UC Berkeley

UC Berkeley Electronic Theses and Dissertations

Title
Strongly Correlated Electron Systems Near Criticality: From Nodal Semimetals to High-Temperature Superconductors

Permalink
https://escholarship.org/uc/item/2pc8r5t5

Author
Dumitrescu, Philipp

Publication Date
2016

Peer reviewed|Thesis/dissertation

Strongly Correlated Electron Systems Near Criticality: From Nodal Semimetals to High-Temperature Superconductors

by

Philipp Dumitrescu

A dissertation submitted in partial satisfaction of the

requirements for the degree of

Doctor of Philosophy

in

Physics

in the

Graduate Division

of the

University of California, Berkeley

Committee in charge:

Professor Ashvin Vishwanath, Chair
Professor Joel E Moore
Professor Tanja Cuk

Spring 2016

Strongly Correlated Electron Systems Near Criticality: From Nodal Semimetals to High-Temperature Superconductors

Abstract

Strongly Correlated Electron Systems Near Criticality: From Nodal Semimetals to High-Temperature Superconductors

by

Philipp Dumitrescu

Doctor of Philosophy in Physics

University of California, Berkeley

Professor Ashvin Vishwanath, Chair

In this thesis, we will study aspects of two phases close to criticality arising in solid state systems with strong interactions between electrons. In the first part, we study finite temperature transport in a non-Fermi-liquid phase arising from a nodal semimetal with long-range interactions – the so-called Luttinger-Abrikosov-Beneslavskii phase. We are particularly interested in calculating the finite temperature shear viscosity of the phase and find that it is consistent with a bound proposed in the context of gauge-gravity duality. In the second part of the thesis, we study a minimal model of nematic fluctuations in the high-temperature superconductor iron selenide. Nematic fluctuations arising from a quantum critical point have been proposed to explain the phenomenology of several high-temperature superconductors. In a numerical simulation using determinant quantum Monte Carlo methods, we find no direct evidence of a nematic critical point. However, we still observe a wide region of superconductivity correlated with nematic fluctuations as well as an unusual antiferro-quadrupole order.

Contents

Acknowledgments

I would like to express my sincere gratitude to my advisor Ashvin Vishwanath. Ashvin gave me an academic home at Berkeley and I want to thank him for his support and confidence over these last five years. My discussions with Ashvin have been a privilege; learning from them has shaped my views of physics and beyond.

I have greatly benefited from the interactions with other faculty, post-docs and students during my time at UC Berkeley, during the semester at KITP in Santa Barbara and during short trips to Stanford University. For many illuminating discussions, I would especially like to thank Yasaman Bahri, Leon Balents, Snir Gazit, Tarun Grover, Steve Kivelson, Itamar Kimchi, Akash Maharaj, Max Metlitski, Adrian Po, Louk Rademaker, Dániel Varjas, Romain Vasseur and Michael Zaletel.

My special thanks go to Sid Parameswaran, Andrew Potter and Maksym Serbyn for their guidance, enthusiasm and support beyond measure.

Part of this work has resulted from research pursued together with Maksym Serbyn, Richard Scalettar, and Ashvin Vishwanath. I want to thank them for the exciting time working together. Thanks also to Joel Moore and Tanja Cuk for agreeing to serve on my thesis committee and to James Analytis for serving on my qualifying examination committee.

Many of my views of physics and condensed matter theory were shaped by people I interacted with while an undergraduate. I would not be where I am without the time and encouragement of Nigel Cooper, Ben Simons, Wilhelm Zwerger, and especially David Khmelnitskii.

My friends from Munich, Cambridge, Berkeley and beyond have been a source of many wonderful memories for which I am thankful.

Above all, I would like to thank my parents and my brother for their love and unwavering support.

This thesis incorporates previously published material from

[1] Dumitrescu, P. T. Shear viscosity in a non-Fermi-liquid phase of a quadratic semimetal. *Phys. Rev. B* **92,** 121102 (2015)

[2] Dumitrescu, P. T. *et al.* Superconductivity and Nematic Fluctuations in a model of FeSe monolayers: A Determinant Quantum Monte Carlo Study. *ArXiv e-prints.* arXiv: `1512.08523 [cond-mat.supr-con]` (2015)

Chapter 1

Introduction

Exploring and describing the nature of phases and phase transitions is a central theme of condensed matter physics. A macroscopic system, such as a solid or a liquid, is made from a very large number of atomic constituents. The laws that govern the large distance and long timescale properties of the system may be entirely different from the laws at the atomic scale. As we are confronted with a wealth of new physical materials and theoretical models, we are steadily increasing our understanding of the effective degrees of freedom which describe a phase and of the external responses associated with those degrees of freedom.

The ideas of the renormalization group (RG) give a natural framework to understand interacting systems with many degrees of freedom, where fluctuation effects between different energy scales become important. Conceptually, we consider the systems starting from the microscopic theory at short-distance scales and construct a theory at successively larger length-scales by integrating out fluctuations at the intermediate scales. This procedure generates effective models, that neglect microscopic details but correctly describe the long distance behavior of the full theory. Iterating this procedure to the longest distances leads us to so-called fixed points, which describe the essential nature of phases or phase transitions. The renormalization group picture naturally highlights the universal nature of phases – different systems have similar long distance properties when their behavior is governed by the same fixed point.

The ideas of RG become precise in the vicinity of a critical point – quintessential examples are the liquid-gas critical point and the Curie point of a ferromagnet. The correlation length ξ of the interaction becomes larger than any characteristic microscopic length-scale of the system ℓ

$$\xi \gg \ell, \tag{1.1}$$

and typically diverges in a scaling form

$$\xi \sim \frac{1}{|g - g_c|^\nu}. \tag{1.2}$$

Here g is some tuning parameter and g_c its critical value; the scaling exponent ν is a universal property of the critical point. Close to the critical point, there is a wide separation of scales, and the dependence on physics at the microscopic scale ℓ generally enters physical response functions in only a simple form. This constrains the structure of the theory at and in the vicinity of the critical point and allows predictions to be made, which depend only on general aspects such as the symmetries and dimensionality of the system.

In the traditional 'Ginzburg-Landau-Wilson' picture of a critical point, phases are distinguished by broken symmetries and the transitions between them are driven by the fluctuations of the broken symmetry order parameter [3–6]. Far away from the phase transition, the correlation length ξ is generically at the microscopic scale ℓ and we can understand the essential phase structure from considering only a small number of interacting constituents. In a classical ferromagnet, for example, the magnetic phase at low temperatures can be thought of as the alignment of neighboring spins, while the paramagnet at high temperatures can be thought of as independent, thermally fluctuating spins. The symmetries and symmetry breaking patterns also determine the low energy excitations of the system through Goldstone's theorem and through the classical hydrodynamics of conserved currents [7–9].

The above considerations apply equally to phase transitions in classical systems, driven by thermal fluctuations, and to phase transitions in quantum mechanical systems, driven by the non-commuting nature of terms in a many-body Hamiltonian [10]. The study of quantum critical phenomena, describing the zero-temperature transitions between different ground-states, has received much interest in recent years due to experimental progress in a variety of materials including high-temperature superconductors, strongly interacting spin systems, heavy-fermion systems, cold-atom systems or quantum Hall systems. While no experiment is ever performed truly in the ground state, the special nature of critical points means that they can dominate the physics of a system even at temperatures and tuning parameters far away.

Beyond the experimental impetus, quantum phases and critical phenomena naturally provide a richer structure then their classical counterparts. Even the most traditional of condensed matter systems – a metal – requires the presence of anti-commuting fermions forming a Fermi surface; it's excitations are quite different from classical order parameter fluctuations. The study of gauge structures and symmetry representations has led to a more refined understanding of phases not distinguished by any local order parameter. This includes symmetry protected topological states such as topological insulators and their interacting analogs [11–13] or topologically ordered states as in fractional quantum Hall systems [14]. Additionally, such structures allow new types of phase transitions, such as between phases not breaking any

symmetries or deconfined criticality driven by degrees of freedom emerging only close to the critical point [15, 16].

1.1 Gapless Electronic Phases

Landau's theory of Fermi liquids adapted for the screened Coulomb interaction is the foundation of our understanding of the electronic properties of metals [17–20]. The fundamental idea is that the phase of the interacting electrons is analytically connected to the non-interacting system. For a free fermion model of solids, the electrons are determined by the band-structure

$$H = \sum_{\mathbf{p}} \varepsilon_{\mathbf{p}} c_{\mathbf{p}}^{\dagger} c_{\mathbf{p}}, \tag{1.3}$$

where $\varepsilon_{\mathbf{p}}$ is the dispersion relation and $\mathbf{p}$ the momentum; other quantum numbers such as band index and spin are suppressed. The Fermi surface is specified at $T = 0$ by $\varepsilon_{\mathbf{p}} = \varepsilon_F$; the states below ε_F in energy are occupied and the states above empty. The electron spectral function is

$$A(\mathbf{p}, \omega) = \delta(\omega - v_F p), \tag{1.4}$$

where ω is the frequency above the chemical potential and v_F the Fermi velocity. The delta-function form reflects the well-defined nature of the electronic excitations, which have a fixed dispersion.

In the presence of interactions, the electron spectral function will still be sharply peaked around a well-defined dispersion

$$A(\mathbf{p}, \omega) = \frac{1}{\pi \tau} \frac{Z}{(\omega - v_F^* p)^2 + 1/\tau^2} + \ldots \sim Z \delta(\omega - \varepsilon_{\mathbf{p}}^*). \tag{1.5}$$

This gives a notion of electronic quasi-particles, with renormalized Fermi velocity v_F^*. The degree of overlap with a free fermion state is captured by the quasi-particle residue Z; the neglected terms marked '...' are the weak incoherent background. A key insight of Landau was that the form (1.5) will be valid even in the presence of strong interactions. The smallness of $1/\tau$ is guaranteed close to the Fermi surface by phase space restrictions and the Pauli exclusion principle. In fact, $1/\tau$ is determined by the leading RG irrelevant perturbation. In three spatial dimensions, $1/\tau \sim \omega^2/\varepsilon_F$, which is small if $\omega \ll \varepsilon_F$. In a different language, the smallness of phase space is a type of $1/N$ expansion [21, 22].

The phase space restriction on electrons is a strong constraint on the emergence of novel phases. For a generic Fermi surface without singularities in the density of states, the only weak coupling instability is attractive Cooper pairing. At low temperatures

this leads to the $U(1)$ gauge-symmetry breaking superconducting state. To obtain behavior with gapless electronic excitations, which is qualitatively different from a Fermi liquid one either has to consider a Fermi surface with strong interactions or consider the limit where the size of the Fermi surface is vanishing – so called nodal semimetals or zero-gap semiconductors.

Non-Fermi-liquid states arising from a strongly interacting Fermi surface have received much attention over the last decades in the study of high-temperature superconductors [23]. With sufficiently strong electron-electron interactions, Fermi liquids can undergo spontaneous symmetry breaking transitions; examples include charge-density, spin-density, nematic or ferromagnetic order. The resultant state may be Mott insulating and all charge degrees of freedom gapped. In the case where a metal undergoes a phase transition into another metallic state, the bosonic critical fluctuations at the transition point can couple strongly to the low lying electronic states. This can lead to the destruction of quasi-particles and to non-Fermi-liquid behavior at the transition point.

Experimentally, there is vast evidence of non-Fermi-liquid behavior in the copper and iron based superconductors. The strange-metal region seen at temperatures above the superconducting dome in a wide variety of high-temperature superconductors has a famous linear-T resistivity, which suggests a state without quasi-particles [24]. Similarly, many experiments suggest that the pseudo-gap region seen in cuprate superconductors has vanishing quasi-particle weight [23]. It is, however, still an open question if these regions are new bona-fide phases of matter.

An entirely different approach to realizing non-Fermi-liquid phases has been to consider systems with small or vanishing Fermi surfaces; the Fermi level is at the point where a conduction and valance band touch. Perhaps the most celebrated experimental realization in recent years is graphene, which hosts two dimensional Dirac electrons [25–27]. Other recent realizations include three dimensional Dirac and Weyl semimetals [28–32]. However, the electron-electron interactions in graphene are RG irrelevant and this is found to be the case in many semimetals. Therefore, a quasi-particle picture remains valid and the interactions give only corrections to the Dirac spectrum at low energies [33]. In contrast, models were interactions are RG relevant are typically driven to a symmetry broken state where a quasi-particle picture may again be applied. In two and three dimensional systems[1], only exceptionally few theories are known which flow to a truly gapless, strongly correlated 'non-Fermi-liquid' phase[2], such as a conformal field theory (CFT). One well known example is QED_3 describing algebraic spin liquids, which has been proposed to be realized in certain strongly coupled spin systems [36, 37].

---

[1]The special kinematic restrictions and symmetries of quasi-one dimensional systems mean that many non-trivial conformal field theories are known [34, 35].

[2]While weakly coupled semimetals lack a Fermi surface and are never true Fermi liquids, we reserve the expression 'non-Fermi-liquid' to cases where the quasi-particle description breaks down.

1.2   Quantum Criticality

A schematic phase diagram of a system with a quantum critical point is shown in Figure 1.1. In addition to the diverging length-scale ξ (1.2) there is an associated energy scale (gap) that vanishes at the critical point

$$\Delta \sim \xi^{-z} \sim |g - g_c|^{\nu z}, \tag{1.6}$$

where z is the dynamic critical exponent, which also sets the dispersion of excitations at criticality $\varepsilon \sim k^z$. When $z \neq 1$, the anisotropy of scaling between space and time is analogous to classical spatially anisotropic critical points (Lifshitz transitions) [38]. Even in non-relativistic systems, many critical points are found to have an emergent Lorentz invariance, giving rise to a critical exponent $z = 1$.

It is convenient to consider the system in imaginary time τ, since this naturally describes both the zero and finite temperature cases. At finite temperatures, an effective dimensional reduction occurs as the imaginary time direction is compactified in a circle of circumference β. At finite temperatures directly at $g = g_c$, the properties of the system are set by the finite size scaling of the critical behavior in the imaginary time direction. Even away from $g = g_c$, where a gap opens according to (1.6), the scaling regime of the quantum critical point persists provided that the temperature is sufficiently high compared to the gap scale Δ. This is referred to as the quantum critical region or 'quantum critical fan' (Figure 1.1). Only once $T \lesssim \Delta$, are the long distance properties determined again by non-universal aspects of the phases.

Just as for a classical critical point, the scale invariant nature of the quantum critical point imposes strong constraints on the form of correlation functions and responses. In the quantum critical regime, correlation functions at finite T, probed at certain frequency ω and momentum k – say of susceptibility of the order parameter ϕ – will have the form

$$G(\omega, k, T) \sim T^{-2\Delta_\phi/z} g\left(\frac{\omega}{T}, \frac{k^z}{T}\right), \tag{1.7}$$

where Δ_ϕ is the scaling dimension of ϕ at the critical point, and $g(x, y)$ some universal scaling function.

Understanding the properties of the quantum critical region is interesting, as they are both fingerprints of the universal physics of the underlying critical point and accessible to experiments. Additionally, fundamentally new physics can emerge out of the quantum critical region. For example, in a quantum critical metal, the non-Fermi liquid arising from critical fluctuations strongly coupling to the Fermi surface is itself unstable towards Cooper paring. The exact nature of superconductivity in the vicinity of critical points and to what extent the incoherent regime survives at all are still open questions [39].
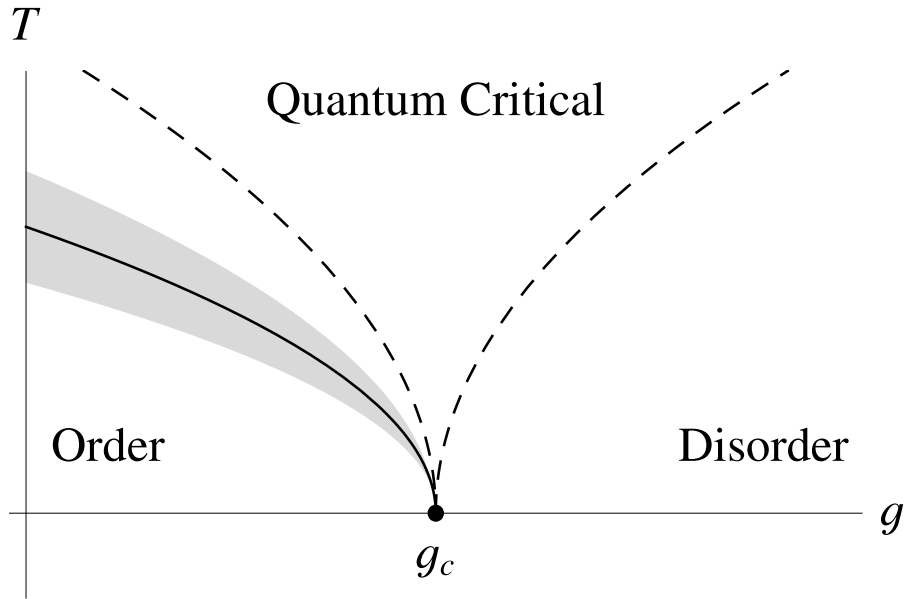
Figure 1.1: Schematic phase diagram of a quantum critical point at $T = 0, g = g_c$ tuned by a parameter g. In the case shown here, the ordered phase also persists to finite temperature and there is a second-order finite-temperature phase transition (solid line). The gray shaded region is the classical critical region, i.e. the range of classical fluctuations. Directly above the quantum critical point is the incoherent, quantum critical region – the crossover lines $\Delta \sim T$ are dashed.

1.3 Transport Properties

Transport coefficients, such as the electrical and thermal conductivities or the viscosities, play a central role in describing condensed matter systems. They are experimentally measurable and contain signatures which characterize the different phases of matter. Nonetheless, for non-Fermi-liquids at finite temperatures, as in the vicinity of a quantum critical point, there remain great difficulties in calculating transport coefficients analytically due to the lack of a quasiparticle description. This is true even when the nature of the underlying critical point is well understood and the transport coefficients are determined by universal physics.

Consider as an example the electrical conductivity at finite frequencies and temperatures, which is related to the current-current correlation function. The expected

scaling behavior is

$$\sigma(\omega, T) \sim T^{(d-2)/z} f\left(\frac{\omega}{T}\right), \tag{1.8}$$

where $f(x)$ is a universal scaling function. As has often been emphasized [10], the limits of ω and T do not commute and the physics in the regimes $\omega \ll T$ and $\omega \gg T$ is very different.

The limit $\omega \gg T$ is essentially that of the zero-temperature fixed point and the correlation function can accurately be calculated in the same way the critical point is accessed – for example order-by-order in a perturbative renormalization-group calculation controlled by an ε or $1/N$ expansion. In contrast, the limit $\omega \ll T$ describes the hydrodynamic regime of thermally activated scale-invariant excitations moving through the sample and interacting with each other over long distances. Calculating the form of the correlation-function in this limit is significantly more complex, even in the ε or $1/N$ expansion. Indeed, if the critical point is not particle-hole symmetric the $\omega = 0$ (DC) conductivity is typically infinite in the absence of translation symmetry breaking effects, due to the total electric current coupling to the conserved total momentum.

Recently, insight has been gained from the relationship between strongly coupled field theories and classical gravitational theories in the context of gauge-gravity duality [40, 41]. From the studies of various special cases, Kovtun, Son and Starinets [42, 43] conjectured a lower bound on the ratio of the shear viscosity η and the entropy density s for a general class of finite temperature field theories

$$\frac{\eta}{s} \geq \frac{\hbar}{4\pi k_B}. \tag{1.9}$$

This bound exactly applies to the DC transport limit, which is theoretically difficult to describe. Since all scattering channels between excitations are saturated in the quantum critical regime, the mean free time of interaction is expected to approach the thermal equilibration time $\tau_{eq} \sim \hbar/k_B T$. This naturally gives rise to universal amplitude ratios which characterize the interacting field theory [10]. Nonetheless, it is very surprising that (1.9) does not contain the speed of light (which is a fixed property of a Lorentz invariant CFT) and therefore should also apply to non-relativistic strongly coupled systems. Models which saturate this bound have been referred to as 'perfect fluids'.

The bound (1.9) is similar to the Mott-Ioffe-Regel limit for the minimal conductivity in disordered metals [44]. As mentioned above, with the exception of particle-hole symmetric theories, the conductivity is determined by mechanisms which break translational symmetry. The ratio η/s is therefore singled out as a good indicator for studying the intrinsic strength of interaction of the underlying carriers. While there are theoretical counter-examples [45, 46] to the bound (1.9), the notion that there

exists some fundamental bound on transport in strongly coupled systems remains. Indeed, most phases which have been studied satisfy (1.9) [47–51].

1.4   Outline

This thesis will study transport phenomena in two different strongly interacting electrons systems, both close to quantum criticality. Part I will consider the so-called Luttinger-Abrikosov-Beneslavskii phase, which is a stable quantum critical phase arising in a spin-orbit coupled zero-gap semiconductor with long-range Coulomb interactions. The particular emphasis will be on understanding the finite temperature shear-viscosity, which has been proposed as a measure of the strength of correlations in an interacting system. Part II will consider a Hubbard-like model describing the physics of the iron-based high-temperature superconductor FeSe and study the relationship of superconductivity to orbital fluctuations.

Note that, unless otherwise stated, we will use units in which the reduced Planck constant $\hbar = 1$ and the Boltzmann constant $k_B = 1$.

Part I

Strongly Correlated Non-Fermi-Liquid Phase

Overview

In the first part of this thesis, we will consider questions related to a strongly correlated non-Fermi-liquid phase arising in a spin-orbit coupled, gapless semiconductor. This phase was originally considered in [52–54] and recently dubbed the 'Luttinger-Abrikosov-Beneslavskii' (LAB) phase by [55].

In chapter 2, we will summarize how the LAB phase arises and the nature of the non-Fermi-liquid behavior. Then we will consider response functions at the one-loop level in chapter 3. The primary goal will be to develop a kinetic equation formalism to describe the d.c. ($\omega = 0$) transport properties, which are dominated by collisions. In particular, we will be interested in computing the shear viscosity η, which we do in chapter 4. The shear viscosity η is relevant to ultrasound attenuation experiments [56–58] and also allows us to characterize the LAB phase in the context of the proposed η/s bound (1.9).

Chapter 2

Luttinger-Abrikosov-Beneslavskii Phase

The low energy excitations of Luttinger-Abrikosov-Beneslavskii (LAB) phase are described by an interacting scale-invariant field theory, which has many unusual features compared to other known non-Fermi liquids: it is realized in a three dimensional system, there is an unusual spin-orbit symmetry, there are long-range Coulomb interactions and the low energy degrees of freedom do not have emergent Lorentz or even Galilean invariance. It has been suggested [55] that this phase could arise in strongly correlated pyrochlore iridates and might explain some of the unusual properties of $Pr_2Ir_2O_7$. More generally, the model has garnered recent attention as part of a focus on emergent quantum phases in materials with strong spin-orbit coupling and in semimetals – these include systems as different as graphene, the surface states of topological insulators, Weyl semimetals or nodal superconductors [59, 60]. Although there are still open question about the low energy properties of the model [61], the LAB phase gives general insights into the nature of non-Fermi liquid phases arising from electron-electron interactions. In this chapter we will consider the origins of the LAB phase and show the existence of the fixed point [52].

2.1   Origins of the Zero-Gap Band-structure

The band-structure which gives rise to the LAB phase is a version of the Luttinger Hamiltonian [62], in which a band inversion occurs. Let us consider a typical s-p semiconductor with cubic symmetry O_h, such as GaAs (Figure 2.1a). The energy bands in the vicinity of the Fermi energy are the 4s, 4p, 5s states, with the conduction band 5s like (Γ_6). Because of spin-orbit coupling, the 3p states split into four $3P_{3/2}$ and two $3P_{1/2}$ states at the Γ point. Away from the Γ point the $P_{3/2}$ bands split into two twofold degenerate bands, forming the valance 'light-hole' and 'heavy-hole'
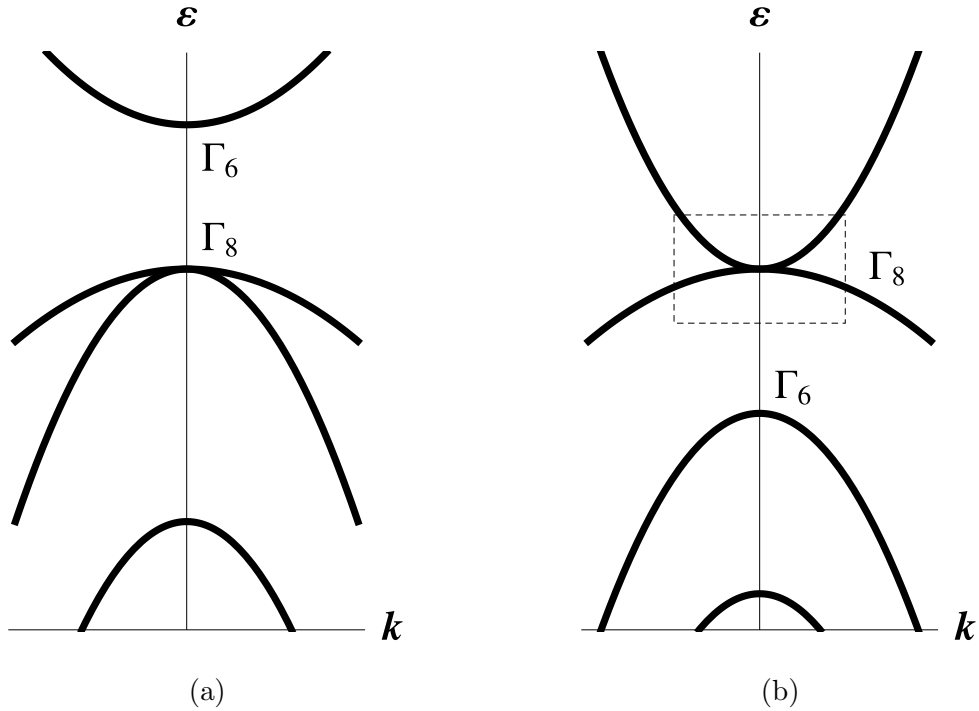
Figure 2.1: Schematic of band-structures in spin-orbit coupled s-p semiconductors. The band-structure in (a) shows a typical direct bandgap semiconductor such as GaAs. There are p-wave light and heavy hole valance bands, which are degenerate at Γ_8; the conduction band is s-wave Γ_6. The band-structure of (b) has a band inversion so that the Γ_6 point lies below the Γ_8 point in energy; this is the case in HgTe. A quadratic band touching forms at the Γ_8 point as one of the hole bands is pushed up in energy. The region of the effective model giving rise to the LAB phase is shown in the dashed box.

bands.

While the basic structure of the $P_{3/2}$ bands close to the Γ point are determined by the representation of the crystal symmetries, the nature of the dispersion is not. In particular, one of the $P_{3/2}$ might be electron-like in nature giving rise to a zero-gap semi-conductor. This typically occurs – such as in the classic examples of α-Sn or HgTe – when the higher s-band is pushed below the $P_{3/2}$ bands (Figure 2.1b). This band inversion is also the origin of topological insulators; HgTe in particular has received much attention in this respect [63, 64]. The four-fold degeneracy at the Γ point is protected by the presence of the O_h symmetry and can only be lifted by applying external strain or confining the system to lower dimensions in a quantum well.

The most general form of the band-structure close to the Γ_8 point in $\mathbf{k} \cdot \mathbf{p}$ theory

was considered by Luttinger in [62]. The $P_{3/2}$ bands are conveniently written in terms of $j = 3/2$ angular momentum matrices:

$$J_x = \frac{1}{2} \begin{pmatrix} 0 & \sqrt{3} & 0 & 0 \\ \sqrt{3} & 0 & 1 & 0 \\ 0 & 1 & 0 & \sqrt{3} \\ 0 & 0 & \sqrt{3} & 0 \end{pmatrix}, \qquad J_y = \frac{i}{2} \begin{pmatrix} 0 & -\sqrt{3} & 0 & 0 \\ \sqrt{3} & 0 & -1 & 0 \\ 0 & 1 & 0 & -\sqrt{3} \\ 0 & 0 & \sqrt{3} & 0 \end{pmatrix}, \qquad J_z = \frac{1}{2} \begin{pmatrix} 3 & 0 & 0 & 0 \\ 0 & 1 & 0 & 0 \\ 0 & 0 & -1 & 0 \\ 0 & 0 & 0 & -3 \end{pmatrix},$$

$$(2.1)$$

so $J^2 = J_x^2 + J_y^2 + J_z^2 = 15/4$. We can use these to construct a set of 16 independent matrices onto which we can decompose all other matrices:

$$1$$
$$J_x, J_y, J_z$$
$$J_x^2, J_y^2, \tfrac{1}{2}\{J_x, J_y\}, \tfrac{1}{2}\{J_y, J_z\}, \tfrac{1}{2}\{J_z, J_x\},$$
$$\tfrac{1}{2}\{(J_y^2 - J_z^2), J_x\}, \tfrac{1}{2}\{(J_z^2 - J_x^2), J_y\}, \tfrac{1}{2}\{(J_x^2 - J_y^2), J_z\},$$
$$J_x^3, J_y^3, J_z^3, J_x J_y J_z + J_z J_y J_x$$

$$(2.2)$$

In the absence of any external strain or time-reversal symmetry breaking due to a magnetic field, the most general quadratic Hamiltonian of the bands around the Γ_8 point is [62]

$$H = \beta_1 k^2 + \beta_2 \left(k_x^2 J_x^2 + k_y^2 J_y^2 + k_z^2 J_z^2 \right)$$
$$+ 2\beta_3 \left(k_x k_y \{J_x, J_y\} + k_y k_z \{J_y, J_z\} + k_z k_x \{J_z, J_x\} \right) \quad (2.3)$$

with $\beta_1, \beta_2, \beta_3$ constants. We will restrict ourselves to the fully rotationally invariant case $\beta_2 = \beta_3$, which will turn out to be the relevant case for the LAB phase. We write the Hamiltonian in the more insightful form [52]

$$H = f k^2 + c A_{ij} k_i k_j, \quad (2.4)$$

where

$$A_{ij} = \frac{1}{2}\{J_i, J_j\} - \frac{1}{3} J^2 \delta_{ij}. \quad (2.5)$$

The A_{ij} matrices satisfy a more complex mathematical structure which makes them suitable for generalization, which we will consider below. The energy spectrum of the free bands has the simple form

$$\varepsilon_k = (f \pm c) k^2, \quad (2.6)$$

with each band being twofold degenerate.

2.2 A_{ij} Matrices

For the model which is isotropic in all directions we chose

$$A_{ij} = \frac{1}{2}\{J_i, J_j\} - \frac{1}{3}J^2\delta_{ij}, \tag{2.5'}$$

in the physical dimension $d = 3$. Because we will be performing an ε-expansion we need to extend the spin structure to fractional dimension; there is an intrinsic ambiguity on how to do this. The choice will affect both the fixed point value of the interaction found from the RG analysis as well as the scattering elements entering a kinetic equation. The simplest choice is to formally use the $d = 3$ structure. One can also use a spin structure in $d = 4$ – the starting point of the ε-expansion – by embedding the rotation group $SU(2)$ for $j = 3/2$ spin in a higher dimensional group, such as $SO(4)$.

Alternatively, Abrikosov [52] constructed a series of spin-orbit coupled models with quadratic band touching in arbitrary dimensions d using Clifford matrices. The relationship of states around the Γ_8 point to the $SO(5)$ Clifford algebra has been stressed recently in [65]. The Hamiltonian is

$$H = \gamma^a d_a(\mathbf{k}), \qquad a = 1, 2, \ldots, (d-1)(d+2)/2 \tag{2.7}$$

where γ^a are anti-commuting Clifford matrices. The $d_a(\mathbf{k})$ are functions determined by requiring that the dispersion should be quadratic $[H^2 = d_a(\mathbf{k})d_a(\mathbf{k}) = c^2k^4]$ and by imposing an orthogonality condition over angular integration $[\int \mathrm{d}\Omega_{\mathbf{k}} d_a(\mathbf{k})d_a(\mathbf{k}') = 0$ for $\mathbf{k}'$ constant]. Since one can construct the $SO(N)$ Clifford algebra from sets of Pauli matrices, it is easy to determine the dimension of the representation r_d – in particular, $r_3 = 4$, $r_4 = 16$. From the γ^a, we define generalized A_{ij} matrices satisfying

$$\{A_{ij}, A_{kl}\} = \frac{d}{d-1}(\delta_{ik}\delta_{jl} + \delta_{il}\delta_{jk}) - \frac{2}{d-1}\delta_{ij}\delta_{kl} \tag{2.8}$$

This relationship is also well defined in fractional dimensions and is useful for the ε-expansion since only this combination appears in the RG calculation. In certain dimensions, a γ matrix will not enter the Hamiltonian and thus give a notion of chiral symmetry to the states. Importantly, this does not occur for the relevant dimensions for our model $d = 3, 4$. This does occur $d = 2$, where the Hamiltonian describes, e.g. a special case of the quadratic chiral edge state at the surface of a crystalline topological insulator [66].

2.3 Eigenstates

The eigenstates of the free system (2.4) are plane waves with spinor structure. The fields are

$$\psi_a(\mathbf{x}) = \int \frac{\mathrm{d}^3 k}{(2\pi)^3} \, [u_m(\mathbf{k})]_a \, c_m(\mathbf{k}) e^{i\mathbf{k}\cdot\mathbf{x}} \tag{2.9}$$

where

$$[u_m(\mathbf{k})]_a = \mathscr{D}^{3/2}_{am}(\varphi, \theta, 0) \tag{2.10}$$

with (φ, θ) the Euler angles of $\hat{\mathbf{k}}$ and $\mathscr{D}^{3/2}$ the Wigner D-symbols associated with the rotation R which takes $\hat{\mathbf{z}}$ to $\hat{\mathbf{k}}$ [67]. The fact that we set the Euler angle $\gamma = 0$ is a phase choice in the definition of the wave-functions. The states with helicity $\hat{\mathbf{k}}\cdot\mathbf{J} = \pm 1/2$ correspond to the valance band and the states with helicity $\hat{\mathbf{k}}\cdot\mathbf{J} = \pm 3/2$ correspond to the conduction band.

Parity acts as

$$P c_m(\mathbf{p}) P^{-1} = \eta c_{-m}(-\mathbf{p}) \tag{2.11}$$

where η is a phase choice. Using the property of Wigner matrices $\mathscr{D}_{ab}(-\mathbf{p}) = i\mathscr{D}_{a,-b}(\mathbf{p})$, the action of parity on the field is

$$P \psi(\mathbf{x})_a P^{-1} = i\eta \psi(-\mathbf{x})_a \tag{2.12}$$

as required for the Hamiltonian to be invariant. The action of time-reversal is

$$T c_m(\mathbf{p}) T^{-1} = \zeta(-1)^{3/2-m} c_m(-\mathbf{p}) \tag{2.13}$$

where ζ is a phase choice. We obtain the action on the fields

$$T \psi(\mathbf{x}, t)_a T^{-1} = \zeta M_{ab} \psi(\mathbf{x}, -t)_b. \tag{2.14}$$

To make manifest the time-reversal symmetry of the Hamiltonian, we note the symmetry of the A matrices

$$A^*_{ij} = A^T_{ij} = M A_{ij} M^{-1} \tag{2.15}$$

where

$$M = \tau_x \sigma_y = i \begin{pmatrix} 0 & 0 & 0 & -1 \\ 0 & 0 & 1 & 0 \\ 0 & -1 & 0 & 0 \\ 1 & 0 & 0 & 0 \end{pmatrix} \tag{2.16}$$

Finally, even in the case $f = 0$, where the dispersion of the conduction and valance band are symmetric, $\varepsilon = \pm ck^2$, the model does not have particle-hole symmetry. This is most easily seen by noting that the magnitude of the helicities of the two bands are different ($\pm 3/2$ vs. $\pm 1/2$). On a technical level, the Hamiltonian written as (2.7) in $d = 3$ requires all five γ matrices and no additional matrix can be constructed

to represent the action of particle-hole symmetry. This lack of particle-hole symmetry has far reaching consequences. For example, unlike many critical theories, the clean system does not have a universal finite temperature conductivity as the electric current couples to the conserved total momentum.

Matrix Elements

We will need the form of matrix elements for transitions between the various bands. For convenience, we introduce the spherical basis

$$\hat{\mathbf{e}}_{+1} = -\tfrac{1}{\sqrt{2}}(\hat{\mathbf{x}} + i\hat{\mathbf{y}}) \tag{2.17}$$

$$\hat{\mathbf{e}}_0 = \hat{\mathbf{z}} \tag{2.18}$$

$$\hat{\mathbf{e}}_{-1} = \tfrac{1}{\sqrt{2}}(\hat{\mathbf{x}} - i\hat{\mathbf{y}}) \tag{2.19}$$

which satisfies the orthogonality condition $\hat{\mathbf{e}}_q^* \hat{\mathbf{e}}_{q'} = \delta_{qq'}$. We wish to evaluate quantities of the type $u_m^\dagger(\hat{\mathbf{n}} \cdot \mathbf{J})u_m$ and similar. Denote the vector spin-1 rotation matrix taking $\hat{\mathbf{k}} \to \hat{\mathbf{z}}$ by $R^{-1}(\mathbf{k})$.

$$u_m^\dagger(\mathbf{k})(\hat{\mathbf{n}} \cdot \mathbf{J})u_m(\mathbf{k}) = \hat{\mathbf{e}}_q^* \{R^{-1}(\mathbf{k})[\hat{\mathbf{n}}]\} \langle m'| J_q |m\rangle \tag{2.20}$$

$$\langle m'| J_q |m\rangle = \begin{cases} m\delta_{m,m'}, & q = 0 \\ \mp\delta_{m+q,m'}\sqrt{(j \mp m)(j \pm m + 1)/2}, & q = \pm 1 \end{cases} \tag{2.21}$$

Hence we obtain the matrix elements

$$u_{\pm 3/2}^\dagger(\mathbf{k})(\hat{\mathbf{n}} \cdot \mathbf{J})u_{\pm 3/2}(\mathbf{k}) = \pm\tfrac{3}{2}\hat{\mathbf{n}} \cdot \hat{\mathbf{k}} \tag{2.22}$$

$$u_{\pm 1/2}^\dagger(\mathbf{k})(\hat{\mathbf{n}} \cdot \mathbf{J})u_{\pm 1/2}(\mathbf{k}) = \pm\tfrac{1}{2}\hat{\mathbf{n}} \cdot \hat{\mathbf{k}} \tag{2.23}$$

$$u_{\pm 3/2}^\dagger(\mathbf{k})(\hat{\mathbf{n}} \cdot \mathbf{J})u_{\mp 3/2}(\mathbf{k}) = 0 \tag{2.24}$$

$$u_{\pm 1/2}^\dagger(\mathbf{k})(\hat{\mathbf{n}} \cdot \mathbf{J})u_{\mp 1/2}(\mathbf{k}) = \sqrt{2}T_\pm(\hat{\mathbf{n}}) \tag{2.25}$$

$$u_{\pm 3/2}^\dagger(\mathbf{k})(\hat{\mathbf{n}} \cdot \mathbf{J})u_{\mp 1/2}(\mathbf{k}) = 0 \tag{2.26}$$

$$u_{\pm 3/2}^\dagger(\mathbf{k})(\hat{\mathbf{n}} \cdot \mathbf{J})u_{\pm 1/2}(\mathbf{k}) = \sqrt{\tfrac{3}{2}}T_\pm(\hat{\mathbf{n}}) \tag{2.27}$$

where

$$T_+(\hat{\mathbf{n}}) = T_-^\dagger(\hat{\mathbf{n}}) = -\hat{\mathbf{e}}_+^* \{R^{-1}(\mathbf{k})[\hat{\mathbf{n}}]\} = \frac{[\hat{\mathbf{e}}_- \cdot \hat{\mathbf{k}}](-i\hat{\mathbf{k}} \times \hat{\mathbf{n}} - \hat{\mathbf{n}} + (\hat{\mathbf{k}} \cdot \hat{\mathbf{n}})\hat{\mathbf{k}}) \cdot \hat{\mathbf{z}}}{1 - (\hat{\mathbf{k}} \cdot \hat{\mathbf{z}})^2} \tag{2.28}$$

Denote by n_i, m_i the components of the unit vectors $\hat{\mathbf{n}}, \hat{\mathbf{m}}$:

$$u^\dagger_{\pm 3/2}(\mathbf{k})(A_{ij}n_i m_j)u_{\pm 3/2}(\mathbf{k}) = \tfrac{9}{4}(\hat{\mathbf{n}} \cdot \hat{\mathbf{k}})(\hat{\mathbf{m}} \cdot \hat{\mathbf{k}}) - \tfrac{5}{4}(\hat{\mathbf{n}} \cdot \hat{\mathbf{m}})$$
$$+ \tfrac{3}{4}[T_+(\hat{\mathbf{m}})T_-(\hat{\mathbf{n}}) + T_-(\hat{\mathbf{m}})T_+(\hat{\mathbf{n}})] \tag{2.29}$$

$$u^\dagger_{\pm 1/2}(\mathbf{k})(A_{ij}n_i m_j)u_{\pm 1/2}(\mathbf{k}) = \tfrac{1}{4}(\hat{\mathbf{n}} \cdot \hat{\mathbf{k}})(\hat{\mathbf{m}} \cdot \hat{\mathbf{k}}) - \tfrac{5}{4}(\hat{\mathbf{n}} \cdot \hat{\mathbf{m}})$$
$$+ \tfrac{7}{4}[T_+(\hat{\mathbf{m}})T_-(\hat{\mathbf{n}}) + T_-(\hat{\mathbf{m}})T_+(\hat{\mathbf{n}})] \tag{2.30}$$

$$u^\dagger_{\pm 3/2}(\mathbf{k})(A_{ij}n_i m_j)u_{\pm 1/2}(\mathbf{k}) = \pm\sqrt{\tfrac{3}{2}}\left[(\hat{\mathbf{n}} \cdot \hat{\mathbf{k}})T_\pm(\hat{\mathbf{m}}) + (\hat{\mathbf{m}} \cdot \hat{\mathbf{k}})T_\pm(\hat{\mathbf{n}})\right] \tag{2.31}$$

$$u^\dagger_{\pm 3/2}(\mathbf{k})(A_{ij}n_i m_j)u_{\mp 1/2}(\mathbf{k}) = \sqrt{3}T_\pm(\hat{\mathbf{m}})T_\pm(\hat{\mathbf{n}}) \tag{2.32}$$

$$u^\dagger_{+3/2}(\mathbf{k})(A_{ij}n_i m_j)u_{-3/2}(\mathbf{k}) = 0 \tag{2.33}$$

$$u^\dagger_{+1/2}(\mathbf{k})(A_{ij}n_i m_j)u_{-1/2}(\mathbf{k}) = 0 \tag{2.34}$$

and their Hermitian conjugates. In particular, we will need the form

$$u^\dagger_{\pm 3/2}(\mathbf{k})(A_{ij}n_i k_j)u_{\pm 3/2}(\mathbf{k}) = +\hat{\mathbf{n}} \cdot \mathbf{k} \tag{2.35}$$

$$u^\dagger_{\pm 1/2}(\mathbf{k})(A_{ij}n_i k_j)u_{\pm 1/2}(\mathbf{k}) = -\hat{\mathbf{n}} \cdot \mathbf{k} \tag{2.36}$$

$$u^\dagger_{\pm 3/2}(\mathbf{k})(A_{ij}n_i k_j)u_{\pm 1/2}(\mathbf{k}) = \pm k\sqrt{\tfrac{3}{2}}T_\pm(\hat{\mathbf{n}}) \tag{2.37}$$

and all others being zero. As expected, the form of the Hamiltonain is

$$H = \sum_m \int \frac{\mathrm{d}^3 k}{(2\pi)^3}\sigma_m E_k c^\dagger_m c_m \tag{2.38}$$

where $E_k = ck^2$ and $\sigma_m = m^2 - 5/4$.

2.4   The Luttinger-Abrikosov-Beneslavskii Model

We now consider the Luttinger band-structure (2.4) with the Fermi level fixed at the quadratic band touching. The electrons are interacting via the long range Coulomb interaction. The $T = 0$ partition function in path integral form is

$$Z = \int \mathscr{D}[\psi, \psi^\dagger]\,e^{iS}, \tag{2.39}$$

where the action S is

$$S = S_0 + S_{int}$$

$$S_0 = \int \mathrm{dt}\mathrm{d}^3x \; \left[i\psi_a^\dagger(\partial_t\psi_a) - f(\partial_i\psi_a^\dagger)(\partial_i\psi_a) - c(\partial_i\psi_a^\dagger)\left[A_{ij}\right]_{ab}(\partial_j\psi_b)\right],$$

$$S_{int} = -\frac{1}{2}\int \mathrm{dt}\mathrm{d}^3x\mathrm{d}^3x' \left[\frac{\rho(\mathbf{x})\rho(\mathbf{x}')}{|\mathbf{x}-\mathbf{x}'|}\right].$$

(2.40)

Here $\psi(\mathbf{x})$ are the four component electron fields, $\rho(\mathbf{x}) = e\psi^\dagger(\mathbf{x})\psi(\mathbf{x})$ is the electric charge density and e is the charge of the electron. It will be convenient to decouple the interaction in the density channel using a real Hubbard-Stratonovitch field φ, by inserting

$$1 = \int \mathscr{D}\varphi \; \exp\left[\frac{i}{2}\int \frac{\mathrm{d}\omega\,\mathrm{d}^dk}{(2\pi)^{d+1}}\varphi(\omega,\mathbf{k})\cdot\frac{k^2}{4\pi e^2}\cdot\varphi(-\omega,-\mathbf{k})\right]$$

(2.41)

to the partition function and shifting fields. The interaction term of the action becomes

$$S_{int} = \int\mathrm{dt}\mathrm{d}^3x\mathrm{d}^3x' \; \left[-\frac{1}{2}\frac{\rho(\mathbf{x})\rho(\mathbf{x}')}{|\mathbf{x}-\mathbf{x}'|}\right] = \int\mathrm{d}^3x\mathrm{dt} \; \left[\frac{1}{8\pi e^2}(\partial_i\varphi)(\partial_i\varphi) - \varphi\psi_a^*\psi_a\right].$$

(2.42)

Because we are considering the usual non-dynamic Coulomb interaction between electrons, the terms can be derived by coupling the theory to electromagnetism and only considering the scalar part. From the electromagnetic Maxwell term, rescaled by the interaction

$$-\frac{1}{16\pi e^2}F_{\mu\nu}F^{\mu\nu} \to +\frac{1}{8\pi e^2}(\partial_i\varphi)(\partial_i\varphi).$$

(2.43)

The second term in (2.42) is the density interaction and comes from the $U(1)$ minimal substitution $\partial_t \to \partial_t + i\varphi$.

2.5 Low Energy Behavior in an ε-expansion

We will first consider the scaling in general spatial dimension d to determine the effect of the Coulomb interactions at low energies. Let the scaling variable be $[K] = -[L] = 1$. We perform the scaling such that the kinetic term $cA_{ij}\partial_i\psi^\dagger\partial_j\psi$ remains invariant. The scaling dimensions of the other variables at tree level (bare scaling) are

$$\begin{aligned}
[\omega] &= -[T] = 2, \\
[f] &= 0, & [e^2] &= 4 - d, \\
[\psi(t,\mathbf{x})] &= \tfrac{1}{2}d, & [\varphi(t,\mathbf{x})] &= 2, \\
[\psi(\omega,\mathbf{k})] &= -\tfrac{1}{2}(d+4), & [\varphi(\omega,\mathbf{k})] &= -d.
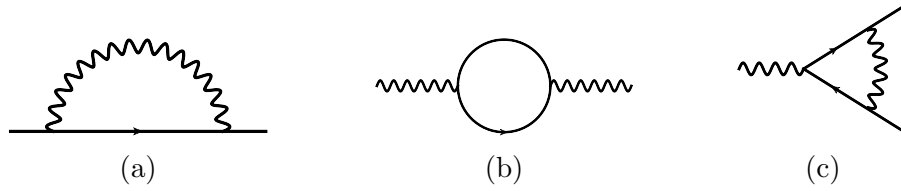\end{aligned}$$

(2.44)

Figure 2.2: One-loop diagrams needed to be considered for the perturbative renormalization (a) Electron self-energy (b) Boson self-energy (polarization) (c) Vertex correction.

We see that the interaction between electrons is relevant in the physical dimension $d = 3$ and marginal in $d = 4$. In order to control the RG flow, we can therefore use an epsilon expansion ($\varepsilon = 4 - d \ll 1$) with non-integer dimension d to control the perturbative RG calculation; this will be the simplest way to access the LAB fixed point [52].

Within the ε-expansion, the dimensionless coupling constant $\alpha = e^2/c\Lambda^\varepsilon$ evolves under the renormalization group and one finds that the system flows towards a stable Wilson-Fisher fixed point [52, 55]. In particular, in the scaling limit close to the fixed point the propagator of the auxiliary Coulomb field remains unscreened and takes the general form

$$V(\omega, \mathbf{q}) = \frac{1}{q^{2-\eta_\varphi}} S\left(\frac{\omega}{q^z}\right). \tag{2.45}$$

Here z is the anomalous exponent describing the scaling between energy and momentum $\epsilon(\mathbf{k}) = ck^z$ and η_φ is the anomalous scaling dimension of the Coulomb field. The scaling function $S(x)$ is defined so that in the asymptotic limit $S \to 1$ as $x \to 0$.

One-Loop ε-expansion

In this section, we perform the ε-expansion to lowest order and show the presence of a stable fixed point. Since we are expanding about the dimension where the interaction is marginal, it is sufficient to keep only logarithmically diverging terms. The free causal electronic Green function at $T = 0$ is

$$G^{(0)}_{ab}(\omega, \mathbf{k}) = [\omega - H_e(\mathbf{k}) + i\delta \, \mathrm{sgn}(\omega)]^{-1}_{ab}, \tag{2.46}$$

$$= \frac{(\omega - fk^2)\delta_{ab} + c\,[A_{ij}]_{ab}\,k_i k_j}{(\omega - fk^2)^2 - (ck^2 - i\delta')^2}, \tag{2.47}$$

where $\delta, \delta' \to 0^+$. The non-dynamic Coulomb Green function is

$$D^{(0)}(\omega, \mathbf{k}) = \frac{4\pi e^2}{k^2}. \tag{2.48}$$

We use a hard momentum cutoff Λ; physically this momentum must be sufficiently small that the approximation of the Luttinger band-structure is valid. The divergent part of the one-loop electronic self-energy (Figure 2.2a) is

$$\Sigma_{ab}^{(1)}(\omega, \mathbf{k}) = i \int \frac{d\Omega \, d^d q}{(2\pi)^{d+1}} \, D^{(0)}(\omega, \mathbf{k}) G_{ab}^{(0)}(\Omega + \omega, \mathbf{q} + \mathbf{k}), \tag{2.49}$$

$$= c \, [A_{ij}]_{ab} \, k_i k_j \cdot \frac{2\pi e^2 (d-2)}{c(d+2)} \int^{\Lambda} \frac{d^d q}{(2\pi)^d} \frac{1}{q^4} + \dots, \tag{2.50}$$

while divergent contribution of the first correction to the polarization (Figure 2.2b) is

$$\Pi^{(1)}(\omega, \mathbf{k}) = -i \operatorname{tr} \int \frac{d\Omega \, d^d q}{(2\pi)^{d+1}} G^{(0)}(\Omega - \tfrac{1}{2}\omega, \mathbf{q} - \tfrac{1}{2}\mathbf{k}) G^{(0)}(\Omega + \tfrac{1}{2}\omega, \mathbf{q} + \tfrac{1}{2}\mathbf{k}), \tag{2.51}$$

$$= -\frac{r_d}{4c} \int^{\Lambda} \frac{d^d q}{(2\pi)^d} \left(\frac{k^2}{q^4} \right) + \dots \tag{2.52}$$

The first correction to the electron-photon vertex (Figure 2.2c) is convergent so that we can neglect the contribution in the peturbative RG

$$\gamma^{(1)} = \int \frac{d\Omega \, d^d K}{(2\pi)^{d+1}} G^{(0)}(\Omega + \omega, \mathbf{K} + \mathbf{q}) G^{(0)}(\Omega, \mathbf{K}) D^{(0)}(\omega' - \Omega, \mathbf{k} - \mathbf{K}), \tag{2.53}$$

$$\sim \int \frac{d^d K}{(2\pi)^d} O(K^{-6}) + \dots \tag{2.54}$$

Summing the corrections for the electron and photon Green function

$$G = G^{(0)} + G^{(0)} \Sigma^{(1)} G = \frac{G^{(0)}}{1 - \Sigma^{(1)} G^{(0)}}, \tag{2.55}$$

$$= \left[\omega - fk^2 - cA_{ij}k_i k_j \left(1 + \frac{2\pi e^2 (d-2)}{c(d+2)} \int^{\Lambda} \frac{d^d q}{(2\pi)^d} \frac{1}{q^4} \right) + i\delta \operatorname{sgn}(\omega) \right]^{-1}, \tag{2.56}$$

$$D = D^{(0)} + D^{(0)} \Pi^{(1)} D = \frac{D^{(0)}}{1 - \Pi^{(1)} D^{(0)}} = \left[\frac{k^2}{4\pi e^2} + \frac{r_d}{4c} \int^{\Lambda} \frac{d^d q}{(2\pi)^d} \frac{k^2}{q^4} \right]^{-1}. \tag{2.57}$$

Now set $d = 4 - \varepsilon$ and, imagining we have integrated out high momentum shells from Λ to Λ/b, where we denote $b = e^{\mathrm{d}\ell}$.

$$
\begin{aligned}
S = \int^{\Lambda/b} \frac{\mathrm{d}\omega\, \mathrm{d}^d k}{(2\pi)^{d+1}} & \left[\psi_a^*(\omega, \mathbf{k}) \left(\omega - f k^2 - c\,[A_{ij}]_{ab}\, k_i k_j \cdot (1 + B \mathrm{d}\ell) \right) \psi_b(\omega, \mathbf{k}) \right. \\
& \left. + \frac{1}{2} \varphi(\omega, \mathbf{k}) \left(\frac{k^2}{4\pi e^2} + k^2 \frac{r_d}{2c(4\pi)^{d/2}\Gamma(d/2)} \mathrm{d}\ell \right) \varphi(-\omega, -\mathbf{k}) \right] \\
& - \int^{\Lambda/b} \frac{\mathrm{d}\omega\, \mathrm{d}\Omega\, \mathrm{d}^d k\, \mathrm{d}^d q}{(2\pi)^{2d+2}} \left[\varphi(-\Omega, -\mathbf{q})\psi_a^*(\omega + \Omega, \mathbf{k} + \mathbf{q})\psi_a(\omega, \mathbf{k}) \right] \quad (2.58)
\end{aligned}
$$

here the Λ/b applies only to the momentum integrals and we have defined

$$
B = \frac{4\pi e^2 (d - 2)}{(4\pi)^{d/2} c (d + 2) \Gamma(d/2)}. \tag{2.59}
$$

Now rescale $k \to k e^{-\mathrm{d}\ell}, \omega \to \omega e^{-z\mathrm{d}\ell}$ and renormalize the fields so that the coefficients of the A_{ij} and the interaction term are unchanged

$$
\psi \to \psi (1 + B\mathrm{d}\ell)^{-1/2} e^{(d+z+2)\mathrm{d}\ell/2}, \tag{2.60}
$$

$$
\varphi \to \varphi (1 + B\mathrm{d}\ell) e^{(2z+2d-(d+z+2))\mathrm{d}\ell}. \tag{2.61}
$$

We obtain for the time-dependent term

$$
\frac{\omega e^{(2-z)\mathrm{d}\ell}}{1 + B\mathrm{d}\ell} \simeq \omega \exp\left[(2 - z - B)\, \mathrm{d}\ell \right], \tag{2.62}
$$

which sets the dynamical critical exponent

$$
z = 2 - B. \tag{2.63}
$$

The action is now a self-similar form, provided we let

$$
f' = \frac{f}{1 + B\mathrm{d}\ell} \tag{2.64}
$$

$$
\frac{1}{e'^2} = \left(\frac{1}{e^2} + \frac{2\pi r_d}{(4\pi)^{d/2}\Gamma(\frac{1}{2}d)} \mathrm{d}\ell \right) e^{(d+z-6)\mathrm{d}\ell} (1 + B\mathrm{d}\ell)^2 \tag{2.65}
$$

which we can express as a flow equation

$$\frac{\mathrm{d}f}{\mathrm{d}\ell} = -Bf \tag{2.66}$$

$$\frac{\mathrm{d}e^2}{\mathrm{d}\ell} = (6 - d - z)e^2 - e^4 \left(\frac{4\pi r_d}{2c(4\pi)^{d/2}\Gamma(\frac{1}{2}d)} + \frac{2B}{e^2} \right) \tag{2.67}$$

Letting $d = 4 - \varepsilon$ we obtain a perturbative fixed point; to lowest order in ε

$$\alpha^* = \left(\frac{e^2}{c} \right)^* = \frac{24\pi}{3r_d + 2}\varepsilon \to \frac{12\pi}{25} \tag{2.68}$$

To lowest order in ε, the dynamical critical exponent

$$z = 2 - \frac{2}{3r_d + 2}\varepsilon \to 2 - \frac{1}{25}. \tag{2.69}$$

If we set $r_4 = 16$ – the smallest dimension of the representation in $d = 4$ – and set $\varepsilon = 1$ we obtain exactly the results first obtained by [52]. We trivially expand $e^2 = (e^2)^* + \delta e^2$ so

$$\frac{\mathrm{d}\delta e^2}{\mathrm{d}\ell} = -\varepsilon \delta e^2 \tag{2.70}$$

which implies the fixed point is stable. If we were to have chosen to formally use the $d = 3$ structure (2.5′) of the commutation relation but still perform the integrals in $d = 4 - \varepsilon$ the results would be

$$\alpha^* = \left(\frac{e^2}{c} \right)^* = \frac{64\pi}{3(3r_d + 2)}\varepsilon \to \frac{32\pi}{21}, \qquad z = 2 - \frac{9}{4(3r_d + 2)}\varepsilon \to 2 - \frac{9}{56} \tag{2.71}$$

with $r_3 = 4$. The difference in the above results is mostly due to the different dimension of the representation $r_{3,4}$, rather the form of the commutator $\{A_{ij}, A_{kl}\}$ or the prescription of angular integration. For calculating the shear viscosity in Chapter 4, we shall therefore use the $d = 3$ structure (2.5′) with $r_3 = 4$.

We see from (2.66) that the isotropic term is irrelevant at the Wilson-Fisher fixed point. Therefore, we shall generally consider the low energy regime, where these terms are asymptotically small and can be neglected and set $f = 0$ form the outset. Abrikosov argues [52, 68] that the IR fixed point will be isotropic in general.

Large-N Theory

One can also develop a controlled RG calculation in $d = 3$ in the limit of a large number N of electronic fields [52], which gives a consistent picture with the fixed

point found above. We will not pursue this calculation here. This restriction is due to technical features of the kinetic equation calculation. A consistent large-N theory needs to includes the full frequency dependent one-loop renormalized interaction; see [10].

Chapter 3

One-Loop Response Functions

In this chapter, we will compute the one-loop response functions for the conductivity and shear viscosity of the LAB model. These correspond to the response of the free band-structure without interaction effects. Apart from being interesting in their own right, they will be useful for setting up the form of the correlation functions that will be calculated in the fully interacting case and address some subtleties in the definition of the viscosity. Additionally, they allow us a platform to draw connections to the kinetic equation approach developed later.

3.1 Conductivity

Keeping in mind that in the LAB phase the band-structure becomes isotropic under the RG flow, let us consider the simplest band-structure of (2.4) with $f = 0$, and couple a background $U(1)$ field (a_0, a_i) using minimal substitution. The action is

$$S = \int \mathrm{d}t \mathrm{d}^d x \left\{ i\psi_a^\dagger \partial_t \psi_a - ea_0 \psi_a^\dagger \psi_a - c\left[A_{ij}\right]_{ab} \left[(\partial_i + iea_i)\psi_a^\dagger\right] \left[(\partial_j - iea_j)\psi_b\right] \right\}. \quad (3.1)$$

The minimal substitution procedure guarantees invariance under the gauge transformation

$$a_i \to a_i + \partial_i f, \qquad a_0 \to a_0 - \partial_t f, \qquad \psi_a \to e^{ief}\psi_a. \quad (3.2)$$

The charge density

$$\rho(\mathbf{x}, t) = e\psi_a^\dagger \psi_a, \quad (3.3)$$

and current density

$$j_i(\mathbf{x}, t) = j_i^{(p)}(\mathbf{x}, t) + j_i^{(d)}(\mathbf{x}, t),$$

$$j_i^{(p)}(\mathbf{x}, t) = ec\,[A_{ij}]_{ab}\,\left[\psi_a^\dagger(-i\partial_j\psi_b) + (i\partial_j\psi_a^\dagger)\psi_b\right], \tag{3.4}$$

$$j_i^{(d)}(\mathbf{x}, t) = 2e^2 c\,[A_{ij}]_{ab}\,\psi_a^*\psi_b a_j.$$

are given from Noether's theorem. The current has both a paramagnetic and diamagnetic contribution, both of which are needed to obtain a gauge invariant conductivity.

In linear response theory, the current induced by an external field is given by

$$\langle j_i(\mathbf{r})\rangle = -\int \mathrm{d}^d r\; K_{ij}^{(M)}(i\omega_n, \mathbf{r} - \mathbf{r}')a_j(\mathbf{r}') = -\int \mathrm{d}^d r\; \Pi_{ij}^{(M)}(i\omega_n, \mathbf{r} - \mathbf{r}')a_j(\mathbf{r}') - \langle j_i^{(d)}(\mathbf{r})\rangle, \tag{3.5}$$

where we have explicitly separated out the diamagnetic contribution $\langle j_i^{(d)}(\mathbf{r})\rangle$. The response $\Pi^{(M)}$ from the paramagnetic current can be calculated using the Kubo formula [69] for the current-current correlator. In imaginary time

$$\Pi_{ij}^{(M)}(i\omega_n, \mathbf{r} - \mathbf{r}') = -\frac{1}{2}\int_{-\beta}^{\beta}\mathrm{d}\tau\; e^{i\omega_n\tau}\langle T_\tau j_i^{(p)}(\mathbf{r}, \tau)j_j^{(p)}(\mathbf{r}', 0)\rangle. \tag{3.6}$$

To obtain the conductivity we consider an external electric field and change variables $E_i = -\partial_t a_i$ to obtain

$$\sigma(\omega) = i\left[\frac{K^{(M)}(i\omega_n, \mathbf{p} = 0)}{i\omega_n}\right]_{i\omega_n \to \omega + i\delta}. \tag{3.7}$$

Gauge Invariance

The diamagnetic term in (3.5) is not a linear response coefficient, but arises at quadratic order in the external gauge field a_i. Nonetheless, it is needed even at linear order to obtain a well-defined conductivity, as it cancels any contribution from the zero-frequency, zero-momentum linear response term $\Pi_{ij}^{(M)}(i\omega_n = 0, \mathbf{p} = 0)$. Physically, $K_{ij}^{(M)}(i\omega_n = 0, \mathbf{p} = 0) = 0$ since a pure gauge configuration of a_i cannot induce a current. Here we show that this cancellation explicitly occurs at the one-loop level; the proof naturally generalizes to the higher loops.

The diamagnetic term can be computed directly

$$\langle j_i^{(d)}(\mathbf{r})\rangle = -2e^2 c\,[A_{ij}]_{ab}\,\langle \psi_a^*\psi_b\rangle\,a_j(\mathbf{r}), \tag{3.8}$$

$$= -2e^2 c\,\lim_{\tau \to 0^+}T\sum_{\varepsilon_n}\int\frac{\mathrm{d}^d p}{(2\pi)^3}\,[A_{ij}]_{ab}\,(-1)G_{ba}^{(M)}(i\varepsilon_n, \mathbf{p})e^{-i\varepsilon_n\tau}, \tag{3.9}$$

where we have introduced the free Matsubara Green function from (2.47)

$$G^{(M)}_{ab}(i\varepsilon_n, \mathbf{p}) = \left[\frac{1}{i\varepsilon_n - cA_{ij}p_ip_j} \right]_{ab} = \frac{i\varepsilon_n\delta_{ab} + c\left[A_{ij}\right]_{ab}p_ip_j}{(i\varepsilon_n)^2 - c^2p^4}. \qquad (3.10)$$

At the free level

$$\nabla_{p_i}G^{(M)}_{ab}(i\varepsilon_n, \mathbf{p}) = G^{(M)}_{ac}(i\varepsilon_n, \mathbf{p})(2\left[A_{ik}\right]_{cd}p_k)G^{(M)}_{db}(i\varepsilon_n, \mathbf{p}). \qquad (3.11)$$

Integrating (3.9) by parts, and using (3.11) gives

$$\langle j_i^{(d)}(\mathbf{r})\rangle = -2e^2c\lim_{\tau\to 0^+}T\sum_{\varepsilon_n}\int\frac{\mathrm{d}^dp}{(2\pi)^3}\left[A_{ij}\right]_{ab}p_iG^{(M)}_{bc}(i\varepsilon_n, \mathbf{p})\cdot$$

$$(2\left[A_{ik}\right]_{cd}p_k)G^{(M)}_{da}(i\varepsilon_n, \mathbf{p})e^{-i\varepsilon_n\tau} \qquad (3.12)$$

which is exactly $-\Pi^{(M)}_{ij}(i\omega_n = 0, \mathbf{p} = 0)$, as required. Equation (3.11) is the statement of the Ward identity for $U(1)$ charge conservation in the free theory. The proof for the interacting case is identical, but now uses the general form of the Ward identity

$$\nabla_{p_i}G^{(M)}_{ab}(i\varepsilon_n, \mathbf{p}) = G^{(M)}_{ac}(i\varepsilon_n, \mathbf{p})\Gamma_{ab,i}(\mathbf{p}, \mathbf{p})G^{(M)}_{db}(i\varepsilon_n, \mathbf{p}) \qquad (3.13)$$

where $\Gamma_{ab,i}(\mathbf{p}, \mathbf{p})$ is the dressed current vertex.

One-Loop Conductivity

With the above set-up, the form of the one-loop electromagnetic response is

$$K_{ij}(i\omega_n, \mathbf{p}) = 4e^2c^2T\sum_{\varepsilon_n}\int\frac{\mathrm{d}^dq}{(2\pi)^d}\left[\frac{\mathrm{tr}\left\{A_{im}q_m(i\varepsilon_n + i\omega_n + cA_{op}(q + \frac{1}{2}p)_o(q + \frac{1}{2}p)_p)\right.}{\left[(i\varepsilon_n + i\omega_n)^2 - c^2\left|\mathbf{q} + \frac{1}{2}\mathbf{p}\right|^4\right]}\cdot\right.$$

$$\left.\cdot\frac{A_{jn}q_n(i\varepsilon_n + cA_{kl}(q - \frac{1}{2}p)_k(q - \frac{1}{2}p)_l)\right\}}{\left[(i\varepsilon_n)^2 - c^2\left|\mathbf{q} - \frac{1}{2}\mathbf{p}\right|^4\right]} - (\omega_n = 0, \mathbf{p} = 0)\right] \qquad (3.14)$$

where $(\omega_n = 0, \mathbf{p} = 0)$ is the diamagnetic term. Note that the $\omega_n \to 0$ limit and the Matsubara summation do not commute, due to the coalescing of poles. This reflects at a technical level the difference between the regimes $\omega/T \gg 1$ and $\omega/T \ll 1$. Setting $\mathbf{p} = 0$, performing the Matsubara sums, and Wick rotating to real frequencies gives the conductivity

$$\sigma_{ij}(\omega) = i\delta_{ij}cr_d e^2 \int \frac{\mathrm{d}^d q}{(2\pi)^d} \left[\frac{(\omega + i\delta)\tanh(cq^2/(2T))}{(\omega + i\delta)^2 - 4c^2 q^4} + \frac{1}{\omega + i\delta} \cdot \frac{cq^2}{dT\cosh^2(cq^2/(2T))} \right]$$
(3.15)

Note that we have to be careful with the causal $i\delta$ terms. To proceed, we use the Sokhotski-Plemelj formula

$$\frac{1}{\omega \pm i\delta} = \mathrm{PP}\frac{1}{\omega} \mp i\pi\delta(\omega)$$
(3.16)

The real part of the conductivity is made from two parts (Figure 3.1). The first, corresponds to the finite frequency response due to inter-band transitions between the conduction and valance band

$$\sigma_{ij}^{(I)}(\omega) = -\frac{\delta_{ij}cr_d e^2}{2} \int \frac{\mathrm{d}^d q}{(2\pi)^d} \tanh\left(\frac{cq^2}{2T}\right) \mathrm{Im}\left[\frac{1}{\omega + i\delta - 2cq^2} + \frac{1}{\omega + i\delta + 2cq^2} \right],$$
(3.17)

$$= \frac{\pi\delta_{ij}cr_d e^2}{4(4\pi)^{d/2}\Gamma(d/2)} \left(\frac{|\omega|}{2c}\right)^{(d-2)/2} \tanh\left(\frac{|\omega|}{4T}\right).$$
(3.18)

In the limit $T \to 0$ this is simply

$$\sigma_{ij}(\omega) = \frac{\pi\delta_{ij}cr_d e^2}{4(4\pi)^{d/2}\Gamma(d/2)} \left(\frac{|\omega|}{2c}\right)^{(d-2)/2}.$$
(3.19)

Since the band-structure does not have a gap, the edge of the inter-band spectrum reaches $\omega = 0$. The scaling of the frequency is exactly what we expect from (2.44). In d dimensions, the fields $\psi(\mathbf{x}, t)$ scale as $+d/2$, so the current scales as $d + 1$ and the conductivity scales as $(d - 2)/2$.

In contrast, the second contribution to the conductivity only occurs at finite T and comes from thermally excited electrons moving ballistically ($\omega = 0$) through the sample without relaxation:

$$\sigma_{ij}^{(II)}(\omega) = \delta(\omega)\pi\delta_{ij}cr_d e^2 \int \frac{\mathrm{d}^d q}{(2\pi)^d} \left[\frac{cq^2}{dT\cosh^2(cq^2/(2T))} \right],$$
(3.20)

$$= \delta(\omega)\delta_{ij} \frac{2\pi cr_d e^2 \zeta(d/2)(1 - 2^{1-d/2})}{(4\pi)^{d/2}} \left(\frac{T}{c}\right)^{d/2}.$$
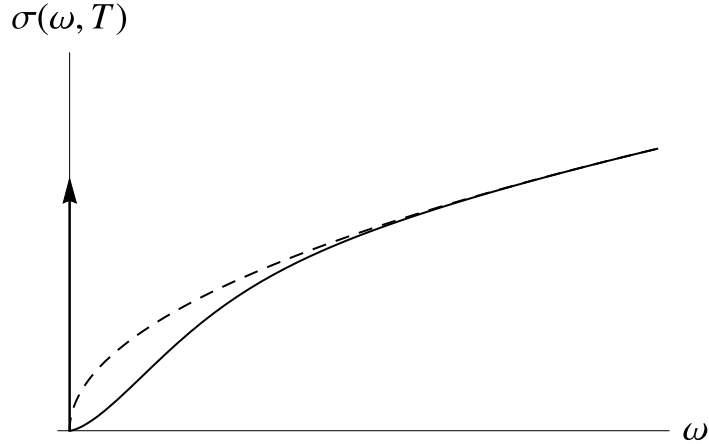(3.21)

$$\sigma(\omega, T)$$

Figure 3.1: Schematic of one-loop conductivity $\sigma(\omega, T)$ in $d = 3$ as a function of ω at a finite T [solid line; the arrow indicates the presence of $\delta(\omega)$ at finite T]. The $T = 0$ result is showed as a dashed line.

Collision-less Kinetic Equation

We will now reproduce the results of the one-loop calculation above using the collision-less kinetic equation. Define the distribution function

$$f_{ab}(t, \mathbf{R}, \mathbf{p}) = \int \frac{d\omega}{2\pi} \int d^D r \ \left\langle c_b^\dagger (R + \tfrac{1}{2}r) c_a (R - \tfrac{1}{2}r) \right\rangle e^{-ip \cdot r} \tag{3.22}$$

here $p = (\omega, \mathbf{p})$, $R = (t, \mathbf{R})$, and $r = (t', \mathbf{r})$; the integral over ω sets $t = t'$. The kinetic equation for $f_{ab}(t, \mathbf{p})$ in a uniform external field without collision is just given by the streaming term

$$\frac{d f_{ab}}{dt} = \frac{\partial f_{ab}}{\partial t} - i \left[f, c A_{ij} p_i p_j \right]_{ab} + e\mathbf{E} \cdot \frac{\partial f_{ab}}{\partial \mathbf{p}} = 0. \tag{3.23}$$

The second term arises from the commutator in the Heisenberg equation of motion for the density matrix – this does not just reduce to the classical Poisson bracket because of the matrix structure. Since the system here is spatially uniform, we can rotate to the band (m) basis using (2.9) and (2.10), giving

$$f_{mm'}(t, \mathbf{p}) = \left[u_m^\dagger(\mathbf{p}) \right]_a f_{ab}(t, \mathbf{p}) \left[u_m(\mathbf{p}) \right]_b. \tag{3.24}$$

The form of the paramagnetic current (3.4) in this basis is $\mathbf{j} = \mathbf{j}_1 + \mathbf{j}_2$, where

$$\mathbf{j}_1 = 2ec \sum_m \int \frac{\mathrm{d}^3 k}{(2\pi)^3} \mathbf{k} \left(m^2 - \tfrac{5}{4} \right) c_m^\dagger(\mathbf{k}) c_m(\mathbf{k}) \tag{3.25}$$

$$\hat{\mathbf{n}} \cdot \mathbf{j}_2 = 2ec \sum_{\sigma=\pm} \sqrt{\frac{3}{2}} \int \frac{\mathrm{d}^3 k}{(2\pi)^3} |\mathbf{k}| \left(\sigma T_\sigma(\hat{\mathbf{n}}) c_{\sigma 3/2}^\dagger(\mathbf{k}) c_{\sigma 1/2}(\mathbf{k}) + h.c. \right) \tag{3.26}$$

Writing the distribution function in terms of the equilibrium value and perturbations by the electric field gives

$$f_{mm'}(\omega, \mathbf{k}) = 2\pi \delta(\omega) f^{(0)}(\sigma_m c p^2) \delta_{mm'} + f_{mm'}^{(1)}(\omega, \mathbf{p}) \tag{3.27}$$

where $\sigma_m = m^2 - 5/4$ denotes the conduction $(+1)$ or valance (-1) nature of the excitation. We now have to distinguish the cases of the diagonal distribution functions, describing the motion of particles within a band, and the off-diagonal distribution describing inter-band transitions.

For the diagonal distribution functions $m = m'$ and so

$$-i\omega f_{mm}^{(1)} + e(\mathbf{E} \cdot \mathbf{p}) \sigma_m c \left[\frac{\partial f^0(\varepsilon)}{\partial \varepsilon} \right]_{\varepsilon = \sigma_m c p^2} = 0 \tag{3.28}$$

where we do not sum in m. This has a solution

$$f_{mm}^{(1)}(\omega, \mathbf{p}) = \frac{2\sigma_m c e (\mathbf{E} \cdot \mathbf{p})}{-i\omega + \eta} \cdot \frac{1}{4T \cosh^2(cp^2/2T)} \tag{3.29}$$

where η is a small damping factor introduced in the time derivative. From (3.25), we find the conductivity

$$\sigma(\omega) = \frac{e^2 c r_d \delta_{ij}}{-i\omega + \eta} \int \frac{\mathrm{d}^d p}{(2\pi)^d} \frac{c p^2}{dT \cosh^2(cp^2/2T)}, \tag{3.30}$$

where we generalize to d dimensions and let $\sum_m 1 = r_d$. This is exactly the second term in (3.15), which we denoted $\sigma^{(II)}(\omega)$.

For the off-diagonal distribution functions $(m \neq m')$ only transition between the conduction and valance band occur, so $\sigma_m = -\sigma_{m'}$ with distribution function

$$f_{mm'}^{(1)} = -ie\mathbf{E} \cdot \left\{ \left[u_{m'}^\dagger \right]_a \frac{\partial [u_m]_a}{\partial \mathbf{p}} \right\} \frac{f^{(0)}(\sigma_m c p^2) - f^{(0)}(-\sigma_m c p^2)}{\omega - 2c p^2 \sigma_m} \tag{3.31}$$

This contribution needs a more careful evaluation of the matrix elements and we will not generalize to arbitrary dimension d here. Let $\mathbf{E} = E\hat{\mathbf{z}}$ and define

$$\Theta_{m'm} = p \left[u_{m'}^\dagger \right]_a \frac{\partial [u_m]_a}{\partial p_z} = -i(\hat{\mathbf{p}} \times \hat{\mathbf{z}}) \cdot \langle m' | \mathbf{J} | m \rangle \tag{3.32}$$

So

$$\Theta_{1/2,3/2} = \sqrt{\tfrac{3}{2}}(\hat{\mathbf{e}}_+ \cdot \hat{\mathbf{p}}) = -\Theta^*_{3/2,1/2} \tag{3.33}$$

$$\Theta_{-1/2,-3/2} = \sqrt{\tfrac{3}{2}}(\hat{\mathbf{e}}_- \cdot \hat{\mathbf{p}}) = -\Theta^*_{-3/2,-1/2} \tag{3.34}$$

The contribution to the current (3.26) gives the conductivity

$$\sigma^{(I)}_{ij}(\omega) = 4ie^2 c\delta_{ij} \int \frac{\mathrm{d}^3 p}{(2\pi)^3} \tanh\left(\frac{cp^2}{2T}\right) \frac{\omega}{\omega^2 - 4c^2 p^4}. \tag{3.35}$$

With the replacement $\omega \to \omega + i\eta$ and $r_d = 4$, this is exactly the first term in (3.15), which gave rise to $\sigma^{(I)}(\omega)$.

Finally, it is important to note that the kinetic equation has manifest gauge invariance and, unlike in the calculation for the Kubo formula (3.5), we did not need to include the diamagnetic term.

3.2   Shear Viscosity

The shear viscosity is the transport coefficient which characterizes the relaxation of a transverse momentum gradient back to local equilibrium. Considering slow variations of the local momentum $\mathbf{P}(\mathbf{x})$ on a length-scale much larger than the mean free path, the leading dissipative contribution to the stress tensor T_{ij} defines the viscosities. For a pure shear flow

$$\Delta T_{ij} = -\eta \left[\frac{\partial V_i}{\partial x_j} + \frac{\partial V_j}{\partial x_i} - \frac{2}{d}\delta_{ij}(\partial_k V_k) \right], \tag{3.36}$$

where for the LAB model (2.40) with $f = 0$ we can identify the velocity $\mathbf{V} = 2c\mathbf{P}$. Being linear response coefficients, the viscosities can be written in terms of a Kubo formula [70]

$$\eta_{ijkl}(\omega) = \frac{X_{ijkl}(\omega)}{L^d} + \frac{i}{\omega^+}\delta_{ij}\delta_{kl}\left(p + L^d \frac{\partial p}{\partial L^d} \right), \tag{3.37}$$

$$X_{ijkl}(\omega) = \frac{1}{\omega^+}\left\langle \left[\widetilde{T}_{ij}(0), J_{kl}(0) \right] \right\rangle + \frac{1}{\omega^+} \int\limits_0^\infty \mathrm{d}t \, e^{i\omega^+ t} \left\langle \left[\widetilde{T}_{ij}(t), \widetilde{T}_{kl}(0) \right] \right\rangle. \tag{3.38}$$

here $\omega^+ = \omega + i\delta$ with $\delta \to +0$, p is the pressure of the system, L^d the volume of the system. The integrated stress tensor is

$$\widetilde{T}_{ij} = \int \mathrm{d}^d x \ T_{ij}. \tag{3.39}$$

Additionally, J_{ij} are strain generators defined by

$$J_{ij} = -\int \mathrm{d}^d x \ x_i p_j, \tag{3.40}$$

where p_j is the momentum density. We are only interested in the shear flow (3.36), which is the traceless component of the symmetric part of the total viscosity tensor

$$\eta_{ijkl} = \eta \left(\delta_{ik}\delta_{jl} + \delta_{il}\delta_{jk} - \frac{2}{d}\delta_{ij}\delta_{kl} \right) + \ldots \tag{3.41}$$

We will therefore not need to consider the pressure corrections in equation (3.37). The $\sim \langle [\tilde{T}, J] \rangle$ term in (3.38), however, is a contact term analogous to the diamagnetic term in the calculation for the conductivity. In general, we will have to include it to obtain the correct form of the response function.

An important, but subtle problem which arises when using the Kubo formula for viscosity is that the stress tensor is in general not uniquely defined. The space and time translational symmetry imply that the energy-momentum tensor $t^{\mu\nu}$ is conserved through Noether's theorem

$$\partial_\mu t^{\mu\nu} = 0. \tag{3.42}$$

Here μ is a space-time index. The energy density $\mathscr{H} = t_{00}$, the momentum density $p_i = t_{i0}$ and the stress tensor $T_{ij} = t_{ij}$. However, we can change ('improve') the energy-momentum tensor

$$t_{\mu\nu} \to t_{\mu\nu} + \partial_\rho b_{\rho\mu\nu}, \tag{3.43}$$

Provided $b_{\rho\mu\nu} = -b_{\mu\rho\nu}$, this change does not affect the conservation law (3.42). The different choices of improvements are physical – they correspond to different microscopic ways the system can respond to a strain.

LAB Stress Tensor

We will use choose a stress tensor for the LAB phase that is symmetric in the indices ij, which can be done due to the emergent rotation invariance of the model. The Noether stress energy tensor is

$$t^{00} = c \left[A_{ij}\right]_{ab} (\partial_i \psi_a^*)(\partial_j \psi_b), \tag{3.44}$$

$$t^{0i} = -\tfrac{1}{2}i \left(\psi_a^* \partial_i \psi_a - (\partial_i \psi_a^*)\psi_a\right), \tag{3.45}$$

$$t^{i0} = -c \left[A_{ik}\right]_{ab} \left[(\partial_k \psi_a^*)(\partial_t \psi_b) + (\partial_t \psi_a^*)(\partial_k \psi_b)\right], \tag{3.46}$$

$$t^{ij} = c \left[A_{ik}\right]_{ab} (\partial_k \psi_a^* \partial_j \psi_b + \partial_j \psi_a^* \partial_k \psi_b) + \delta^{ij}\mathscr{L}, \tag{3.47}$$

where

$$\mathscr{L} = \frac{1}{2}\left[i\psi_a^*(\partial_t \psi_a) - i(\partial_t \psi_a^*)\psi_a\right] - ea_0 \psi_a^* \psi_a - c \left[A_{ij}\right]_{ab}(\partial_i \psi_a^*)(\partial_j \psi_b), \tag{3.48}$$

is the time-symmetrized Lagrangian. Since t^{ij} is a physical current, we may evaluate it on-shell using the equation of motion, which imply that $\mathscr{L} = 0$, giving the integrated stress tensor

$$\widetilde{t}_{ij} = \int \mathrm{d}^d x \, c \left[A_{ik}\right]_{ab}(\partial_k \psi_a^* \partial_j \psi_b + \partial_j \psi_a^* \partial_k \psi_b). \tag{3.49}$$

Since this form of the stress tensor is not symmetric, we will add the improvement to obtain the final form of the stress tensor

$$p^i = t^{0i} + \tfrac{1}{2}\varepsilon_{ijk}\partial_j s_k, \tag{3.50}$$

$$T^{ij} = t^{ij} - \tfrac{1}{2}\varepsilon_{ijk}\partial_t s_k, \tag{3.51}$$

where

$$s_k = -c \, \psi_a^* \left[J_k\right]_{ab} \psi_b. \tag{3.52}$$

The strain generators are

$$J_{ij} = \frac{i}{2}\int \mathrm{d}^d x \, x_i \left[\psi_a^*(\partial_j \psi_a) - (\partial_j \psi_a^*)\psi_a\right] - \frac{c}{2}\varepsilon_{ijk}\int \mathrm{d}^d x \, \psi_a^* \left[J_k\right]_{ab} \psi_b. \tag{3.53}$$

In the band (m) basis using (2.9) and (2.10) the form of the integrated stress tensor is $\widetilde{T}_{ij}^{(1)} + \widetilde{T}_{ij}^{(2)}$, where

$$\widetilde{T}_{ij}^{(1)} = c\sum_\sigma \int \frac{\mathrm{d}^d k}{(2\pi)^d} 2k_i k_j \left(c_{\sigma 3/2}^\dagger(\mathbf{k})c_{\sigma 3/2}(\mathbf{k}) - c_{\sigma 1/2}^\dagger(\mathbf{k})c_{\sigma 1/2}(\mathbf{k})\right), \tag{3.54}$$

$$\widetilde{T}_{ij}^{(2)} = c\sqrt{\frac{3}{2}}\sum_\sigma \int \frac{\mathrm{d}^d k}{(2\pi)^d} k \left([\sigma T_\sigma(\hat{\mathbf{e}}_i)k_j + \sigma T_\sigma(\hat{\mathbf{e}}_j)k_i] c_{\sigma 3/2}^\dagger(\mathbf{k})c_{\sigma 1/2}(\mathbf{k}) + h.c.\right). \tag{3.55}$$

Here $\hat{\mathbf{e}}_i$ is the unit vector in the i direction.

One-Loop Viscosity

We now proceed to calculate the one-loop viscosity response function for the LAB band-structure. The contact term $\langle [T, J] \rangle$ can be calculated directly and vanishes. The imaginary time correlator of the stress tensor is

$$\chi^{(M)}_{ijkl}(i\omega_n) = \frac{1}{2} \int_{-\beta}^{\beta} \mathrm{d}\tau \; e^{i\omega_n \tau} \left\langle T_\tau \widetilde{T}_{ij}(\tau) \widetilde{T}_{kl}(0) \right\rangle, \tag{3.56}$$

$$= -c^2 L^d \int \frac{\mathrm{d}^d k}{(2\pi)^d} T \sum_{\varepsilon_n} \mathrm{tr}\left[(A_{iq} k_q k_j + A_{jq} k_q k_i) \right.$$
$$\left. G^{(M)}(i\varepsilon_n + i\omega_n, \mathbf{k})(A_{kr} k_r k_l + A_{lr} k_r k_k) G^{(M)}(i\varepsilon_n, \mathbf{k}) \right]. \tag{3.57}$$

As in the case of the conductivity, performing the Matsubara summation gives rise to two contributions – a finite frequency inter-band response and a zero-frequency delta function response. At finite frequencies

$$\chi^{(M)}_{ijkl}(i\omega_n) = \frac{2c^3 L^d r_d d}{d^2 + d - 2} \left(\delta_{il}\delta_{jk} + \delta_{ik}\delta_{jl} - \frac{2}{d}\delta_{ij}\delta_{kl} \right) \int \frac{\mathrm{d}^d q}{(2\pi)^d} \frac{q^6 \tanh(cq^2/2T)}{\omega_n^2 + 4c^2 q^4}, \tag{3.58}$$

so the viscosity only has a shear contribution. Wick rotating to real frequencies

$$\eta^{sh}(\omega) = \frac{2ic^3 L^d r_d d}{(d^2 + d - 2)(\omega + i\delta)} \int \frac{\mathrm{d}^d q}{(2\pi)^d} \frac{q^6 \tanh(cq^2/2T)}{(\omega + i\delta)^2 - 4c^2 q^4}, \tag{3.59}$$

gives rise to shear viscosity caused by inter-band transitions

$$\eta^{sh,(I)}(\omega) = \frac{\pi r_d d}{4(d^2 + d - 2)(4\pi)^{d/2}\Gamma(\frac{1}{2}d)} \left(\frac{|\omega|}{2c} \right)^{d/2} \tanh\left(\frac{|\omega|}{4T} \right). \tag{3.60}$$

At $\omega = 0$, the Matsubara summation gives

$$\chi^{(M)}_{ijkl}(0) = \chi^{(M)}_{ijkl}(i\omega_n \to 0) - \frac{2c^2 L^d r_d}{d(d+2)T}(\delta_{ij}\delta_{kl} + \delta_{ik}\delta_{jl} + \delta_{il}\delta_{jk}) \int \frac{\mathrm{d}^d q}{(2\pi)^d} \frac{q^4}{1 + \cosh(cq^2/T)}. \tag{3.61}$$

Here $\chi^{(M)}_{ijkl}(i\omega_n \to 0)$ is the zero frequency limit of (3.58), which does not contribute. The second term is not a pure shear viscosity, due to neglecting the pressure terms in (3.37). Considering only the shear contribution gives

$$\eta^{sh,(II)}(\omega) = \delta(\omega) \frac{2\pi c r_d}{d(d+2)} \left(\frac{T}{c}\right)^{(d+2)/2} \int \frac{\mathrm{d}^d x}{(2\pi)^d} \frac{x^4}{1 + \cosh(x^2)},$$

$$= \delta(\omega) \frac{\pi c r_d}{2(4\pi)^{d/2}} \zeta(\tfrac{1}{2}d + 1) \left(\frac{T}{c}\right)^{(d+2)/2}. \tag{3.62}$$

As was the case for the conductivity (3.21), this term is caused by thermally excited quasi-particles moving ballistically through the sample. Since there is no relaxation from interactions, there is an infinite δ-function shear response.

As in the case of the conductivity, we could have also arrived at this result through a collisionless kinetic equation calculation. We will however, directly develop the kinetic approach in for the interacting system in the next chapter.

Chapter 4

Finite-Temperature Shear Viscosity of the Luttinger-Abrikosov-Beneslavskii Phase

In this chapter, we develop a kinetic equation formalism to describe the d.c. transport properties of the LAB phase, which are dominated by collisions, and compute the shear viscosity η. The ratio of shear viscosity to entropy density η/s is a measure of the strength of interaction between the excitations of a quantum fluid. As a consequence of the quantum critical nature of the system, η/s is a universal number and we find it to be consistent with the bound proposed from gauge-gravity duality.

$$\frac{\eta}{s} \geq \frac{\hbar}{4\pi k_B}. \tag{1.9$'$}$$

In the first part of the chapter, we will discuss the logical structure of the result and discuss its implications. Technical details are presented after the main result.

4.1 Finite-temperature Shear Viscosity in the LAB phase

To understand the transport of the LAB phase at finite temperatures, we emphasize the similarity to a system in the vicinity of a quantum critical point [10]. The long distance behavior of the system is described by a scale invariant, interacting field theory, whose transport properties are described by universal functions. At finite frequencies there are two regimes for the transport coefficients. The collision-less limit $\omega/T \gg 1$ is dominated by particle-hole production; the effect of interactions is small and the

form of η may be found from the RG flow. In contrast, the limit $\omega/T \ll 1$ is dominated by collisions between thermally excited particles and holes. In a non-interacting system, the excited particles move ballistically and give a delta-function peak; this delta function is broadened by the Coulomb interactions. Phenomenologically, we can understand the dc transport properties from a simple mean free time argument. The temperature is the only characteristic energy scale in the problem; the characteristic length scale is $\sim (c/T)^{1/z}$ and the mean free path is $\ell \sim \alpha^{-2}(c/T)^{1/z}$, which includes the dimensionless scattering rate. A simple Drude theory would predict a dc shear viscosity $\eta \sim n\bar{v}\ell/c \sim \alpha^{-2}(T/c)^{d/z}$. The scaling of the temperature is exactly that of the entropy density $s \sim (T/c)^{d/z}$ as expected.

We now develop a kinetic equation approach to calculate the shear viscosity to leading order in the ε-expansion, which will recover the above considerations and also give a numerical estimate for the value of η/s. Formally, the kinetic equation makes use of a semi-classical expansion and assumes quasi-particles which interact locally. It was shown that in the weakly coupled finite-temperature theory of a scalar field [71, 72], the diagrammatic summation in a Kubo calculation using (3.37) matches the results from a high temperature effective kinetic equation. The LAB phase does not contain quasi-particles, but for small ε the quasi-particles become well defined and this approach is justified during the calculation. The long range Coulomb interaction will be screened at finite temperature on the Debye length-scale $\ell_D \sim \sqrt{\alpha T/c}$, which is much less than the mean free path, justifying the local collision term.

We write the fields ψ in terms of particle and hole eigenstates, by performing a particle-hole transformation on the valance band in (2.9)

$$\psi(\mathbf{x}) = \int_{\mathbf{k}} \left[u_\sigma(\mathbf{k})c_\sigma(\mathbf{k})e^{i\mathbf{k}\cdot\mathbf{x}} + v_\sigma(\mathbf{k})h_\sigma^\dagger(\mathbf{k})e^{-i\mathbf{k}\cdot\mathbf{x}} \right] \tag{4.1}$$

where $\sigma = \pm$ is the helicity of the state, $u_\sigma(\mathbf{k}), v_\sigma(\mathbf{k})$ are spinor factors and $\int_{\mathbf{k}} = \int (\mathrm{d}^d k)/(2\pi)^d$. Since we have a four-band model, the most general semi-classical kinetic equation is for a matrix of distribution of functions including both diagonal distribution functions $\sim \langle c_\sigma^\dagger c_\sigma \rangle, \langle h_\sigma^\dagger h_\sigma \rangle$ and distribution function that describe particle-hole pairs $\sim \langle c_\sigma h_{\sigma'} \rangle, \langle c_\sigma^\dagger h_{\sigma'}^\dagger \rangle$. Here, we neglect the latter type of distribution function, since we are interested in the dc limit of the viscosity. Additionally, we shall drop spin-orbit coupling in matrix elements in the equation and neglect scattering in the Mandelstam s-channel, which involves electron-hole annihilation and production. This is justified in a 'leading q' approximation, where the dominant contribution is from particles with small momentum transfer; however, this would tend to overestimate the viscosity. In this limit, the scattering matrix elements are not affected by the spin structure of the theory. We note that at leading order in ε, the details of the RG scheme do not enter the form of the Coulomb interaction and we use the lowest order expression $4\pi\alpha^* c/q^2$ as the interaction between excitations. At this order, the

thermal screening of the interaction is also negligible. Unlike the bare Coulomb interaction in $d = 3$, there is no low-momentum divergence of the collision integral and thermal screening is not needed as a regulator.

With the above conditions, the full quantum kinetic equation encapsulating the non-equilibrium time-evolution of the system, reduces to the usual semi-classical case

$$\left(\partial_t + \mathbf{v} \cdot \partial_\mathbf{x} + \mathbf{F}_{ext} \cdot \partial_\mathbf{k}\right) f^a(t, \mathbf{x}, \mathbf{k}) = -C[f] \tag{4.2}$$

where a labels both the species (electrons or holes) and helicity, $\mathbf{v} = 2c\mathbf{k}$ is the particle velocity and $C[f]$ is the collision term describing two-particle scattering. The method of extracting the viscosity is standard – one considers the slowly varying local momentum as an external disturbance $X_{ij} = \left[\partial_j P_i + \partial_i P_j - (2\delta_{ij}/d)(\partial_k P_k)\right]/2$, assumes this weakly modifies the equilibrium distribution function $f_0(\mathbf{k}) = 1/\left[\exp(ck^2/T) + 1\right]$ and uses this modified distribution function to find the stress tensor T_{ij} and hence η. We linearize the distribution function $f^a(\mathbf{k}) = f_0(\mathbf{k}) + \delta f^a(\mathbf{k})$, where

$$\delta f^a(\mathbf{k}) = \beta[1 - f_0(\mathbf{k})]f_0(\mathbf{k})\chi_{ij}^a(\mathbf{k})X_{ij} \tag{4.3}$$

and $\chi_{ij}^a(\mathbf{k}) = \sqrt{d/(d-1)}\,(k_i k_j - \delta_{ij} k^2/d)\,\chi^a(k)$ has the appropriate symmetry for the shear flow factored out, so that $\chi^a(k)$ is a function of the magnitude k only.
For the stress tensor, we consider the contributions from the diagonal fermion distribution functions

$$T_{ij} = \sum_a \int_\mathbf{k} 2c k_i k_j f_\sigma^a(\mathbf{k}) \tag{4.4}$$

In addition to neglecting the distribution function describing particle-hole creation, we neglect the contribution from the Coulomb interaction between carriers to the stress tensor; we find this to be sub-leading in ε in our approach.

We solve the kinetic equation using a variational approach [19, 73, 74]. The kinetic equation, linearized for χ, can be viewed as an operator equation on function space $|S_{ij}\rangle = C|\chi_{ij}\rangle$. Here S_{ij} corresponds to the streaming term in (4.2); C is an operator encoding the collision term and is Hermitian with respect to an inner product $\langle f, g \rangle = \sum_a \sum_{i,j} \int_\mathbf{k} f_{ij}^a(\mathbf{k}) g_{ij}^a(\mathbf{k})$. Finding the solution $\chi(k)$ of is equivalent to maximizing the functional $Q[\chi] = \langle \chi_{ij}, S_{ij} \rangle - \langle \chi_{ij}, C\chi_{ij} \rangle/2$ with respect to variations in χ. Physically, this means that the realized solution is that which maximizes entropy production subject to the constraints imposed by the external disturbance and subsequent time evolution of the system. We project χ onto a set of 12 basis functions and optimize the coefficients numerically to find the variational approximation; the optimal function is shown in Figure 4.1.

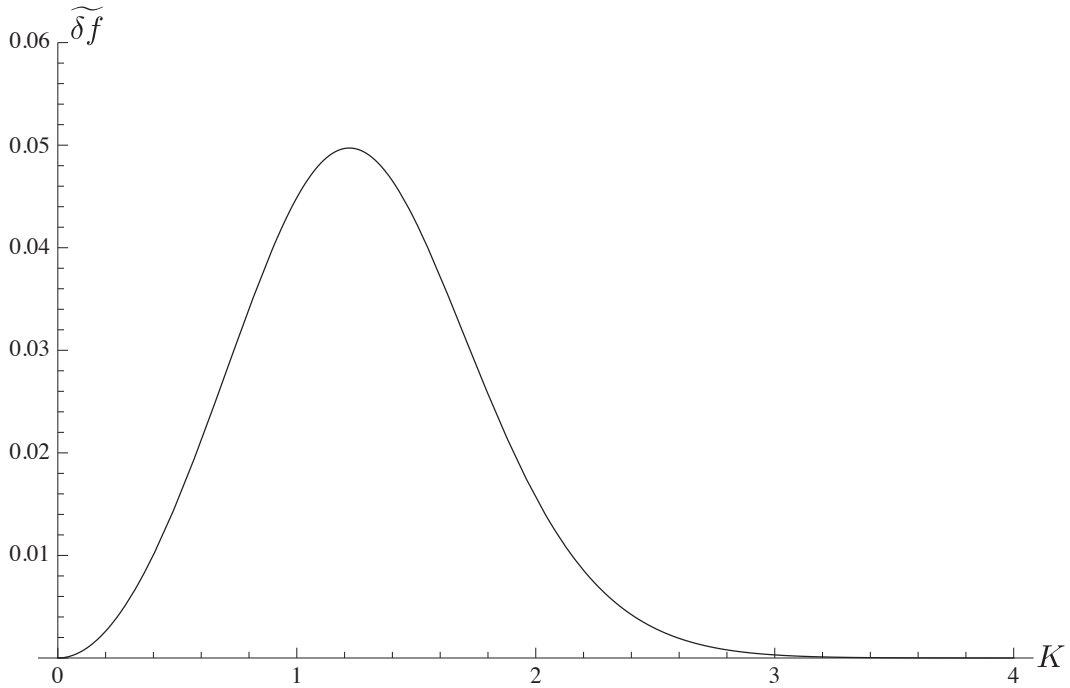Using this solution, we find the viscosity

Figure 4.1: Plot of optimized dimensionless function $\widetilde{\delta f}(K) = -(T(\alpha^*)^2 c) \cdot \chi(K) K^2 [1 - f_0(K)] f_0(K)$ as a function of $K = k\sqrt{T/c}$.

$$\eta \simeq \frac{3.1}{(\alpha^*)^2} \left(\frac{T}{c}\right)^2, \tag{4.5}$$

Since we are calculating η/s to leading order in ε, we can use the entropy density for the unrenormalized band-structure in $d = 4$

$$s = \frac{9\zeta(3)}{16\pi^2} \left(\frac{T}{c}\right)^2, \tag{4.6}$$

along with the fixed point value $\alpha^* = (32\pi/21)\varepsilon$ to finally obtain

$$\frac{\eta}{s} = \frac{0.63}{\varepsilon^2}. \tag{4.7}$$

Setting $\varepsilon = 1$ gives $4\pi\eta/s = 8.0$; consistent with the original bound (1.9'). A priori, there was perhaps reason to believe that this model might strongly violate the original bound, given the unusual properties of the LAB phase – strong interactions, both particle and hole carriers, no Galilean invariance and an anomalous scaling z with softer excitations than in a relativistic system. The value of $\eta/s \simeq 0.63$ is, however,

similar to the values found in the unitary Fermi gas ($\eta/s \leq 0.5$) or in the quark-gluon plasma ($\eta/s \leq 0.4$) [47].

The LAB phase only emerged with the chemical potential at the Γ_8 degeneracy point, so the system lacked a Fermi surface. Changing the chemical potential away sufficiently, we expect to recover the usual Fermi liquid behavior. For a Fermi liquid $\eta/s \sim (\varepsilon_F/T)^3$ is temperature dependent [75]; in this limit the quasi-particles are well defined and weakly interacting. By comparison, graphene with Coulomb interactions is described by a field theory with marginally irrelevant interactions, but stays in a scaling regime for a large range of energies [76, 77]. The ratio $\eta/s \sim 1/\alpha(T)^2$ has a form similar to the quantum critical case (4.7), except that the effective coupling constant $\alpha(T) \sim 1/\log(T_\Lambda/T)$ ultimately renormalizes to zero as $T \to 0$ [51]. In both of these cases, η/s diverges as $T \to 0$ in contrast to the universal ratio obtained for the LAB phase.

Throughout our analysis, we have worked in the ε-expansion to retain analytic control, both for the description of the RG flow and the kinetic equation calculation. The use of the ε-expansion is well established [4, 6]. Determining its accuracy for finite temperature transport coefficients in quantum critical systems by comparison to numerical simulations is an active research area for which we refer to the literature [10, 78, 79]. The extrapolation to the physical dimension is, however, always a sensitive matter and relies on the fixed point evolving smoothly as $\varepsilon \to 1$. This may fail if there is interference from another fixed point. While there is no other fixed point at small ε, it was suggested in [61] that such a fixed point might arise at strong coupling and destabilize LAB phase for the physical dimension $d = 3$; this is still an open question [80].

Finally, we want to briefly comment on the experimental implications of the above discussion. In order to define the viscosity, the mean free path of effects which violate momentum conservation, such as disorder or umklapp processes, must be much larger than the mean free path of electron-electron interaction. This hydrodynamic regime is generally difficult to access in a solid state system, although, for example, recent experiments in $PdCoO_2$ observe very low resistivity and a temperature behavior consistent with phonon drag [81]. In this regime, we might expect the viscosity to dominate the damping of acoustic waves and also to observe viscous drag effects, which may be a route to accessing η. Alternatively, the possibility of more dramatic signatures due to electronic turbulence has been suggested in low viscosity phases [51]; the LAB phase would be a prime candidate for searching for such effects. Overall, we anticipate that the hydrodynamic regime will become increasingly important in the study of solid state systems.

4.2 Variational Solution of the Kinetic Equation

Within the approximations discussed above, the kinetic equation with interaction reduces to the semi-classical kinetic equation for the diagonal distribution functions

$$(\partial_t + \mathbf{v_k} \cdot \partial_\mathbf{x} + \mathbf{F}_{ext} \cdot \partial_\mathbf{k}) f^a(t, \mathbf{x}, \mathbf{k}) = -C[f^a] \tag{4.8}$$

The collision term is

$$C[f] = \frac{1}{2} \sum_{bcd} \int_{\mathbf{p'},\mathbf{k},\mathbf{k'}} |M_{ab}^{cd}(\mathbf{p}, \mathbf{k}, \mathbf{p'}, \mathbf{k'})|^2 \cdot$$
$$(2\pi)^{d+1} \delta(\varepsilon_\mathbf{p} + \varepsilon_\mathbf{k} - \varepsilon_{\mathbf{p'}} - \varepsilon_{\mathbf{k'}}) \delta^d(\mathbf{p} + \mathbf{k} - \mathbf{p'} - \mathbf{k'}) \cdot$$
$$\left\{ f^a(\mathbf{p}) f^b(\mathbf{k})[1 - f^c(\mathbf{p'})][1 - f^d(\mathbf{k'})] - f^c(\mathbf{p'}) f^d(\mathbf{k'})[1 - f^a(\mathbf{p})][1 - f^b(\mathbf{k})] \right\} \tag{4.9}$$

The matrix terms are given by the tree-level scattering processes $ab \to cd$. As stated in the main text, we shall neglect scattering processes in the s-channel (involving particle-hole annihilation and reformation). To find the transport coefficients, we look for perturbations about equilibrium

$$f^a(\mathbf{k}) = f_0(\mathbf{k}) + \beta[1 - f_0(\mathbf{k})] f_0(\mathbf{k}) \chi^a(k) I_{ij\ldots}(\mathbf{k}) X_{ij\ldots} \tag{4.10}$$

where $X_{ij\ldots}$ is the external driving force appropriate for the transport coefficient under consideration, $I_{ij\ldots}(\mathbf{k})$ is tensor appropriate for the symmetry of the driving force and $\chi(k)$ the perturbed distribution function. We also introduce the short-hand $\chi_{ij\ldots}(\mathbf{k}) = I_{ij\ldots}(\mathbf{k})\chi(k)$. We shall keep this generality for the moment, and focus on the case of shear viscosity later. For both particles and holes, the equilibrium distribution function is $f_0(\mathbf{k}) = 1/[\exp(ck^2/T) + 1]$. Explicitly

$$Q[\chi] = -\sum_a \int_\mathbf{k} f_0(\mathbf{k})[1 - f_0(\mathbf{k})] \beta q^a \chi^a(k)$$
$$- \frac{\beta}{16} \sum_{abcd} \int_{\mathbf{k},\mathbf{p},\mathbf{k'},\mathbf{p'}} |M_{ab}^{cd}(\mathbf{p}, \mathbf{k}, \mathbf{p'}, \mathbf{k'})|^2 f_0(\mathbf{p}) f_0(\mathbf{k})[1 - f_0(\mathbf{p'})][1 - f_0(\mathbf{k'})] \cdot$$
$$(2\pi)^{d+1} \delta(\varepsilon_\mathbf{p} + \varepsilon_\mathbf{k} - \varepsilon_{\mathbf{p'}} - \varepsilon_{\mathbf{k'}}) \delta^d(\mathbf{p} + \mathbf{k} - \mathbf{p'} - \mathbf{k'}) \cdot$$
$$\left\{ \chi_{ij\ldots}^a(\mathbf{p}) + \chi_{ij\ldots}^b(\mathbf{k}) - \chi_{ij\ldots}^c(\mathbf{p'}) - \chi_{ij\ldots}^d(\mathbf{k'}) \right\}^2 \tag{4.11}$$

where we used detailed balance to make manifest that C is hermitian. Here q^a are 'charge factors'; in the case of the shear viscosity $q^a = k^4$ for all species. The above

rewrite also gives rise to the factor $1/8$ to stop overcounting of $a \leftrightarrow b$ and $ab \leftrightarrow cd$ processes.

We maximize $Q[\chi]$ by projecting the function $\chi(k) = \sum_\mu a_\mu F_\mu(k)$ onto a set of basis functions $F_\mu(k)$. Maximizing Q then reduces to the solution of matrix equation

$$\sum_\nu C_{\mu\nu} a_\nu = b_\mu \tag{4.12}$$

for a_ν. From now on we set $d = 4$, since we are working in the ε-expansion and interesting in the dominant ε term. We also denote by $\mathbf{P}, \mathbf{K}, \mathbf{Q}$ the scaled momenta $\mathbf{P} = \mathbf{p}\sqrt{c/T}$. We defin $\mathbf{q}$ such that $\mathbf{p}' = \mathbf{p} + \mathbf{q}$ and $\mathbf{k}' = \mathbf{k} - \mathbf{q}$; we perform the $\mathbf{k}'$ integral to remove the delta function in momentum and replace the $\mathbf{p}'$ integration by a $\mathbf{q}$ integration. We rewrite the delta function enforcing energy conservation during scattering as

$$\delta(\varepsilon_{\mathbf{p}} + \varepsilon_{\mathbf{k}} - \varepsilon_{\mathbf{p}'} - \varepsilon_{\mathbf{k}'})$$

$$= \frac{2Q}{c} \cdot \frac{c}{T} \int_{-\infty}^{\infty} dy \, \delta(K^2 - |\mathbf{K} - \mathbf{Q}|^2 - 2Qy)\delta(P^2 - |\mathbf{P} + \mathbf{Q}|^2 + 2Qy) \tag{4.13}$$

$$= \frac{2Q}{T \cdot (2KQ)(2PQ)} \int_{y_0}^{y_1} dy \, \delta\left(\cos\theta_{KQ} - \frac{2y + Q}{2K}\right) \delta\left(\cos\theta_{PQ} - \frac{2y - Q}{2P}\right) \tag{4.14}$$

where $y_0 = \min[P+Q/2, K-Q/2]$ and $y_1 = \max[-P+Q/2, -K-Q/2]$ are restrictions imposed so that the cosines are defined.

Unlike usual 'leading-q' expansions [74], we only modify the matrix elements – dropping the spin structure as well as particle-hole creation processes – but do not expand the functions $\chi_{ij}(\mathbf{p}'), \chi_{ij}(\mathbf{k}')$ in $\mathbf{q}$ nor set $\mathbf{q} = 0$ in the Fermi functions. After performing the angular integrals analytically, we are left with a four-dimensional integral (over k, q, p, y) to calculate $C_{\mu\nu}$, which we perform numerically using the cubature algorithm Cuhre of the Cuba library [82].

To find the shear viscosity we apply a divergence-free background flow pattern of momentum $\mathbf{P}(\mathbf{x})$ with $\partial_k P_k = 0$:

$$X_{ij} = \frac{1}{2}\left(\frac{\partial P_j}{\partial x_i} + \frac{\partial P_i}{\partial x_j}\right) \tag{4.15}$$

$$I_{ij}(\mathbf{k}) = \sqrt{\frac{d}{d-1}}\left(k_i k_j - \frac{1}{d}\delta_{ij}k^2\right) \tag{4.16}$$

and solve the kinetic equation for χ. The shear viscosity can then be found from the stress tensor

$$T_{ij} = -\eta \left(\delta_{ik}\delta_{jl} + \delta_{il}\delta_{jk}\right) 2cX_{ij} = \sum_a \int_{\mathbf{k}} 2ck_i k_j f^a(\mathbf{k}) \tag{4.17}$$

Due to the symmetry of the diagonal part of the stress tensor under particle and hole exchange, the function $\chi(k)$ will be the same for particles and holes. The charge factors $q^a = k^4$ for all species. In the low-q approximation for a matrix element, the sum entering the kinetic equation functional is $\sum_{abcd}|M_{ab}^{cd}(\mathbf{p},\mathbf{k},\mathbf{p}',\mathbf{k}')|^2 = r_d^2 \cdot (4\pi\alpha^*c/q^2)^2$, taking into account the exchange symmetry and over-counting factors. We define the dimensionless scaling function

$$\Phi(K) = \frac{T(\alpha^*)^2}{c} \cdot \chi\left(k\sqrt{\frac{T}{c}}\right) \tag{4.18}$$

which we expand onto a set of basis functions $\Phi(K) = \sum_\mu a_\mu F_\mu(K)$. We choose

$$F_\mu(K) = \left[1 + e^{-K^2}\right]^2 L_\mu^{(3)}(K^2) \tag{4.19}$$

where $L_\mu^{(3)}(x)$ are associated Laguerre polynomials. The choice of Laguerre polynomials is well known from the case of transport in a Boltzmann gas [19] – it simplifies the form of b_μ to

$$b_\mu = \frac{r_4}{16\pi^2(\alpha^*)^2}\left(\frac{T}{c}\right)^2 \frac{18}{\sqrt{3}}\delta_{\mu,0} \tag{4.20}$$

due to the orthogonality properties of the Laguerre polynomials. These basis functions also give a reasonably well conditioned matrix $C_{\mu\nu}$ which can easily be evaluated and inverted numerically. We use a set of 12 basis functions. Performing the variational solution gives

$$\eta = -\frac{r_d}{16\pi^2(\alpha^*)^2}\left(\frac{T}{c}\right)^2 \frac{1}{3\sqrt{3}}\int_0^\infty dK\; f_0(K)[1-f_0(K)]K^7\Phi(K) \tag{4.21}$$

$$= -\frac{r_d}{16\pi^2(\alpha^*)^2}\left(\frac{T}{c}\right)^2 \frac{a_0}{\sqrt{3}} \simeq \frac{3.14}{(\alpha^*)^2}\left(\frac{T}{c}\right)^2 \tag{4.22}$$

with $r_d = 4$. This is the result given in the main text.

4.3 Coulomb Contribution to Stress Tensor

In addition to the contribution of the electrons and holes given in (3.54) and (3.55), the stress tensor has a contribution from the Coulomb interaction

$$T_{ij}^{(int)} = -\frac{1}{4\pi e^2} \int \frac{\mathrm{d}^4 k}{(2\pi)^4} \left[k_i k_j - \frac{1}{2}\delta_{ij} k^2 \right] \langle \varphi(\mathbf{k})\varphi(-\mathbf{k}) \rangle \tag{4.23}$$

where by the average $\langle \varphi(k)\varphi(-k) \rangle$ we mean the semi-classical limit of the correlator evaluated in the non-equilibrium case. We will argue in our approach that the above term is of higher order in ε and can be neglected in our calculation of η. Since the Coulomb interaction is non-dynamic, the contribution to the viscosity when we apply a background momentum $\mathbf{P}(\mathbf{x})$ will be through loop corrections involving the fermions. We shall use the results we found from the Boltzmann equation so that our answer is self-consistent. We can show in Keldysh perturbation theory [19, 83–85], that for the scalar interaction

$$\langle \varphi(x_1)\varphi(x_2) \rangle = -D^R(x_1, x_3)\Pi^{-+}(x_3, x_4)D^A(x_4, x_2) \tag{4.24}$$

where $D^{R,A}$ are the retarded and advanced Green functions of the scalar field and Π^{-+} the appropriate self-energy. Here we use the notation of [19] for the contour labels. We now perform a semi-classical expansion, retaining only the lowest order derivatives of $\mathbf{P}$

$$\begin{aligned}
\langle \varphi(\mathbf{k})\varphi(-\mathbf{k}) \rangle &= -D^R(\mathbf{k})\Pi^{-+}(\mathbf{x}, \mathbf{k})D^A(\mathbf{k}) \\
&+ \frac{i}{2} \left[\frac{\partial D^R(\mathbf{k})}{\partial k_i} \frac{\partial \Pi^{-+}(\mathbf{x}, \mathbf{k})}{\partial x_i} D^A(\mathbf{k}) - D^R(\mathbf{k}) \frac{\partial \Pi^{-+}(\mathbf{x}, \mathbf{k})}{\partial x_i} \frac{\partial D^A(\mathbf{k})}{\partial k_i} \right] + \dots
\end{aligned} \tag{4.25}$$

where further terms in the semi-classical expansion are higher derivative of $\mathbf{P}$ and can be neglected. At our level of approximation we include the thermal screening term and the lowest order k^2 term with the fixed point interaction

$$D^{R,A}(k) = \frac{1}{\nu r_d T c^{-2} + k^2/(4\pi c \alpha^*)} \tag{4.26}$$

where ν is a numerical constant. Since the electron contribution to the viscosity goes as $\sim 1/\varepsilon^2$ we need the dominant power of $\langle \varphi(k)\varphi(-k) \rangle$ in ε to be no higher than $\sim 1/\varepsilon$ in order for (4.23) to be important. The second term in (4.25) does not contribute – to see this consider that the spatial derivative on Π^{-+}, which acts only on $\mathbf{P}(\mathbf{x})$ in the equilibrium distribution function of the fermions. To order $\partial P_j/\partial x_i$, $\partial \Pi^{-+}/\partial x_i$ does not contribute any powers of ε, while the k derivatives of $D^{R,A}$ only contribute positive powers of ε.

In our approximation of considering only the diagonal distribution functions discussed in the main text, the semi-classical self-energy in the first term of (4.25) is

$$\Pi^{-+}(\mathbf{x}, \mathbf{k}) = -\sum_a \int \frac{\mathrm{d}^4 q}{(2\pi)^4} f_a(\mathbf{q})[1 - f_a(\mathbf{k} + \mathbf{q})]\delta(\varepsilon_{\mathbf{k}+\mathbf{q}} - \varepsilon_{\mathbf{q}}) \tag{4.27}$$

where f_a are the non-equilibrium distribution functions (4.10). To order $\partial P_j / \partial x_i$, the f contribute a single $\sim 1/\varepsilon^2$, which are, however, compensated. For a generic momentum $k \sim \sqrt{T}$ in (4.23), we may neglect the screening in $D^{R,A}$ and each propagator contributes a power ε. For a soft momentum on the order of the screening scale or above $k \sim \sqrt{\varepsilon T}$, the contribution to (4.23) is suppressed by powers of k from $\sim k^2 d^4 k$ in the integral. To lowest order in ε, we can therefore neglect (4.23) in our calculation of η.

Part II

Numerical Simulation of Strongly-Correlated Electrons in a High-Temperature Superconductor

Overview

In the second part of the thesis, we will consider questions related to high-temperature superconductivity observed in monolayer iron selenide FeSe. We will be approaching this question from a mostly numerical perspective, performing unbiased Quantum Monte Carlo simulations on Hubbard-type models, designed to capture the essential physics of highly doped FeSe. In chapter 5, we will give a brief overview of the unconventional superconductivity in the iron based superconductors in general. We discuss general questions related to the numerical methods in chapter 6 and present the details and results of the numerical simulation in chapter 7.

Chapter 5

Unconventional Superconductivity in Iron Based Materials

5.1 High-Temperature Superconductivity

The Bardeen-Cooper-Schrieffer (BCS) theory [86] forms the basis of our understanding of conventional superconductors. In BCS theory, electrons bind together to form bosonic Cooper pairs which condense to form the superconducting state. In general, the order parameter has s-wave symmetry and gapped excitations. The pairing is due to an effective attractive interaction mediated by the exchange of virtual phonons. The typical energy scales are small compared to the Fermi energy, and we can describe superconductivity in the BCS picture as an instability of a Fermi liquid at low temperatures.

Since the 1970s, a number of different classes of materials have been synthesized which fall outside of the BCS paradigm. The most famous of these is the family of the copper based superconductors (cuprates), first discovered in 1986 [87]. While superconductivity still arises from the formation of Cooper pairs, the nature of superconductivity is quite different: it does not arise of a Fermi-liquid normal state, the transition temperature is large, the order parameter is typically d-wave, and superconductivity is only one phase in a complex phase diagram with many proximate phases. The cuprates are materials were very strong electron correlations dominate. In particular, the superconducting paring is not mediated by electron-phonon interactions but through complicated mechanisms originating from the repulsive electron-electron interaction [88–90].

Despite three decades of experiment and theoretical progress and a detailed phenomenological understanding of many materials, fundamental questions and disagreements about theoretical interpretations persist. This is especially true about the nature of the normal state above the superconductor – both the pseudo-gap and the
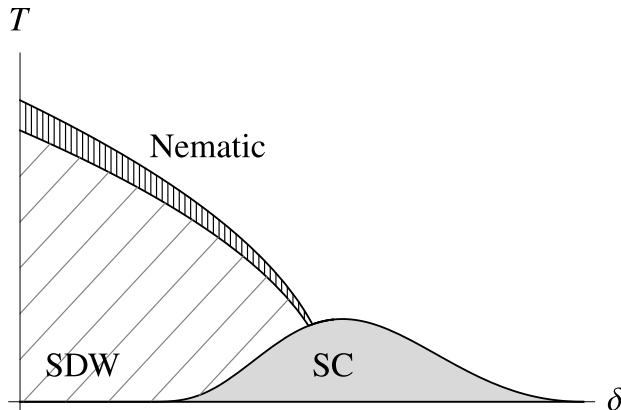
Figure 5.1: Schematic of a phase diagram of a typical iron-pnictide superconductor such as $Ba(Fe_{1-\delta}Co_\delta)_2As_2$ as a function of temperature T and electron doping δ, showing the three different regimes – pure nematic (vertical hatching), stripe spin-density waves (diagonal hatching) and superconductivity (solid gray). Adapted from [95].

strange metal regime. As discussed in the introduction and illustrated by Part I of this thesis, there are many challenges in describing gapless non-Fermi-liquid states. This is exacerbated in many models of the cuprates, where techniques like a usual $1/N$ expansion fail to provide analytic control of the strong interactions of interest [91].

In 2008, the discovery of unconventional superconductors in iron based materials [92, 93] was a dramatic development. It provided a fundamentally new class of high-temperature superconductors, which can be compared to the cuprates and where questions about the nature of the superconductivity and non-Fermi liquid states can be explored. Additionally, the iron-based superconductors are generally believed to have slightly weaker electron-electron interactions and a simpler phase structure then the cuprates [94]. This raises the hope that they are better suited to resolve questions of principle. Nonetheless, the iron-based superconductors have also shown many interesting and novel features.

5.2 Phase Structure of Iron-Based Superconductors

We briefly outline common experimental behavior found in most iron based super-conductors; for a more comprehensive review see [96–99] and references therein. The common feature that unites iron based superconductor are layers of iron atoms arranged on a square lattice with pnictogen or chalcogen atoms staggered above and below the plaquettes of the iron lattice. The simplest structure is that of the so-called 11 compounds, for example iron selenide FeSe (Figure 5.2a). More complicated iron-based superconductors have additional structure in blocking layers between the iron planes. The physics is dominated by the electrons in the iron planes; the iron d_{xz}, d_{yz}, d_{xy} orbitals contribute dominantly to electronic states close to the Fermi surface and gives rise to both electron and hole pockets.

In most iron based superconductors, there are three phases which emerge with changing pressure and doping – a magnetic spin-density wave state (SDW), a nematic state and the superconducting state; a schematic phase diagram is shown in Figure 5.1. The spin-density order is typically either $(0, \pi)$ or $(\pi, 0)$ along the iron atoms and therefore also breaks the C_4 rotational symmetry of the lattice in addition to spin rotation and time-reversal. Slightly preceding or sometimes merged with the SDW is a pure nematic transition that only breaks the C_4 symmetry, but not time-reversal. Due to the coupling between electrons and the lattice, the nematic symmetry breaking is the same as a tetragonal to orthorhombic distortion of the lattice [100, 101]. Although there has been much debate about the exact origins of the nematic phases and the interplay between spin, orbital and lattice degrees of freedom, there is much evidence that this transition is primarily determined by the behavior of electronic degrees of freedom [102–104]. The superconducting order in most iron based superconductors is widely believed to be s^{+-}; such a state is possible because of the more complicated, multi-band nature of the pnictides. Nonetheless, proposals for other pairing symmetries such as s^{++} or d-wave have not been excluded [105].

5.3 Phenomenology of FeSe

A notable exception in the general pattern outlined in the previous section is iron selenide FeSe. In undoped bulk FeSe at ambient pressure, there is a high-temperature nematic transition at $T_N \sim 90$ K and a superconducting transition at $T_c \sim 8$ K [106]. Unlike most iron based superconductors, there is no magnetic ordering at ambient pressures. Nonetheless, magnetic fluctuations have been observed [110, 111], although these are only weakly temperature dependent above the nematic transition [112]. An important development was the growth of FeSe monolayers on strontium titanate SrTiO$_3$ (STO), where superconductivity was reported with $T_c \sim 65$ K from
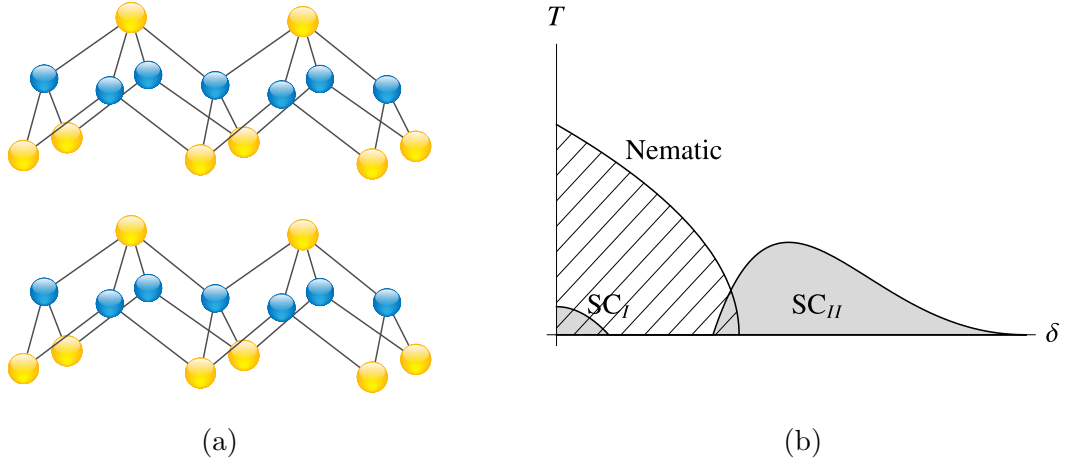
(a)   (b)

Figure 5.2: (a) Schematic showing two layers of the crystal structure of the iron chalcogenide FeSe. The iron atoms (dark blue) form a square lattice in the central plane of each layer. The chalcogen atoms (light yellow) are staggered above and below the plaquettes of the iron lattice. Adapted from [106, 107].
(b) Proposed phase diagram for FeSe as a function of electron doping δ, for example by dosing the surface with potassium K. The bulk superconductivity initially decreases with doping (SC_I). At larger doping, superconductivity reappears and is enhanced to $T_c \sim 40$ K (SC_{II}). Nematic symmetry breaking (from band splitting) decreases with doping; nematic fluctuations are observed in a wide range of the phase diagram. Adapted from [108, 109].

measurements of the Meissner effect [113]. An even higher T_c was reported in an unconventional transport measurement [114] and in an STM study [115]. This has led to an intense effort to study FeSe under different conditions of geometry, doping, pressure and substrate type.

Although no complete picture has emerged, it has become clear that the bulk superconductivity of FeSe can be enhanced to temperatures of $T_c \sim 40$ K in a variety of ways; for example by high electron doping [109, 116, 117] or through the application of pressure [111]. In both these cases, the nematic order is suppressed and disappears as superconductivity reaches a maximum. Nonetheless, the interplay between the two orders remains an open question. In FeSe$_{1-x}$S$_x$, the nematic order is also suppressed with increased chemical pressure from the sulfur, but with little effect on T_c [118]. A schematic phase diagram is shown in Figure 5.2b; for the case of potassium dosing two distinct superconducting domes are reported, while for pressure enhancement only a single dome is seen.

For thin layers of FeSe grown on a verity of substrates, such as MgO [119], sim-

ilar enhancements of T_c up to ~ 40 K are observed. From the growth process, it is expected that these monolayers are doped as compared to the bulk. A similar T_c is achieved in the layered bulk material $(Li_{0.8}Fe_{0.2})OHFeSe$ where electrons are transfered to the FeSe layer [117]; although this compound also has a $T_m \sim 8.5$ K transition to a canted antiferromagnet. This supports the picture that some enhancement of superconductivity is an intrinsic effect.

Because of the high doping effect, the central hole pocket present in the bandstructure of the undoped system is pushed below the Fermi surface [120]. This precludes the s^{+-} pairing symmetry favored to explain the other iron pnictides. Plain s-wave was reported in a scanning tunneling microscopy (STM) study [121]; an angle-resolved photoemission spectroscopy (ARPES) study concluded the gap dependence to be inconsistent with both extended s-wave and d-wave [122].

The additional enhancement to T_c seen in FeSe grown on STO are believed to arise from electron-phonon interactions between the two substrates [123]. Strong evidence for this idea comes from shadow bands seen in ARPES experiments [124], which are due to optical phonons of the surface STO oxygens. Additionally, the strong superconducting enhancement is not seen in two or higher unit cell layers of FeSe on STO [115].

5.4   Electron Nematic Criticality

Electronic nematic criticality has formed the basis of a set of theoretical proposals that have garnered much attention as a possible route for explaining features of high-temperature superconductors. Although probably not applicable in its simplest form, the basic picture is that the superconducting dome seen is covering a nematic quantum critical point, the strange metal phase can be identified in part as the incoherent quantum critical regime and the pseudo-gap phase seen in the cuprates is a signature of the nematic state [125].

In a metal, the nematic transition breaks the rotational symmetry of the Fermi surface down to a lower symmetry, without breaking translational symmetry. In the simple case of an Ising-nematic the C_4 symmetry of electrons on a square lattice is broken down to C_2. When this happens, the entire Fermi surface distorts to align along one of the two broken symmetry axes. The system remains a Fermi liquid on both sides of the transition. Since only a point group symmetry is broken and not a translational symmetry, the order parameter couples to electrons at the same momentum

$$\varphi_N \sim \sum_k f(k) c_k^\dagger c_k \qquad (5.1)$$

where $f(k) = \cos k_x - \cos k_y$ is the $d_{x^2-y^2}$ form factor. Critical fluctuations of the nematic order parameter couple strongly to the entire Fermi surface and give rise to a non-Fermi-liquid state.

Constructing an analytical description of the critical point has proved challenging, as no entirely controlled way has been found to access the critical point. The traditional Hertz-Millis approach [126, 127] proceeds by integrating out the fermions to obtain an effective action of the order parameter and then truncates the effective action at quadratic order. Since fermions are gapless degrees of freedom, the effective bosonic theory has a complicated non-analytic structure and the truncation is unjustified. The most promising analytical methods [128] rely on double ε and $1/N$ expansions in a Fermi-surface patch construction.

Additionally, the non-Fermi-liquid state may itself be unstable towards the formation of a superconductor at low temperatures. The critical fluctuations act to enhance the Cooper pairing in all angular momentum channels [129, 39] and we expect the critical point to be covered by a superconducting dome. This presents a complicated situation as the pairing destroys the very fluctuations and excitations that give rise to it. Recently it was shown in a double expansion calculation [39], that the critical region of the Ising-nematic case is never realized, but preempted by the formation of a superconductor. This casts doubt on the interpretation of the strange metal as arising from the critical fan.

Chapter 6

Determinant Quantum Monte Carlo

The analytical challenges in addressing both fundamental questions about the metallic quantum criticality as well as their application to actual materials, has led to an effort to simulate models numerically. In particular, there has been a renewed interest in recent years [130–134] of using unbiased Determinant Quantum Monte Carlo (DQMC) to study quantum criticality in metals. In this chapter, we review the DQMC algorithm as well as several technical improvements that allow us to simulate the low temperature, strong coupling regime of interacting fermions. We will apply DQMC to study superconductivity in monolayer FeSe in Chapter 7.

6.1 Basic Algorithm

We briefly review the basic DQMC algorithm with discretized time-steps as described in [135–137]. The idea is to directly sample the full partition function in imaginary time. Consider for concreteness a fermion problem discretized on a lattice with on-site four-fermion interactions

$$Z = \text{Tr}\, e^{-\beta H} = \int \mathscr{D}[c^*, c] e^{-S}, \tag{6.1}$$

where

$$S = \int \mathrm{d}\tau \, \left\{ \sum_{\mathbf{i},\mathbf{j}} c^*_{\mathbf{j},\tau} \left[\delta_{\mathbf{ij}} \partial_\tau - t_{\mathbf{ij}} + \delta_{\mathbf{ij}}\mu \right] c_{\mathbf{i},\tau} + \alpha \sum_{\mathbf{i}} O_{\mathbf{i},\tau} O_{\mathbf{i},\tau} \right\}. \tag{6.2}$$

Here $t_{\mathbf{ij}}$ are hopping coefficients and $O_{\mathbf{i},\tau}$ is an on-site bilinear of fermions. The fermion path integral is formally written in terms of Grassmann variables. We introduce an

auxiliary bosonic Hubbard-Stratonovich field φ at each space-time site i, and reduce all interaction terms to be quadratic in fermions. One possible decoupling is

$$e^{\alpha O_i^2} \sim \int \mathrm{d}\varphi_i \; e^{-\varphi_i^2 - 2\sqrt{\alpha}\varphi_i O_i} \tag{6.3}$$

We eliminate all Grassmann variables by integrating out the fermions to obtain

$$Z = \int \mathscr{D}\varphi \; \mathrm{Det}\, G^{-1}(\varphi) e^{-S_b(\varphi)}. \tag{6.4}$$

Here $S_b(\varphi)$ is the bosonic action of the Hubbard-Stratonovich fields and $G^{-1}(\varphi)$ the inverse of the single particle fermion Green function for a given configuration of φ. This integral can be sampled using usual Monte Carlo methods [138–140]. Updates of the Hubbard-Stratonovich field are proposed $\varphi \to \varphi'$ and accepted with probability

$$\min\left[1, \frac{\mathrm{Det}\, G^{-1}(\varphi') e^{-S_b(\varphi')}}{\mathrm{Det}\, G^{-1}(\varphi) e^{-S_b(\varphi)}}\right] \tag{6.5}$$

Despite the simplicity of the above procedure, there are challenges in practically implementing it for the case of strongly correlated systems. These difficulties will manifest themselves as restrictions on the range of parameters (temperature, interaction strength, lattice size), where accurate simulations may be performed.

A central problem in simulating fermion systems using Monte Carlo methods is the so-called sign problem, which arises due to the anti-commuting nature of the fermions. In the context of DQMC, the individual terms of the partition function (6.4) need not be positive. In general the signs of observables generated by the sampling are highly oscillatory. Large numbers are subtracted from each other in order to obtain an estimate for the average result. This leads to an unbounded growth of the statistical errors and renders sampling unreliable. Although models with sign problems can still be simulated, one is mostly limited to the case of very high temperature.

There has been much effort in understanding the detailed sign structure of the partition function Z and finding ways to avoid the sign problem; see [141–146]. Typically, this requires a symmetry, for example time-reversal, which guarantees that each term in the partition function is positive. This has led to the notion of so called 'designer' models – models chosen to be sign problem free while still capturing the essential physics of the problem [147]. We will follow this philosophy in Chapter 7.

6.2   Numerical Instability of the Green Function

The central object in the numerical calculation is $G(\varphi)$, which determines both the update probability (6.5) and is also the basis for calculating other physical observables via Wick's theorem. However, accurately and efficiently calculating the Green

function on a finite precision machine is challenging. The discretized form of the equal time correlation function is

$$G_\varphi(\tau) = [1 + B_\varphi(\tau, 0)B_\varphi(\beta, \tau)]^{-1}. \tag{6.6}$$

Here

$$B_\varphi(\tau, 0) = B(\tau, \tau - \Delta\tau) \ldots B(2\Delta\tau, \Delta\tau)B(\Delta\tau, 0) \tag{6.7}$$

is the propagator discretized in time; for a single time-slice

$$B_\varphi(\Delta\tau + \tau, \tau) = e^{-\Delta\tau H_{int}[\varphi(\tau)]}e^{-\Delta\tau H_0}. \tag{6.8}$$

The multiplication of the string of B matrices introduces large numerical errors on a computer, due to the mixing of finite precision numbers of vastly different scales – the real space basis of the lattice does not take into account any hierarchy of the energies of the problem. One solution [136, 148] is to multiply the matrices consecutively and separate out the scale of the numbers using a rank-revealing factorization such as QR decomposition (with pivoting) or singular value decomposition (SVD). However, naive applications of such methods may fail. For example, the usual SVD algorithm via reduction to a bi-diagonal matrix becomes unstable for large condition numbers and another algorithm such as a Jacobi SVD algorithm must be used [149–151].

When calculating the full determinant, all singular values will enter and so high accuracy is needed. To ensure that rounding errors will not enter the final determinant expression one needs to be careful when performing the inversion (6.6). One method is to perform additional singular value decompositions before inverting [149, 148]

$$G^{-1} = I + B_s(\beta, 0) = I + UDV^T \tag{6.9}$$

We then split D into singular values larger and smaller than 1 ('big' and 'small')

$$D = D_b D_s \tag{6.10}$$

and write

$$G^{-1} = I + UDV = UD_b(D_b^{-1}U^{-1} + D_sV^T) \tag{6.11}$$

the term $(D_b^{-1}U^{-1} + D_sV^T)$ now only contains small numbers. Multiplying U^{-1} and V^T with the appropriate D cancels out numerical errors that were introduced in the original singular value decompositionn. We perform an additional decomposition $(D_b^{-1}U^{-1} + D_sV^T) = \widetilde{U}\widetilde{D}\widetilde{V}^T$ to obtain the stable formulae

$$G = \widetilde{V}\widetilde{D}^{-1}\widetilde{U}^T(UD_b)^{-1} \tag{6.12}$$

$$\det G^{-1} = \det[D_b]\det[\widetilde{D}] \tag{6.13}$$

6.3 Parallel Tempering for DQMC

A challenge of performing any Monte Carlo sampling is to propose new configurations that will quickly explore the space of the variables being sampled and give an accurate estimate of the desired distribution. For DQMC, this means generating statistically independent configurations of φ. However, proposing dramatic changes to φ will generally lead to a rejection in the acceptance step (6.5).

The vast majority of DQMC codes still rely dominantly on local updates due to the computation cost of global updates. In a local updating scheme, sites of the lattice are swept through and changes to the field on each space-time site φ_i proposed. This procedure works well at temperatures high or comparable to the band-width of the fermions. At low temperatures or strong interactions and also anytime we enter into a broken symmetry phase we expect to see ergodicity problems, where the simulations fail to sample over the configuration space and gets confined to some local region. Practically, this is associated with some physical observables being stuck at certain values with unreasonably small error bars [152]. This may present a major limitation as auto-correlation times of the simulation may become so large that the system becomes impossible to simulate.

There has been a long history of developing high acceptance global updates [140]. The existence of these typically rely on a special aspect or symmetry of the model under consideration, such as is the case for the Swenson-Wang or Wolff updates for Potts models [140]. In DQMC, the complex form of the fermion determinant with a Hubbard-Stratonovich field (6.4) means that hardly any global updating schemes are known.

One commonly used update in the Hubbard model is to change the sign of Hubbard-Stratonovich fields on all time-slices of a site. If the interaction is purely on-site and in the limit where there is no-hopping the acceptance probability is 1. To see this, consider the Hubbard model with an Ising decoupling $s = \pm 1$

$$e^{\lambda_s s_i (n_{i,\uparrow} - n_{i,\downarrow})} \tag{6.14}$$

where λ_s is some coefficient. When we set $s_{\mathbf{i},\tau} \to -s_{\mathbf{i},\tau}$ this will leave the Green function invariant, but will change the $\uparrow, \downarrow$ occupation for the spatial site $\mathbf{i}$. The hope is that for sufficiently weak hopping, this update would still be accepted with a high probability.

An approach that has been developed for general Monte Carlo simulations is parallel tempering. To our knowledge, the work presented here [2], along with [132], was among the very first to apply it to a DQMC problem.

The idea of parallel tempering [153] is the set up $N_{parallel}$ number of runs with different values of the interaction $g = \{g_{min}, \ldots, g_{max}\}$ and allow Hubbard-Stratonovich configurations to be exchanged between them. At the weakest interactions, we ex-

pect the system to have short auto-correlation times and the Hubbard-Stratonovich configurations equilibrate very quickly. At strong interactions the system has long auto-correlation times and this is where ergodicity problems arise. The parallel tempering effectively allows configurations to be swapped from strong to weak coupling and back – the strong coupling systems continue to get a new input of de-correlated configurations.

One can view the set of all $N_{parallel}$ simulations as one 'super' Monte-Carlo simulation and the exchange of configurations as a generalized type of update. Provided that the spacing between neighboring interactions is not too large, the typical configurations should be similar and the chance the update is accepted is high. While parallel tempering is typically done with different temperature parameters, any energy parameter can be used. For DQMC simulations, higher temperatures typically use fewer time-slices which helps the system equilibrate faster and so tempering in the interaction is more convenient.

The generalization of the ratio of probabilities in (6.5) for a swap between two simulations is

$$\frac{\det G^{-1}(\{\varphi_1\}, g_2) \det G^{-1}(\{\varphi_1\}, g_1)}{\det G^{-1}(\{\varphi_1\}, g_1) \det G^{-1}(\{\varphi_1\}, g_2)} \cdot \frac{e^{-S_b(\varphi_1) - S_b(\varphi_2)}}{e^{-S_b(\varphi_1) - S_b(\varphi_2)}} \tag{6.15}$$

where g_1, g_2 are the interactions of the simulations. The ratio of the bosonic actions is written for completeness, but cancels out.

There is an interesting alternative to the swap proposed by (6.15); we could attempt a swap in such a way that the ratio of the determinants cancel each other out and only the ratio of the bosonic actions remain. This avoids both the numerical problems and computation effort of calculating the Green function determinant. Because the only combination that enters the determinant is $\varphi\sqrt{|g|}$, we could scale the fields by this factor and then swap. Therefore, we propose

$$\varphi_1^{new} = \varphi_2 \sqrt{|g_2/g_1|} \tag{6.16}$$

$$\varphi_2^{new} = \varphi_1 \sqrt{|g_1/g_2|} \tag{6.17}$$

For simplicity consider the simplest bosonic action $S_b(\varphi) = \sum_i \varphi_i^2$, so that the ratio of probabilities becomes

$$\prod_i \exp\left[-\varphi_{i,1}^2 \left(-1 + \frac{|g_1|}{|g_2|}\right)\right] \exp\left[-\varphi_{i,2}^2 \left(-1 + \frac{|g_2|}{|g_1|}\right)\right] \tag{6.18}$$

We note, however, that in test cases on a lattice with 512 space-time sites, this rescaling resulted in very low acceptance rates ($\sim 10^{-4}$ for interactions $g \sim 1.0$). Nonetheless, this method can be appropriate in other circumstances.

Chapter 7

Quantum Monte Carlo Simulation of FeSe Monolayers with Effective Nematic Interactions

In contrast to bulk FeSe, which exhibits nematic order and low temperature superconductivity, atomic layers of FeSe reverse the situation, having high temperature superconductivity appearing alongside a suppression of nematic order. To investigate this phenomenon, we study a minimal electronic model of FeSe, with interactions that enhance nematic fluctuations. This model is sign problem free, and is simulated using determinant quantum Monte Carlo (DQMC). We developed a DQMC algorithm with parallel tempering, which proves to be an efficient source of global updates and allows us to access the region of strong interactions. Over a wide range of intermediate couplings, we observe superconductivity with an extended s-wave order parameter, along with enhanced, but short ranged, $q = (0, 0)$ ferro-orbital (nematic) order. These results are consistent with approximate weak coupling treatments that predict that nematic fluctuations lead to superconducting pairing. Surprisingly, in the parameter range under study, we do not observe nematic long range order. Instead, at stronger coupling an unusual insulating phase with $q = (\pi, \pi)$ *antiferro*-orbital order appears, which is missed by weak coupling approximations.

7.1   Introduction

A remarkable recent development in materials science has been the observation of enhanced superconductivity in single layers of FeSe, grown initially on $SrTiO_3$ (STO) substrates [115, 154]. In contrast to bulk FeSe which undergoes a superconducting transition at a relatively low temperature $T_c \sim 6$ K [106], T_c in monolayers is at least an order of magnitude larger, in excess of 60 K [113] with even higher transition

temperatures reported by an unconventional transport measurement [114]. Initial studies attributed the enhancement of superconductivity to coupling between electrons in the FeSe layer and an STO phonon, which was also implicated in creating shadow electron bands observed in angle resolved photoemission experiments [124, 155]. However, such shadow bands are also observed for electrons on the surface of STO itself, which does not superconduct [156]. Furthermore, recent studies have observed enhancement of $T_c \sim 40$ K in FeSe in the absence of STO substrate – for example by surface electron doping by depositing potassium [108, 157, 158], or in the layered material $(Li_{0.8}Fe_{0.2})OHFeSe$ [117, 159]. Since the phonon spectra of these materials are entirely different from STO, an alternate mechanism must be at play, which is intrinsic to the FeSe layers. The common element between these and the original FeSe on STO studies is that heavy electron doping leads to a pair of electron like Fermi surfaces [157, 158, 120, 160, 109, 116]. Hence we seek a mechanism for superconductivity that is *intrinsic* to the FeSe layers, that is controlled by electron doping. It has been speculated that the even higher T_c of FeSe on STO is due to a pairing boost arising from the STO phonon [161, 116], in addition to the intrinsic mechanism.

What is the origin of this intrinsic T_c enhancement? Nematic fluctuations present an appealing possibility for the following reasons: (i) Bulk FeSe undergoes a nematic transition at 100 K, and is unique in the family of iron pnictides/chalcogenides in not having a proximate magnetic transition. In fact, no magnetic order is observed down to the lowest temperatures [162, 163] (ii) Electron doping has been shown to suppress nematic order [116] in potassium-doped FeSe, following which superconductivity appears. (iii) Theoretically, fluctuations of nematic order in the vicinity of a nematic quantum critical point are expected to enhance superconductivity, and this effect is particularly pronounced in 2D [39, 164, 129]. However, existing analytical theories have focused on universal aspects of the physics and do not capture non-universal aspects that are relevant to experiments. On the other hand, treatments that incorporate details of FeSe band structure and interactions, often use weak coupling or uncontrolled approximations [165, 166, 161, 167], and may not correctly capture the true phase structure of the system.

In this paper we investigate the role of nematic fluctuations in enhancing superconductivity, by studying a sign problem free model of the FeSe monolayer, using determinant quantum Monte Carlo (DQMC). The phase diagram obtained differs substantially from that predicted by the Random Phase Approximation (RPA) [166], particularly in the strong coupling limit. At intermediate couplings, we find a region with substantially enhanced nematic fluctuations and superconductivity. Although there is no long range ordered nematic, a notable feature is that the maximum enhancement of uniform nematic fluctuations coincides with peak in a superconducting dome. Moreover, we find that superconductivity responds to doping in an essentially asymmetric way – electron doping enhances, while hole doping suppresses super-

conductivity. All these findings link the emergence of superconductivity to nematic fluctuations, and are potentially relevant for the physics of FeSe films.

Other models, which were recently studied using DQMC [130, 131], introduce the order parameter – such as antiferro-magnetic or nematic order – as a separate, dynamic bosonic degree of freedom. Moreover, superconductivity was not observed in the effective model considered by [131]. While such an approach is appropriate to studying universal aspects of quantum phase transitions, here we will be interested in more microscopic questions. We emphasize that our model defined below includes only electronic degrees of freedom, with properly chosen interactions that are sign problem free. Similar techniques can be used to study many other multi-orbital models, for which the presence of two spin species removes the sign problem at any doping.

7.2   Model

We consider a two-band tight binding model, where electrons occupy the d_{xz}, d_{yz} orbitals of iron atoms on a square lattice. This simplified model captures basic features of the iron pnictide bandstructure [168] and allows for nematic symmetry breaking. We take the Hamiltonian

$$H = -\sum_{\mathbf{ij},ab,\sigma} (t_{\mathbf{ij}}^{ab} c_{\mathbf{i}a\sigma}^{\dagger} c_{\mathbf{j}b\sigma} + \text{h.c.}) - \mu \sum_{\mathbf{i},a} n_{\mathbf{i},a} - \frac{g}{2} \sum_{\mathbf{i}} (n_{\mathbf{i},xz} - n_{\mathbf{i},yz})^2 \qquad (7.1)$$

where $a, b = xz, yz$ are orbital indices, $\sigma = \uparrow, \downarrow$ is the spin index and $n_{\mathbf{i},a} = \sum_{\sigma} c_{\mathbf{i}a\sigma}^{\dagger} c_{\mathbf{i}a\sigma}$ is the occupation of orbital a on lattice site $\mathbf{i}$.

Allowed hopping coefficients $t_{\mathbf{ij}}^{ab}$ are dictated by the symmetry of the $d_{xz,yz}$ orbitals and we include hopping between nearest-neighbor (t_1, t_2) and next-nearest-neighbor sites (t_3, t_4), as shown in Fig. 7.1(a). The values of $t_{1,...,4}$ coincide with those used in Ref. [166]; we will measure energy in units of t_1. The Fermi surface in the non-interacting limit $(g = 0)$ with chemical potential $\mu = 0.6$ consists of two electron pockets at X, Y and two hole pockets at Γ, M [Fig. 7.1(b)]. Upon increasing μ the hole pocket at M disappears, while the electron pockets grow.

The attractive interaction term $(g > 0)$ in the second line of Eq. (7.1) favors an on-site nematic symmetry by splitting the two orbitals and breaking C_4 rotational symmetry. This is characterized by a non-zero order parameter $\delta n_{\mathbf{i}} = n_{\mathbf{i},xz} - n_{\mathbf{i},yz}$. Since the interaction is strictly on-site, the pattern of any orbital ordering is not specified a priori.

The weak coupling Random Phase Approximation (RPA) considers the leading instability of the system from the free fermion susceptibility and predicts a variety of orders for Eq. (7.1), depending on the value of μ. In the range $0.2 \lesssim \mu \lesssim 2.5$, including the original parameters considered in [166], the RPA predicts onset of uniform nematic
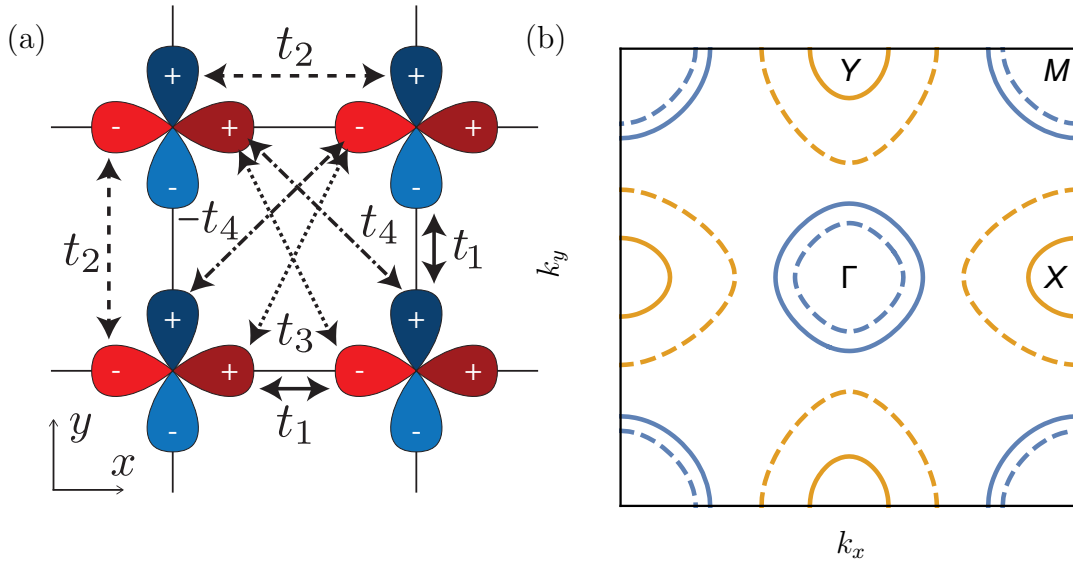
Figure 7.1: (a) Definitions of hopping coefficients $t_{\mathbf{ij}}^{ab}$, where d_{xz} and d_{yz} are schematically shown in red/blue color. All hoppings except for t_4 conserve orbital index. (b) Fermi surface for chemical potential $\mu = 0.6$ (solid lines) and $\mu = 2$ (dashed lines) at $g = 0$, showing two hole pockets at Γ, M and two electron pockets at X, Y. The hopping values are $t_1 = -1.0$, $t_2 = 1.5$, $t_3 = -1.2$, $t_4 = -0.95$. The filling fractions are $f = 0.43, 0.58$ at $\mu = 0.6, 2$ respectively.

order for $g_c \approx 1.7$. For $\mu \gtrsim 2.5$, the susceptibility peaks at wave-vector $(0, \pi)$ and $(\pi, 0)$ predicting stripe order, while for $\mu \lesssim 0.2$ the susceptibility peaks at wave-vector (π, π) predicting antiferro-orbital (AFO) [antiferro-quadrupole (AFQ)] order.

When interactions dominate $g \gg t, \mu$, we can get intuition from a strong coupling expansion in t/g. At zeroth order, the ground state is doubly degenerate – either orbital xz or yz is fully occupied on each site. This degeneracy is split by second order processes, leading to nearest- and next-nearest-neighbor Ising-type interactions of order $\sim t^2/g$. For our hopping parameters, the ground state of the resulting Ising model is a checkerboard pattern [169, 170] – this corresponds to AFO order at half-filling ($f = 0.5$ electrons per site per orbital per spin). On the other hand, intuition from anti-ferromagnetic order in the half-filled Hubbard model [171] suggests that doping will quickly destroy this checkerboard order.

The sensitivity of the weak coupling instability to μ, along with the instability of AFO order with respect to doping away from half filling suggest a number of competing orders and we proceed to study the phase diagram of Eq. (7.1) numerically.

7.3   Sign-problem-free DQMC

We simulate the model in an unbiased fashion using Determinant Quantum Monte Carlo with discretized time-steps as described in [135–137]. In order to sample the full imaginary time partition function $Z = \text{Tr} \, e^{-\beta H}$, we decouple the interactions in the nematic channel using an onsite, continuous Hubbard-Stratonovich field φ; the interaction term is $\sim \sum_{\mathbf{i}} \varphi_{\mathbf{i}} \delta n_{\mathbf{i}}$. Integrating out the fermions analytically, the partition function becomes a path integral of the auxiliary field, $Z = \int D\varphi \, e^{-S_b(\varphi)} \text{Det} \, G^{-1}(\varphi)$, and can be sampled using the Monte Carlo algorithm. The fermion determinant $\text{Det} \, G^{-1}(\varphi)$ decouples into spin sectors since the kinetic energy does not mix spins and $\varphi_{\mathbf{i}}$ couples equally to $\uparrow, \downarrow$ through $\delta n_{\mathbf{i}}$. The spin sectors are equal by time reversal for any field configuration φ, $\text{Det} \, G^{-1}(\varphi) = \text{Det} \, G_{\uparrow}^{-1}(\varphi) \, \text{Det} \, G_{\downarrow}^{-1}(\varphi) = |\text{Det} \, G_{\uparrow}^{-1}(\varphi)|^2 > 0$, which guarantees that the partition function can be sampled in a sign-problem-free manner at any filling.

We perform sweeps through the space-time lattice and update the Hubbard-Stratonovich field φ on each site. As φ couples different orbitals, we perform rank-two Woodbury updates [172] when calculating $G_{\uparrow}$ on a given time-slice. We use the one-sided Jacobi Singular-Value Decomposition algorithm [149] for numerical stabilization [148] on every second time-slice. In order to reduce ergodicity problems at strong interactions, we run the DQMC simulation in parallel for various interaction strengths g and use a parallel-tempering algorithm [153], which proposes to exchange φ configurations between simulations at different g after each sweep. For the data presented here, we have simulated systems with periodic boundary conditions up to $L^2 = 10 \times 10$ in spatial size (200 orbitals) with an inverse temperature of up to $\beta = 8$ ($\beta E_F \sim 40$); the imaginary time step is $\Delta \tau = 1/16$.

7.4   Phase Diagram

We swept the phase diagram of the model described by Eq. (7.1) as a function of interaction strength g and filling fraction f (Fig. 7.2), showing regions of superconducting and antiferro-orbital order. Since we are considering a finite temperature system in two spatial dimensions, only quasi-long-range order exists. Our simulations are on lattice sizes smaller than the scale of these fluctuations and our finite size extrapolations indicate long range order of the $T = 0$ ground state.

We first discuss the phase diagram in vicinity of half-filling $f = 0.5$, which corresponds to two electrons per site. In the limit of strong coupling $g \gtrsim 3.7$ we see development of long-range antiferro-orbital order. This is fully consistent with the intuition from the strong coupling expansion of a fully polarized state in the orbital basis with a checkerboard ordering pattern (Fig. 7.3 inset). The onset of order is confirmed by considering the equal time nematic correlation function
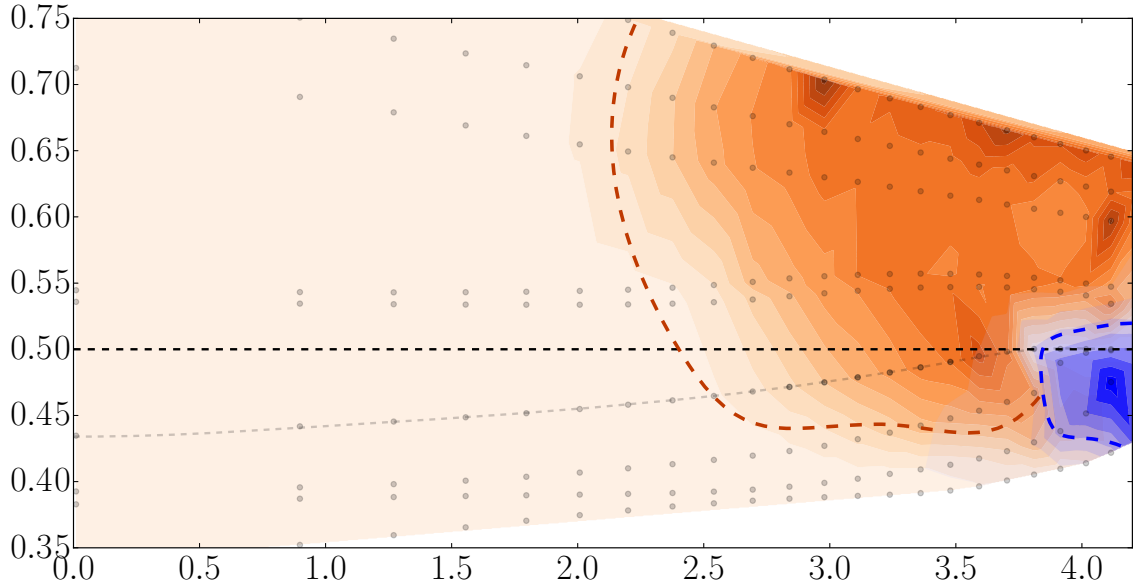
Figure 7.2: Phase diagram of the model Eq. (7.1) as a function of interaction g and filling fraction f at inverse temperature $\beta = 8$. The red dashed line indicates the boundary of the region where the superconducting order parameter extrapolates to a finite value in the thermodynamic limit. The blue dashed line marks the boundary of phase with antiferro-orbital order. The red / blue coloring is the interpolated equal time correlation function of the s-wave superconductivity / antiferro-orbital order on a 10×10 lattice; white space is outside of range sampled. Dots indicate simulated points along 9 values of the chemical potentials $\mu = -1.0, -0.5, 0.0, 0.6, 1.6, 1.8, 3.0, 3.5, 4.0$; the dots joined by a grey dotted line correspond to $\mu = 0.6$. The black dashed line marks half filling.

$$C_{\tau=0}(\mathbf{q}) = \frac{1}{L^2} \sum_{\mathbf{i},\mathbf{j}} e^{i\mathbf{q}\cdot(\mathbf{i}-\mathbf{j})} \langle \delta n_{\mathbf{i}} \delta n_{\mathbf{j}} \rangle. \tag{7.2}$$

The behavior of $C_{\tau=0}(\mathbf{q})$ at $q = (\pi, \pi)$ is shown in Fig. 7.3. To reduce finite size effects, we show $C_{\tau=0}(\mathbf{q})$ averaged over three neighboring points $\mathbf{q}, \mathbf{q} + 2\pi\hat{\mathbf{x}}/L, \mathbf{q} + 2\pi\hat{\mathbf{y}}/L$ which coincide in the thermodynamic limit. We also can confirm the onset of order via the Binder ratio [173] for the boson field φ conjugate to δn at zero frequency.

The AFO order rapidly disappears when the system is doped away from half-filling, or the interaction strength is decreased. In contrast to the expectations from weak coupling RPA, we do not observe any nematic ordering at other wave-vectors. Instead, when the long range AFO disappears, we observe a large region with non-zero superconducting order. To probe the superconducting order, we study the equal-time
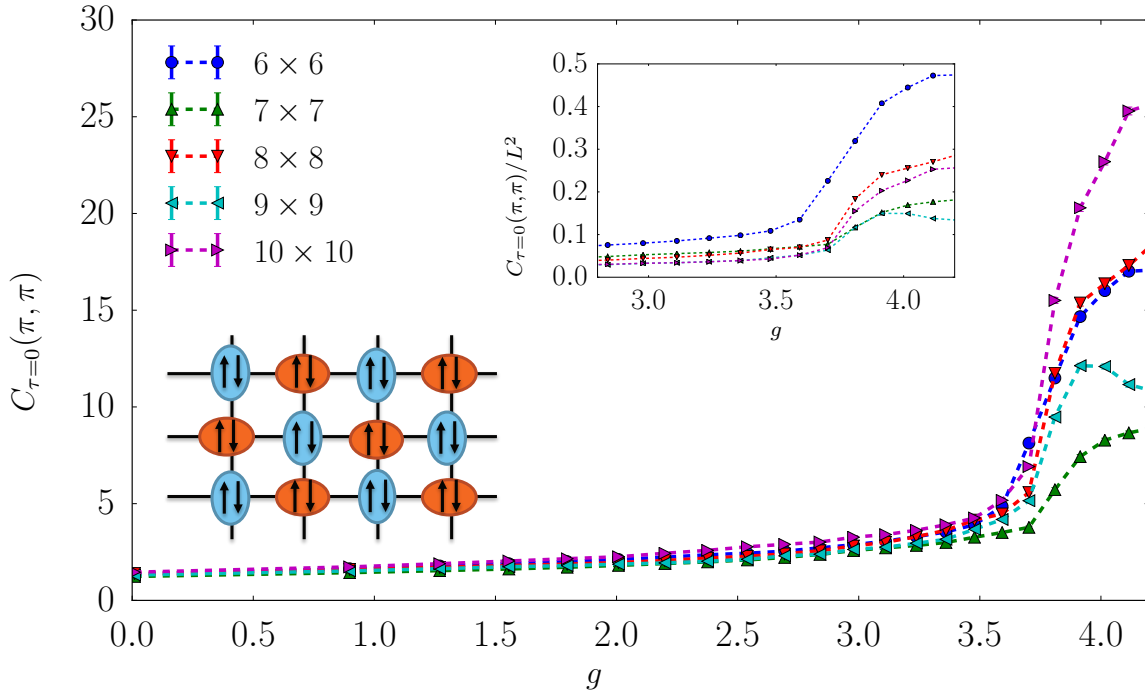
Figure 7.3: Equal time nematic correlation function averaged around $q = (\pi, \pi)$ rises rapidly, signaling onset of the long-range order. The left inset shows a cartoon of the antiferro-orbital ordering pattern. The second inset indicates the convergence of the correlation function, when normalized by L^2, as expected from long-range order. Note the even-odd effect due to periodic boundary conditions.

pair correlation function $\sim \langle \Delta_{ab}(\mathbf{i}) \Delta_{cd}^\dagger(\mathbf{j}) \rangle$, where the specific form of the $\Delta_{ab}(\mathbf{i})$ depends on the symmetry of pairing. We consider all possible irreducible representations of lattice point group D_4 involving on-site, nearest neighbor and next nearest neighbor sites and found non-vanishing pair correlation function for the order parameter with s-wave (A_1) symmetry. The dominant response is the on-site pairing, where the only non-vanishing pairing is within the same orbitals with equal sign ($A_1 \times A_1$ representation),

$$\Delta^{\mathrm{s}}(\mathbf{i}) = \frac{1}{2} c_{\mathbf{i}a\alpha} (i\sigma_{\alpha\beta}^y)(\tau_{ab}^0) c_{\mathbf{i}b\beta}. \tag{7.3}$$

Here σ and τ are the Pauli matrices acting in the spin and orbital basis, and τ^0 is an identity matrix. The order parameter $\Delta^{\mathrm{s}}(\mathbf{i})$ coexists with the extended s-wave pairing between nearest neighbors, $\Delta^{\mathrm{s\text{-}ex}}(\mathbf{i})$, where the gap changes sign between orbitals ($B_1 \times B_1$ representation),
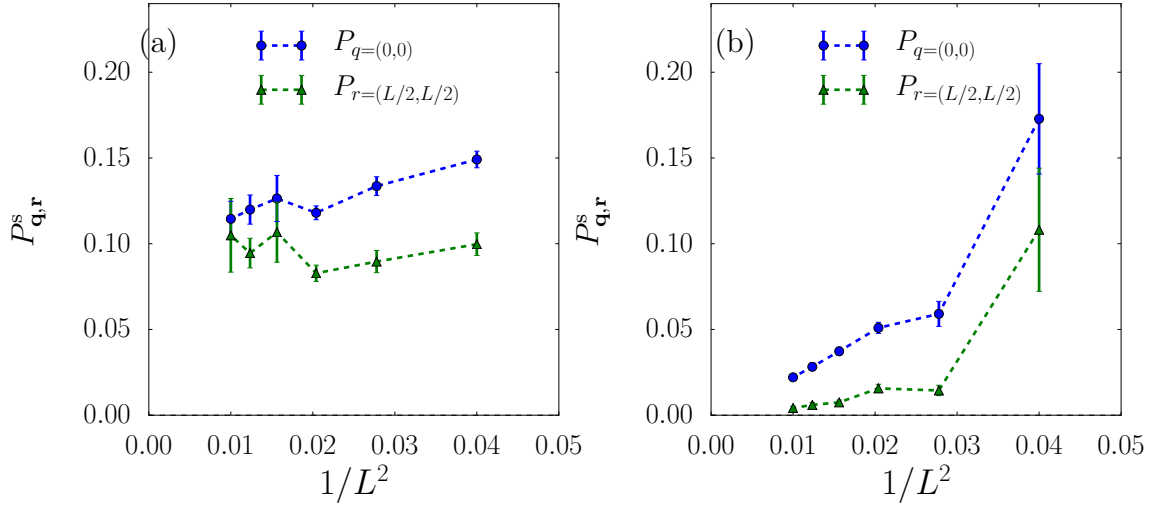
Figure 7.4: Finite size scaling of the on-site s-wave equal time pair correlation at maximal-distance $P^s_{\mathbf{r}=(L/2,L/2)}$ and zero-momentum $P^s_{\mathbf{q}=0}$. (a) In the region which we identify as a superconductor ($\mu = 0.6$, $g = 3.59$) $P_{\mathbf{r}}, P_{\mathbf{q}}$ extrapolate to a finite value in the thermodynamic limit. (b) In the region of the AFO phase ($\mu = 0.6$, $g = 3.91$), both pair correlation functions scale to zero in the thermodynamic limit.

$$\Delta^{\text{s-ex}}(\mathbf{i}) = \frac{1}{2}\sum_{\hat{\mathbf{e}}} d(\hat{\mathbf{e}})\, c_{\mathbf{i}+\hat{e},a\alpha}(\sigma^y_{\alpha\beta})(\tau^z_{ab})c_{\mathbf{i}b\beta}, \tag{7.4}$$

as is reflected by τ^z matrix. Here, the vector $\hat{\mathbf{e}}$ runs over nearest neighbors and $d(\hat{\mathbf{e}})$ denotes the $d_{x^2-y^2}$-wave symmetry form-factor, $d(\pm\hat{\mathbf{x}}) = 1$, and $d(\pm\hat{\mathbf{y}}) = -1$. For $\mu \geq 2$, the s-wave pairing also extends to next-nearest neighbor sites, along the diagonals of the square lattice. It has a d_{xy}-wave form factor along with the τ^x pairing in the orbital basis ($B_2 \times B_2$ representation).

The equal time ($\tau = 0$) pair correlation function for the on-site s-wave is defined as

$$P^s_{\mathbf{r}} = \frac{1}{L^2}\sum_{\mathbf{i}}\langle\Delta^s(\mathbf{i}+\mathbf{r})\Delta^s(\mathbf{i})\rangle, \quad P^s_{\mathbf{q}} = \frac{1}{L^2}\sum_{\mathbf{r}}e^{i\mathbf{q}\cdot\mathbf{r}}P^s_{\mathbf{r}} \tag{7.5}$$

in the coordinate and Fourier space respectively, where both sums are performed over all lattice points. In the thermodynamic limit, the value of $P^s_{\mathbf{q}}$ at $\mathbf{q} = 0$ must converge to the value of $P^s_{\mathbf{r}}$ at maximum separation $\mathbf{r} = (L/2, L/2)$, if there is long-range superconducting order. At small L, $P^s_{\mathbf{q}=0}$ includes mostly short range contributions and overestimates the order parameter [174]. Fig. 7.4(a) shows data from the superconducting phase where both quantities extrapolate to finite value as $1/L \to 0$, moreover these quantities become closer to each other for larger system sizes. In contrast,
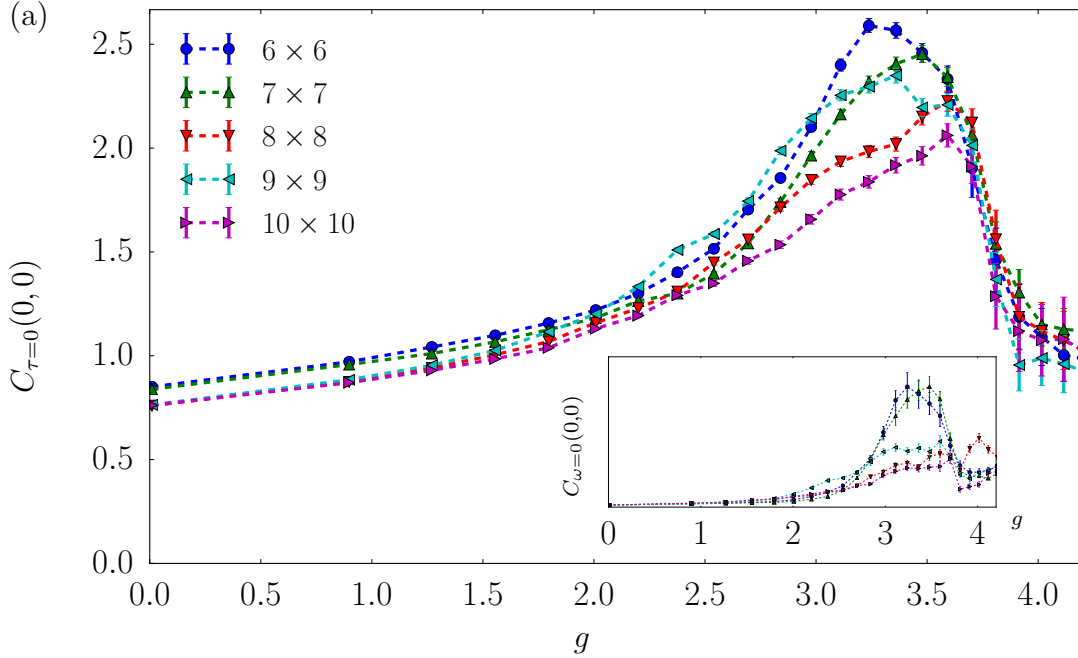
Figure 7.5: The uniform nematic correlation function; the inset shows the unnormalized nematic susceptibility $C_{\omega=0}(0,0) = \langle \delta n \delta n \rangle$ at $q = 0, \omega = 0$ – here we derive this data from the correlation function of the Hubbard-Stratonovich fields, since φ is conjugate to δn.

Fig. 7.4(b) shows data from the AFO phase, where the pair correlation functions are non-zero only due to finite size effects and extrapolate to zero in the thermodynamic limit.

In order to confirm the above picture of the ordered phases, we consider the pseudo-density of states [175]

$$\widetilde{N} = \frac{1}{TL^2} \sum_{\mathbf{q}} G\left(\tau = \frac{\beta}{2}, \mathbf{q}\right) = \sum_{\mathbf{q}} \int_{-\infty}^{\infty} \frac{N(\omega, \mathbf{q})\mathrm{d}\omega}{2T \cosh(\omega/2T)} \tag{7.6}$$

where $G(\tau, \mathbf{q})$ is the imaginary time Green function summed over orbitals and $N(\omega, \mathbf{q})$ is the single-particle density of states at momentum $\mathbf{q}$. $\widetilde{N}$ gives us a measure of the single-particle states at the Fermi energy without numerically challenging analytic continuation; in the limit where the temperature is far below any other energy scale $\widetilde{N} \simeq \pi N(\omega = 0)$. Fig. 7.7 shows $\widetilde{N}$ for the chemical potentials $\mu = 0.6$ (a) and $\mu = 4.0$ (b). At weak interactions, there is a finite density of states corresponding to the metallic phase with larger finite size effects due to the discrete sampling of the Fermi surface. Once the system enters the superconducting phase, $\widetilde{N}$ drops to
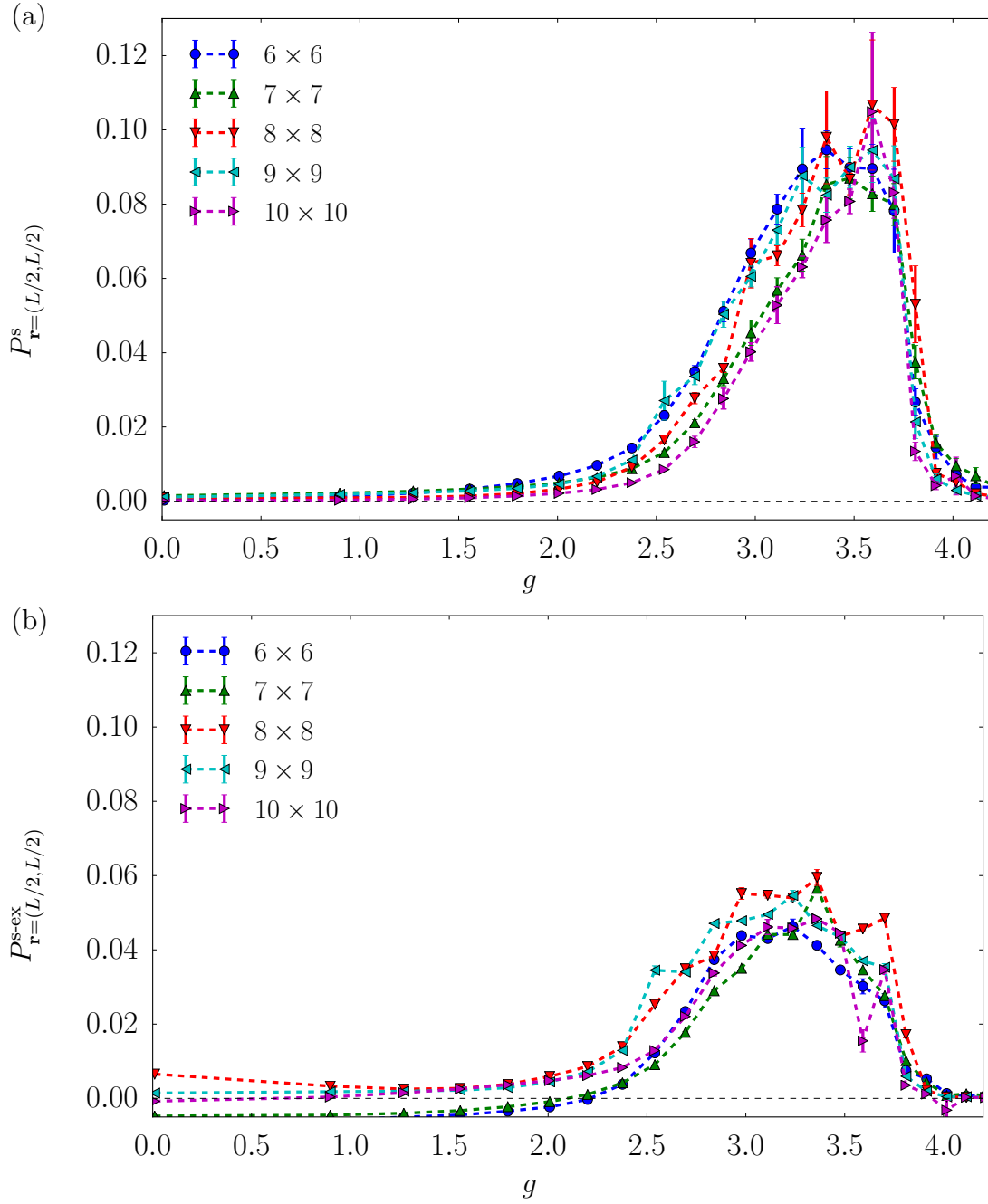
(a)

(b)

Figure 7.6: The (a) on-site s-wave pair correlation function, and (b) nearest neighbor extended s-wave. They have a very similar dependence on the interaction strength for fixed value of $\mu = 0.6$ as the uniform nematic correlation functions (Figure 7.5). The onset and termination of the on-site superconducting order coincides with similar trends in the nematic susceptibility.

zero which is consistent with the fully gapped s-wave pairing symmetry. For (a) the system is in the AFO phase at $g \gtrsim 3.7$, which we see is Mott insulating.

7.5 Origin of Superconductivity

We observed an extended s-wave superconducting order in a large portion of the phase diagram. One may worry that this superconducting order arises only from the attractive parts of the interaction in the model defined by Eq. (7.1). However, decoupling the interaction in the pairing channel within a mean field calculation only leads to significant superconducting pairing for much stronger interactions, $g \geq 6$ at $\beta = 8$. Since the mean field approximation tends to overestimate the ordering tendency, this suggests that this scenario in isolation is improbable.

A number of recent works [129, 39] addressed enhancement of superconductivity in a vicinity of a uniform nematic transition by nematic fluctuations. While we do not find long-range uniform nematic order in the considered range of doping and interactions, the intuition from weak-coupling RPA suggests possible competition between various ordering tendencies for this model. Then, upon approaching the AFO transition, we expect to have enhancement of fluctuations in various channels, including uniform nematic fluctuations.

To check if the uniform nematic fluctuations play a role in the superconducting phase, we compare the evolution of equal time nematic and pair correlation functions with interactions, Fig. 7.5 and Fig. 7.6. The uniform nematic correlation function has a maximum around $g \approx 3.5$, exactly where $P_\mathbf{r}^\mathrm{s}$ peaks. For larger interaction, the onset of the AFO phase signaled by a rapid increase in AFO correlations for $g \geq 3.7$ (see Fig. 7.3) coincides with the destruction of superconductivity and suppression of uniform nematic correlations.

To further explore the relationship between uniform nematic fluctuations and superconductivity, we consider adding an explicit symmetry breaking term $\Delta\mu \sum_\mathbf{i} \delta n_\mathbf{i}/2$ to the Hamiltonian. This suppresses the uniform nematic fluctuations by causing the system to order in one of the orbitals; the superconducting order (Fig. 7.8) is strongly suppressed with increase symmetry breaking. However, the symmetry breaking term also causes a change in the band-structure and pushes the filling dependence to higher electron doping (at a fixed chemical potential μ), which we also expect to modify the superconducting response. While it is hard to isolate the impact of these different effects, the following comparison may be worthwhile – an orbital splitting of $\Delta\mu = 0.6$ leads to a 65% suppression of superconductivity at $g = 3.0$. However, a uniform chemical potential change of the same magnitude at the same filling leads to a suppression of 67% for hole doping and a 60% enhancement for electron doping. Thus orbital splitting appears to have a more significant impact on superconducting pairing.
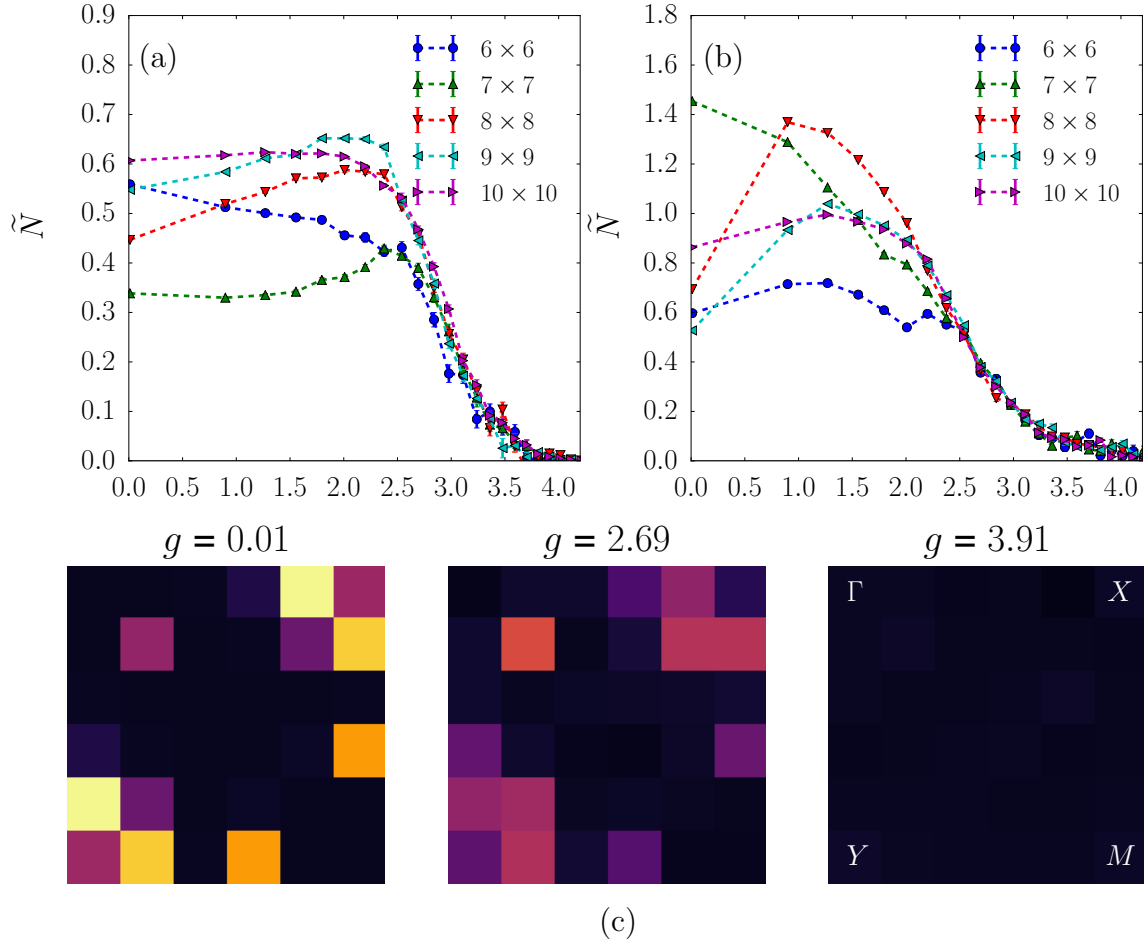
Figure 7.7: The pseudo-density of states $\widetilde{N}$ along lines of constant chemical potential (a) $\mu = 0.6$ and (b) $\mu = 4.0$ shows large finite size variation in the metallic state and starts deceasing once the system enters a gapped state. From correlation function measurements the system in (a) enters the superconducting state at $g \sim 2.5$ and the AFO state at $g \sim 3.7$; we see here that the AFO state is gapped. The system in (b) is strongly electron doped and always far away from the AFO state; the drop to zero of $\widetilde{N}$ suggest the superconductor is fully gapped, as expected from a s-wave superconductor. The three bottom panels (c) show the **q** space resolved pseudo-density of states of the 10×10 lattice at $\mu = 0.6$; one quater of the Brillouin zone is shown. As the interaction increase, the states close to the Fermi surface are gapped out.
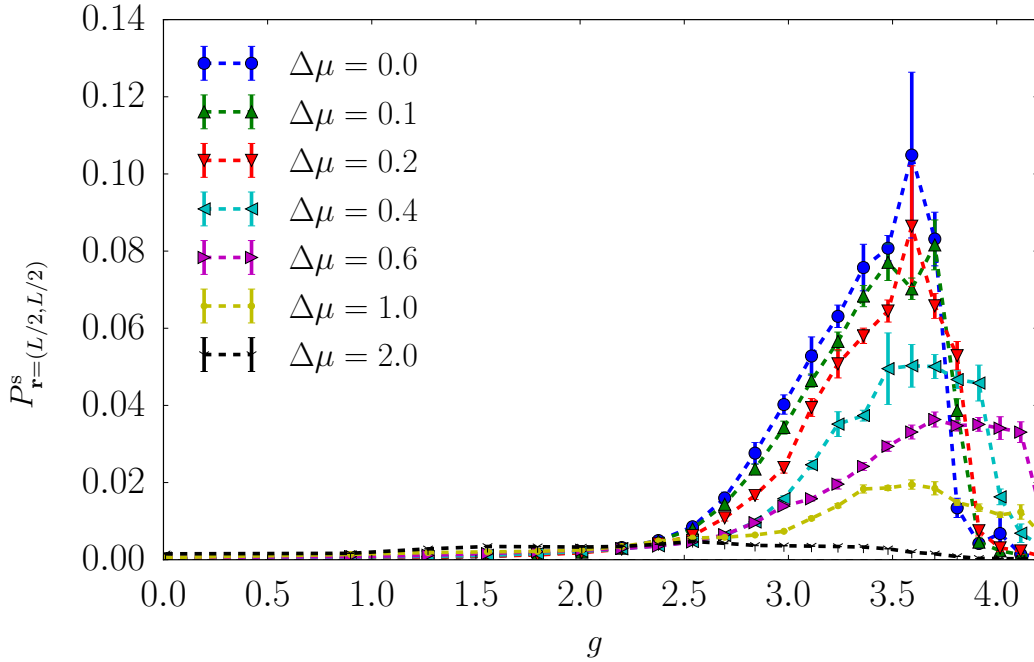
Figure 7.8: On-site s-wave correlation is suppressed in simulations which have an explicit orbital symmetry breaking term $\Delta\mu \sum_{\mathbf{i}} \delta n_{\mathbf{i}}/2$. The simulations are performed at constant chemical potential $\mu = 0.6$, so the dependence of filling on g is different from the case $\Delta\mu = 0$. Note for $\Delta\mu \gtrsim 0.4$, pairing persists to higher values of the interaction strength g. This is understandable since the filling is shifted to higher electron doping where the insulating phase is suppressed.

7.6 Discussion and Implications for FeSe

Motivated by the idea of a nematic instability driven by electron-electron interactions [104], we considered a purely electronic model with interactions in the nematic channel. Our studies revealed a phase diagram with a large superconducting region. While our two-band model is oversimplified, it roughly captures the behavior of the FeSe Fermi surface with doping: electron pockets increase in size upon doping, while hole pockets shrink. Moreover, we use a local on-site interaction that favors imbalance in orbital occupancy. We consider our interaction term as an approximation after one integrates out high energy bosonic modes; similar interaction terms were shown to arise from the Fe-ion oscillations [176]. The on-site Coulomb repulsion, which is absent in our model, will presumably suppress on site pairing, but the extended parts of the superconducting pairing, which we find share the same trends as

the onsite pairing, will presumably be less affected, and may be directly relevant for the observed superconductivity in FeSe films.

Our model in Eq. (7.1) was found to have a long-range antiferro-orbital order at strong coupling, whereas the bulk FeSe is believed to have a uniform nematic order. Nevertheless, the model considered here has enhanced uniform nematic fluctuations as a precursor to the onset of uniform order. We found that these nematic fluctuations are correlated with enhancement of superconductivity. Moreover, we observed an essential asymmetry of the superconducting phase, doping with electrons enhances superconducting order, while hole doping destroys it. This is consistent with the phenomenology of FeSe, where SC emerges upon strong electron doping. One can potentially try to connect the nematic fluctuation mechanism more closely with the observed superconductivity by looking for anisotropy of the gaps in momentum space [129], which is left for future work on larger system sizes. Beyond considerations of FeSe, many systems, such as intermetallic rare earth compounds, show ferro-quadrupole or antiferro-quadrupole order without any magnetic phase transitions [58]. They have recently received renewed attention [177] and our results might be relevant to the physics of these materials.

To conclude, we proposed a two band model with interactions which enhance nematic fluctuations and studied this model using DQMC. We find that robust high temperature superconductivity appears that is accompanied by ferro-nematic fluctuations, although the ferro-nematic ordered phase itself does not appear in the range that was studied. Our findings can be relevant to enhanced superconductivity in FeSe films, as well as other situations where a fluctuating order may be responsible for superconductivity. Our methods are readily extendible to a wide class of multi-orbital models.

Bibliography

1. Dumitrescu, P. T. Shear viscosity in a non-Fermi-liquid phase of a quadratic semimetal. *Phys. Rev. B* **92,** 121102 (2015).

2. Dumitrescu, P. T., Serbyn, M., Scalettar, R. T. & Vishwanath, A. Superconductivity and Nematic Fluctuations in a model of FeSe monolayers: A Determinant Quantum Monte Carlo Study. *ArXiv e-prints.* arXiv: `1512.08523` `[cond-mat.supr-con]` (2015).

3. Landau, L. D. & Lifshitz, E. M. *Statistical physics* 3rd ed. (Pergamon Press, Oxford, 1980).

4. Wilson, K. G. & Kogut, J. The renormalization group and the ϵ expansion. *Phys. Rep.* **12,** 75 –199 (1974).

5. Wilson, K. G. The renormalization group and critical phenomena. *Rev. Mod. Phys.* **55,** 583–600 (1983).

6. Zinn-Justin, J. *Quantum field theory and critical phenomena* 4th ed (Clarendon Press, Oxford, 2002).

7. Forster, D. *Hydrodynamic fluctuations, broken symmetry, and correlation functions* (Addison-Wesley, Redwood City, Calif., 1990).

8. Chaikin, P. M. & Lubensky, T. C. *Principles of condensed matter physics* (Cambridge University Press, Cambridge, 1995).

9. Weinberg, S. *The quantum theory of fields* (Cambridge University Press, Cambridge, 2000).

10. Sachdev, S. *Quantum phase transitions* 2nd ed. (Cambridge University Press, Cambridge, 2011).

11. Hasan, M. Z. & Kane, C. L. *Colloquium*: Topological insulators. *Rev. Mod. Phys.* **82,** 3045–3067 (2010).

12. Qi, X.-L. & Zhang, S.-C. Topological insulators and superconductors. *Rev. Mod. Phys.* **83,** 1057–1110 (2011).

13. Senthil, T. Symmetry-Protected Topological Phases of Quantum Matter. *Annu. Rev. Condens. Matter Phys.* **6,** 299–324 (2015).

14. Wen, X.-G. *Quantum field theory of many-body systems: from the origin of sound to an origin of light and electrons* (Oxford University Press, Oxford, 2004).

15. Senthil, T., Balents, L., Sachdev, S., Vishwanath, A. & Fisher, M. P. A. Quantum criticality beyond the Landau-Ginzburg-Wilson paradigm. *Phys. Rev. B* **70,** 144407 (2004).

16. Senthil, T., Vishwanath, A., Balents, L., Sachdev, S. & Fisher, M. P. A. Deconfined Quantum Critical Points. *Science* **303,** 1490–1494 (2004).

17. Abrikosov, A. A., Gorkov, L. P. & Dzyaloshinski, I. E. *Methods of quantum field theory in statistical physics* (Dover Publications, New York, 1975).

18. Abrikosov, A. A. *Fundamentals of the theory of metals* (North-Holland, Amsterdam, 1988).

19. Lifshitz, E. M. & Pitaevskii, L. P. *Physical kinetics* (Pergamon Press, Oxford, 1981).

20. Nozières, P & Pines, D. *The theory of quantum liquids* (Perseus Books, Cambridge, Mass., 1999).

21. Polchinski, J. Effective Field Theory and the Fermi Surface. *ArXiv High Energy Physics - Theory e-prints.* eprint: `hep-th/9210046` (1992).

22. Shankar, R. Renormalization-group approach to interacting fermions. *Rev. Mod. Phys.* **66,** 129–192 (1994).

23. Lee, P. A., Nagaosa, N. & Wen, X.-G. Doping a Mott insulator: Physics of high-temperature superconductivity. *Rev. Mod. Phys.* **78,** 17–85 (2006).

24. Emery, V. J. & Kivelson, S. A. Superconductivity in Bad Metals. *Phys. Rev. Lett.* **74,** 3253–3256 (1995).

25. Novoselov, K. S. *et al.* Electric Field Effect in Atomically Thin Carbon Films. *Science* **306,** 666–669 (2004).

26. Castro Neto, A. H., Guinea, F., Peres, N. M. R., Novoselov, K. S. & Geim, A. K. The electronic properties of graphene. *Rev. Mod. Phys.* **81,** 109–162 (2009).

27. Novoselov, K. S. Nobel Lecture: Graphene: Materials in the Flatland. *Rev. Mod. Phys.* **83,** 837–849 (2011).

28. Liu, Z. K. *et al.* A stable three-dimensional topological Dirac semimetal Cd_3As_2. *Nat. Mater.* **13,** 677–681 (2014).

29. Neupane, M. *et al.* Observation of a three-dimensional topological Dirac semimetal phase in high-mobility Cd_3As_2. *Nat. Commun.* **5** (2014).

30. Lu, L. *et al.* Experimental observation of Weyl points. *Science* **349,** 622–624 (2015).

31. Lv, B. Q. *et al.* Experimental Discovery of Weyl Semimetal TaAs. *Phys. Rev. X* **5,** 031013 (2015).

32. Xu, S.-Y. *et al.* Discovery of a Weyl fermion semimetal and topological Fermi arcs. *Science* **349,** 613–617 (2015).

33. Elias, D. C. *et al.* Dirac cones reshaped by interaction effects in suspended graphene. *Nat. Phys.* **7,** 701–704 (2011).

34. Di Francesco, P., Mathieu, P. & Sénéchal, D. *Conformal field theory* (Springer, New York, 1997).

35. Deshpande, V. V., Bockrath, M., Glazman, L. I. & Yacoby, A. Electron liquids and solids in one dimension. *Nature* **464,** 209–216 (2010).

36. Rantner, W. & Wen, X.-G. Electron Spectral Function and Algebraic Spin Liquid for the Normal State of Underdoped High T_c Superconductors. *Phys. Rev. Lett.* **86,** 3871–3874 (2001).

37. Balents, L. Spin liquids in frustrated magnets. *Nature* **464,** 199–208 (2010).

38. Hornreich, R. M., Luban, M. & Shtrikman, S. Critical Behavior at the Onset of $\vec{\mathrm{k}}$-Space Instability on the λ Line. *Phys. Rev. Lett.* **35,** 1678–1681 (1975).

39. Metlitski, M. A., Mross, D. F., Sachdev, S. & Senthil, T. Cooper pairing in non-Fermi liquids. *Phys. Rev. B* **91,** 115111 (2015).

40. Sachdev, S. What Can Gauge-Gravity Duality Teach Us About Condensed Matter Physics? *Annu. Rev. Condens. Matter Phys.* **3,** 9–33 (2012).

41. Hartnoll, S. A. Lectures on holographic methods for condensed matter physics. *Classical and Quantum Gravity* **26,** 224002 (2009).

42. Kovtun, P. K., Son, D. T. & Starinets, A. O. Viscosity in Strongly Interacting Quantum Field Theories from Black Hole Physics. *Phys. Rev. Lett.* **94,** 111601 (2005).

43. Son, D. T. & Starinets, A. O. Viscosity, Black Holes, and Quantum Field Theory. *Ann. Rev. Nucl. Part. Sci.* **57,** 95–118 (2007).

44. Gunnarsson, O., Calandra, M. & Han, J. E. *Colloquium*: Saturation of electrical resistivity. *Rev. Mod. Phys.* **75,** 1085–1099 (2003).

45. Brigante, M., Liu, H., Myers, R. C., Shenker, S. & Yaida, S. Viscosity Bound and Causality Violation. *Phys. Rev. Lett.* **100,** 191601 (2008).

46. Kats, Y. & Petrov, P. Effect of curvature squared corrections in AdS on the viscosity of the dual gauge theory. *J. High Energy Phys.* **2009,** 044 (2009).

47. Schäfer, T. & Teaney, D. Nearly perfect fluidity: from cold atomic gases to hot quark gluon plasmas. *Rep. Prog. Phys.* **72,** 126001 (2009).

48. Schäfer, T. Ratio of shear viscosity to entropy density for trapped fermions in the unitarity limit. *Phys. Rev. A* **76,** 063618 (2007).

49. Bruun, G. M. & Smith, H. Shear viscosity and damping for a Fermi gas in the unitarity limit. *Phys. Rev. A* **75,** 043612 (2007).

50. Enss, T., Haussmann, R. & Zwerger, W. Viscosity and scale invariance in the unitary Fermi gas. *Ann. Phys. (NY)* **326,** 770 –796 (2011).

51. Müller, M., Schmalian, J. & Fritz, L. Graphene: A Nearly Perfect Fluid. *Phys. Rev. Lett.* **103,** 025301 (2009).

52. Abrikosov, A. A. Calculation of critical indices for zero-gap semiconductors. *Sov. Phys. JETP* **39,** 709 (1974).

53. Abrikosov, A. A. & Beneslavskii, S. D. Some Properties of Gapless Semiconductors of the Second Kind. *J. Low Temp. Phys.* **5,** 141 (1971).

54. Abrikosov, A. A. & Beneslavskii, S. D. Possible Existence of Substances Intermediate Between Metals and Dielectrics. *Sov. Phys. JETP* **32,** 699 (1971).

55. Moon, E.-G., Xu, C., Kim, Y. B. & Balents, L. Non-Fermi-Liquid and Topological States with Strong Spin-Orbit Coupling. *Phys. Rev. Lett.* **111,** 206401 (2013).

56. Khan, F. S. & Allen, P. B. Sound attenuation by electrons in metals. *Phys. Rev. B* **35,** 1002–1019 (1987).

57. Pippard, A. Theory of Ultrasonic Attenuation in Metals and Magneto-Acoustic Oscillations. *Proc. R. Soc. Lond. A Math. Phys. Sci.* **257,** 165–193 (1960).

58. Lüthi, B. *Physical acoustics in the solid state* (Springer, Berlin, 2007).

59. Vafek, O. & Vishwanath, A. Dirac Fermions in Solids: From High-T_c Cuprates and Graphene to Topological Insulators and Weyl Semimetals. *Annu. Rev. Condens. Matter Phys.* **5,** 83–112 (2014).

60. Witczak-Krempa, W., Chen, G., Kim, Y. B. & Balents, L. Correlated Quantum Phenomena in the Strong Spin-Orbit Regime. *Annu. Rev. Condens. Matter Phys.* **5,** 57–82 (2014).

61. Herbut, I. F. & Janssen, L. Topological Mott Insulator in Three-Dimensional Systems with Quadratic Band Touching. *Phys. Rev. Lett.* **113,** 106401 (2014).

62. Luttinger, J. M. Quantum Theory of Cyclotron Resonance in Semiconductors: General Theory. *Phys. Rev.* **102,** 1030–1041 (1956).

63. Bernevig, B. A., Hughes, T. L. & Zhang, S.-C. Quantum Spin Hall Effect and Topological Phase Transition in HgTe Quantum Wells. *Science* **314,** 1757–1761 (2006).

64. König, M. *et al.* Quantum Spin Hall Insulator State in HgTe Quantum Wells. *Science* **318,** 766–770 (2007).

65. Murakami, S., Nagaosa, N. & Zhang, S.-C. SU(2) Non-Abelian holonomy and dissipationless spin current in semiconductors. *Phys. Rev. B* **69,** 235206 (2004).

66. Fu, L. Topological Crystalline Insulators. *Phys. Rev. Lett.* **106,** 106802 (2011).

67. Biedenharn, L. C & Louck, J. D. *Angular momentum in quantum physics: theory and application* (Addison-Wesley, Reading, Mass., 1981).

68. Abrikosov, A. A. On the energy spectrum of gapless semiconductors with considerably differing masses of electrons and holes. *J. Low Temp. Phys.* **18,** 185–199 (1975).

69. Kubo, R. Statistical-Mechanical Theory of Irreversible Processes. I. General Theory and Simple Applications to Magnetic and Conduction Problems. *J Physical Soc Japan* **12,** 570–586 (1957).

70. Bradlyn, B., Goldstein, M. & Read, N. Kubo formulas for viscosity: Hall viscosity, Ward identities, and the relation with conductivity. *Phys. Rev. B* **86,** 245309 (2012).

71. Jeon, S. Hydrodynamic transport coefficients in relativistic scalar field theory. *Phys. Rev. D* **52,** 3591–3642 (1995).

72. Jeon, S. & Yaffe, L. G. From quantum field theory to hydrodynamics: Transport coefficients and effective kinetic theory. *Phys. Rev. D* **53,** 5799–5809 (1996).

73. Ziman, J. M. *Electrons and Phonons* (Oxford University Press, Oxford, 1960).

74. Arnold, P., Moore, G. D. & Yaffe, L. G. Transport coefficients in high temperature gauge theories (I): leading-log results. *J. High Energy Phys.* **2000,** 001 (2000).

75. Abrikosov, A. A. & Khalatnikov, I. M. The theory of a fermi liquid (the properties of liquid ^{3}He at low temperatures). *Rep. Prog. Phys.* **22,** 329 (1959).

76. Son, D. T. Quantum critical point in graphene approached in the limit of infinitely strong Coulomb interaction. *Phys. Rev. B* **75,** 235423 (2007).

77. Sheehy, D. E. & Schmalian, J. Quantum Critical Scaling in Graphene. *Phys. Rev. Lett.* **99,** 226803 (2007).

78. Gazit, S., Podolsky, D., Auerbach, A. & Arovas, D. P. Dynamics and conductivity near quantum criticality. *Phys. Rev. B* **88,** 235108 (2013).

79. Witczak-Krempa, W., Sorensen, E. S. & Sachdev, S. The dynamics of quantum criticality revealed by quantum Monte Carlo and holography. *Nat. Phys.* **10,** 361–366 (2014).

80. Janssen, L. & Herbut, I. F. Nematic quantum criticality in three-dimensional Fermi system with quadratic band touching. *Phys. Rev. B* **92,** 045117 (2015).

81. Hicks, C. W. *et al.* Quantum Oscillations and High Carrier Mobility in the Delafossite $PdCoO_2$. *Phys. Rev. Lett.* **109,** 116401 (2012).

82. Hahn, T. Cuba – a library for multidimensional numerical integration. *Computer Physics Communications* **168,** 78 –95 (2005).

83. Altland, A. & Simons, B. D. *Condensed Matter Field Theory* 2nd ed. (Cambridge University Press, Cambridge, 2010).

84. Rammer, J. & Smith, H. Quantum field-theoretical methods in transport theory of metals. *Rev. Mod. Phys.* **58,** 323–359 (1986).

85. Kamenev, A. *Field theory of non-equilibrium systems* ISBN: 9780521760829 (Cambridge University Press, Cambridge, 2011).

86. Bardeen, J., Cooper, L. N. & Schrieffer, J. R. Theory of Superconductivity. *Phys. Rev.* **108,** 1175–1204 (1957).

87. Bednorz, J. G. & Müller, K. A. Possible High T_c Superconductivity in the Ba-La-Cu-O System. *Z. Phys. B: Condens. Matter* **64,** 189–193 (1986).

88. Leggett, A. J. *Quantum liquids: Bose condensation and Cooper pairing in condensed-matter systems* (Oxford University Press, Oxford, 2006).

89. Norman, M. R. The Challenge of Unconventional Superconductivity. *Science* **332,** 196–200 (2011).

90. Keimer, B., Kivelson, S. A., Norman, M. R., Uchida, S. & Zaanen, J. From quantum matter to high-temperature superconductivity in copper oxides. *Nature* **518,** 179–186 (2015).

91. Lee, S.-S. Low-energy effective theory of Fermi surface coupled with U(1) gauge field in $2 + 1$ dimensions. *Phys. Rev. B* **80,** 165102 (2009).

92. Kamihara, Y., Watanabe, T., Hirano, M. & Hosono, H. Iron-Based Layered Superconductor $La[O_{1-x}F_x]$ FeAs (x= 0.05-0.12) with T_c=26 K. *J. Am. Chem. Soc.* **130,** 3296–3297 (2008).

93. Takahashi, H. *et al.* Superconductivity at 43 K in an iron-based layered compound $LaO_{1-x}F_x FeAs$. *Nature* **453,** 376–378 (2008).

94. Basov, D. N. & Chubukov, A. V. Manifesto for a higher Tc. *Nat. Phys.* **7,** 272–276 (2011).

95. Chu, J.-H., Analytis, J. G., Kucharczyk, C. & Fisher, I. R. Determination of the phase diagram of the electron-doped superconductor $Ba(Fe_{1-x}Co_x)_2 As_2$. *Phys. Rev. B* **79,** 014506 (2009).

96. Paglione, J. & Greene, R. L. High-temperature superconductivity in iron-based materials. *Nat. Phys.* **6,** 645–658 (2010).

97. Johnston, D. C. The puzzle of high temperature superconductivity in layered iron pnictides and chalcogenides. *Adv. Phys.* **59,** 803–1061 (2010).

98. Stewart, G. R. Superconductivity in iron compounds. *Rev. Mod. Phys.* **83,** 1589–1652 (2011).

99. Martinelli, A., Bernardini, F. & Massidda, S. The phase diagrams of iron-based superconductors: Theory and experiments. *C. R. Phys.* **17,** 5 –35 (2016).

100. de la Cruz, C. *et al.* Magnetic order close to superconductivity in the iron-based layered $LaO_{1-x}F_xFeAs$ systems. *Nature* **453,** 899–902 (2008).

101. Pratt, D. K. *et al.* Coexistence of Competing Antiferromagnetic and Superconducting Phases in the Underdoped $Ba(Fe_{0.953}Co_{0.047})_2As_2$ Compound Using X-ray and Neutron Scattering Techniques. *Phys. Rev. Lett.* **103,** 087001 (2009).

102. Fang, C., Yao, H., Tsai, W.-F., Hu, J. & Kivelson, S. A. Theory of electron nematic order in LaFeAsO. *Phys. Rev. B* **77,** 224509 (2008).

103. Xu, C., Müller, M. & Sachdev, S. Ising and spin orders in the iron-based superconductors. *Phys. Rev. B* **78,** 020501 (2008).

104. Fernandes, R. M., Chubukov, A. V. & Schmalian, J. What drives nematic order in iron-based superconductors? *Nat. Phys.* **10,** 97–104 (2014).

105. Hirschfeld, P. J. Using gap symmetry and structure to reveal the pairing mechanism in Fe-based superconductors. *C. R. Phys.* **17,** 197–231 (2016).

106. Hsu, F.-C. *et al.* Superconductivity in the PbO-type structure α-FeSe. *Proc. Natl. Acad. Sci. U.S.A.* **105,** 14262–14264 (2008).

107. Chubukov, A. & Hirschfeld, P. J. Iron-based superconductors, seven years later. *Physics Today* **68,** 46–52 (2015).

108. Wen, C. H. P. *et al.* Anomalous correlation effects and unique phase diagram of electron doped FeSe revealed by angle resolved photoemission spectroscopy. *Nat. Commun.* **7** (2016).

109. Song, C.-L. *et al.* Observation of Double-Dome Superconductivity in Potassium -Doped FeSe Thin Films. *Phys. Rev. Lett.* **116,** 157001 (2016).

110. Bendele, M. *et al.* Coexistence of superconductivity and magnetism in $FeSe_{1-x}$ under pressure. *Phys. Rev. B* **85,** 064517 (2012).

111. Medvedev, S. *et al.* Electronic and magnetic phase diagram of β-$Fe_{1.01}$Se with superconductivity at 36.7K under pressure. *Nat. Mater.* **8,** 630–633 (2009).

112. Shamoto, S. *et al.* Spin nematic susceptibility studied by inelastic neutron scattering in FeSe. *ArXiv e-prints.* arXiv: `1511.04267 [cond-mat.supr-con]` (2015).

113. Zhang, Z. *et al.* Onset of the Meissner effect at 65 K in FeSe thin film grown on Nb-doped $SrTiO_3$ substrate. English. *Sci. Bull. (Beijing)* **60,** 1301–1304 (2015).

114. Ge, J.-F. *et al.* Superconductivity above 100 K in single-layer FeSe films on doped $SrTiO_3$. *Nat. Mater.* **14,** 285–289 (2015).

115. Qing-Yan, W. *et al.* Interface-Induced High-Temperature Superconductivity in Single Unit-Cell FeSe Films on $SrTiO_3$. *Chinese Physics Letters* **29,** 037402 (2012).

116. Ye, Z. R. *et al.* Simultaneous emergence of superconductivity, inter-pocket scattering and nematic fluctuation in potassium-coated FeSe superconductor. *ArXiv e-prints.* arXiv: `1512.02526 [cond-mat.supr-con]` (2015).

117. Lu, X. F. *et al.* Coexistence of superconductivity and antiferromagnetism in $(Li_{0.8}Fe_{0.2})OHFeSe$. *Nat. Mater.* **14,** 325–329 (2015).

118. Hosoi, S. *et al.* Nematic quantum critical point without magnetism in $FeSe_{1-x}S_x$ superconductors. *ArXiv e-prints.* arXiv: `1604.00184 [cond-mat.supr-con]` (2016).

119. Shiogai, J., Ito, Y., Mitsuhashi, T., Nojima, T. & Tsukazaki, A. Electric-field-induced superconductivity in electrochemically etched ultrathin FeSe films on $SrTiO_3$ and MgO. *Nat. Phys.* **12,** 42–46 (2015).

120. He, S. *et al.* Phase diagram and electronic indication of high-temperature superconductivity at 65 K in single-layer FeSe films. *Nat. Mater.* **12,** 605–610 (2013).

121. Fan, Q. *et al.* Plain s-wave superconductivity in single-layer FeSe on $SrTiO_3$ probed by scanning tunnelling microscopy. *Nat. Phys.* **11,** 946–952 (2015).

122. Zhang, Y. *et al.* Superconducting gap anisotropy in monolayer FeSe thin film. *ArXiv e-prints.* arXiv: `1512.06322 [cond-mat.supr-con]` (2015).

123. Lee, D.-H. What makes the T_c of $FeSe/SrTiO_3$ so high? *Chinese Physics B* **24,** 117405 (2015).

124. Lee, J. J. *et al.* Interfacial mode coupling as the origin of the enhancement of T_c in FeSe films on $SrTiO_3$. *Nature* **515,** 245–248 (2014).

125. Fradkin, E., Kivelson, S. A., Lawler, M. J., Eisenstein, J. P. & Mackenzie, A. P. Nematic Fermi Fluids in Condensed Matter Physics. *Annu. Rev. Condens. Matter Phys.* **1,** 153–178 (2010).

126. Hertz, J. A. Quantum critical phenomena. *Phys. Rev. B* **14,** 1165–1184 (1976).

127. Millis, A. J. Effect of a nonzero temperature on quantum critical points in itinerant fermion systems. *Phys. Rev. B* **48,** 7183–7196 (1993).

128. Mross, D. F., McGreevy, J., Liu, H. & Senthil, T. Controlled expansion for certain non-Fermi-liquid metals. *Phys. Rev. B* **82,** 045121 (2010).

129. Lederer, S., Schattner, Y., Berg, E. & Kivelson, S. A. Enhancement of Superconductivity near a Nematic Quantum Critical Point. *Phys. Rev. Lett.* **114,** 097001 (2015).

130. Berg, E., Metlitski, M. A. & Sachdev, S. Sign-Problem–Free Quantum Monte Carlo of the Onset of Antiferromagnetism in Metals. *Science* **338,** 1606–1609 (2012).

131. Schattner, Y., Lederer, S., Kivelson, S. A. & Berg, E. Ising nematic quantum critical point in a metal: a Monte Carlo study. *ArXiv e-prints.* arXiv: `1511.03282 [cond-mat.supr-con]` (2015).

132. Schattner, Y., Gerlach, M. H., Trebst, S. & Berg, E. Competing Orders in a Nearly Antiferromagnetic Metal. *ArXiv e-prints.* arXiv: `1512.07257 [cond-mat.supr-con]` (2015).

133. Li, Z.-X., Wang, F., Yao, H. & Lee, D.-H. The nature of effective interaction in cuprate superconductors: a sign-problem-free quantum Monte-Carlo study. *ArXiv e-prints.* arXiv: `1512.04541 [cond-mat.supr-con]` (2015).

134. Li, Z.-X., Wang, F., Yao, H. & Lee, D.-H. Quantum Monte Carlo study of the T_c enhancement mechanism in FeSe on $SrTiO_3$. *ArXiv e-prints.* arXiv: `1512.06179 [cond-mat.supr-con]` (2015).

135. Blankenbecler, R., Scalapino, D. J. & Sugar, R. L. Monte Carlo calculations of coupled boson-fermion systems. I. *Phys. Rev. D* **24,** 2278–2286 (1981).

136. White, S. R. *et al.* Numerical study of the two-dimensional Hubbard model. *Phys. Rev. B* **40,** 506–516 (1989).

137. Assaad, F. & Evertz, H. in *Computational Many-Particle Physics* (eds Fehske, H., Schneider, R. & Weiße, A.) 277–356 (Springer, Berlin Heidelberg, 2008).

138. Metropolis, N., Rosenbluth, A. W., Rosenbluth, M. N., Teller, A. H. & Teller, E. Equation of State Calculations by Fast Computing Machines. *The Journal of Chemical Physics* **21,** 1087–1092 (1953).

139. Krauth, W. *Statistical mechanics: algorithms and computations* (Oxford University Press, Oxford, 2006).

140. Thijssen, J. *Computational physics* (Cambridge University Press, Cambridge, 2007).

141. Loh, E. Y. *et al.* Sign problem in the numerical simulation of many-electron systems. *Phys. Rev. B* **41,** 9301–9307 (1990).

142. Troyer, M. & Wiese, U.-J. Computational Complexity and Fundamental Limitations to Fermionic Quantum Monte Carlo Simulations. *Phys. Rev. Lett.* **94,** 170201 (2005).

143. Wu, C. & Zhang, S.-C. Sufficient condition for absence of the sign problem in the fermionic quantum Monte Carlo algorithm. *Phys. Rev. B* **71,** 155115 (2005).

144. Li, Z.-X., Jiang, Y.-F. & Yao, H. Solving the fermion sign problem in quantum Monte Carlo simulations by Majorana representation. *Phys. Rev. B* **91,** 241117 (2015).

145. Wei, Z. C., Wu, C., Li, Y., Zhang, S. & Xiang, T. Majorana Positivity and the Fermion sign problem of Quantum Monte Carlo Simulations. *ArXiv e-prints.* arXiv: `1601.01994 [cond-mat.str-el]` (2016).

146. Li, Z.-X., Jiang, Y.-F. & Yao, H. Majorana-time-reversal symmetries: a fundamental principle for sign-problem-free quantum Monte Carlo simulations. *ArXiv e-prints.* arXiv: `1601.05780 [cond-mat.str-el]` (2016).

147. Kaul, R. K., Melko, R. G. & Sandvik, A. W. Bridging Lattice-Scale Physics and Continuum Field Theory with Quantum Monte Carlo Simulations. *Annu. Rev. Condens. Matter Phys.* **4,** 179–215 (2013).

148. Loh, E. Y. *et al. Stable simulations of many fermion systems* tech. rep. (Los Alamos National Lab, United States, 1989), LA–UR–89–3143.

149. Bai, Z., Lee, C., Li, R.-C. & Xu, S. Stable solutions of linear systems involving long chain of matrix multiplications. *Linear Algebra and its Applications* **435,** 659 –673 (2011).

150. Drmac, Z. & Veselic, K. New fast and accurate Jacobi SVD algorithm. I. *SIAM J. Matrix Anal. Appl.* **29,** 1322–1342 (2008).

151. Drmac, Z. & Veselic, K. New fast and accurate Jacobi SVD algorithm. II. *SIAM J. Matrix Anal. Appl.* **29,** 1343–1362 (2008).

152. Scalettar, R. T., Noack, R. M. & Singh, R. R. P. Ergodicity at large couplings with the determinant Monte Carlo algorithm. *Phys. Rev. B* **44,** 10502–10507 (1991).

153. Katzgraber, H. G., Trebst, S., Huse, D. A. & Troyer, M. Feedback-optimized parallel tempering Monte Carlo. *J. Stat. Mech.* **2006,** P03018 (2006).

154. Liu, D. *et al.* Electronic origin of high-temperature superconductivity in single-layer FeSe superconductor. *Nat. Commun.* **3,** 931 (2012).

155. Peng, R. *et al.* Tuning the band structure and superconductivity in single-layer FeSe by interface engineering. *Nat. Commun.* **5** (2014).

156. Chen, C., Avila, J., Frantzeskakis, E., Levy, A. & Asensio, M. C. Observation of a two-dimensional liquid of Fröhlich polarons at the bare $SrTiO_3$ surface. *Nat. Commun.* **6** (2015).

157. Miyata, Y., Nakayama, K., Sugawara, K., Sato, T. & Takahashi, T. High-temperature superconductivity in potassium-coated multilayer FeSe thin films. *Nat. Mater.* **14,** 775–779 (2015).

158. Tang, C. *et al.* Interface-enhanced electron-phonon coupling and high- temperature superconductivity in potassium-coated ultrathin FeSe films on $SrTiO_3$. *Phys. Rev. B* **93,** 020507 (2016).

159. Sun, H. *et al.* Soft Chemical Control of Superconductivity in Lithium Iron Selenide Hydroxides $Li_{1−x}Fe_x(OH)Fe_{1−y}Se$. *Inorg. Chem.* **54,** 1958–1964 (2015).

160. Tan, S. *et al.* Interface-induced superconductivity and strain-dependent spin density waves in $FeSe/SrTiO_3$ thin films. *Nat. Mater.* **12,** 634–640 (2013).

161. Xiang, Y.-Y., Wang, F., Wang, D., Wang, Q.-H. & Lee, D.-H. High-temperature superconductivity at the $FeSe/SrTiO_3$ interface. *Phys. Rev. B* **86,** 134508 (2012).

162. Baek, S.-H. *et al.* Orbital-driven nematicity in FeSe. *Nat. Mater.* **14,** 210–214 (2015).

163. Baek, S.-H. *et al.* Nematicity and in-plane anisotropy of superconductivity in FeSe detected by [77]Se nuclear magnetic resonance. *ArXiv e-prints.* arXiv: `1510.07533 [cond-mat.supr-con]` (2015).

164. Maier, T. A. & Scalapino, D. J. Pairing interaction near a nematic QCP of a 3-band CuO_2 model. *ArXiv e-prints.* arXiv: `1405.5238 [cond-mat.supr-con]` (2014).

165. Graser, S, Maier, T. A., Hirschfeld, P. J. & Scalapino, D. J. Near-degeneracy of several pairing channels in multiorbital models for the Fe pnictides. *New J. Phys.* **11,** 025016 (2009).

166. Yamase, H. & Zeyher, R. Superconductivity from orbital nematic fluctuations. *Phys. Rev. B* **88,** 180502 (2013).

167. Jiang, K., Hu, J., Ding, H. & Wang, Z. Interatomic Coulomb interaction and electron nematic bond order in FeSe. *Phys. Rev. B* **93,** 115138 (2016).

168. Raghu, S., Qi, X.-L., Liu, C.-X., Scalapino, D. J. & Zhang, S.-C. Minimal two-band model of the superconducting iron oxypnictides. *Phys. Rev. B* **77,** 220503 (2008).

169. Binder, K. & Landau, D. P. Phase diagrams and critical behavior in Ising square lattices with nearest- and next-nearest-neighbor interactions. *Phys. Rev. B* **21,** 1941–1962 (1980).

170. Yin, J. & Landau, D. P. Phase diagram and critical behavior of the square-lattice Ising model with competing nearest-neighbor and next-nearest-neighbor interactions. *Phys. Rev. E* **80,** 051117 (2009).

171. Hirsch, J. E. Two-dimensional Hubbard model: Numerical simulation study. *Phys. Rev. B* **31,** 4403–4419 (1985).

172. Press, W. H., Teukolsky, S. A., Vetterling, W. & Flannery, B. *Numerical recipes: The art of scientific computing* 3rd ed. (Cambridge University Press, Cambridge, 2007).

173. Binder, K. Finite size scaling analysis of ising model block distribution functions. English. *Z. Phys. B: Condens. Matter* **43,** 119–140 (1981).

174. Varney, C. N. *et al.* Quantum Monte Carlo study of the two-dimensional fermion Hubbard model. *Phys. Rev. B* **80,** 075116 (2009).

175. Trivedi, N. & Randeria, M. Deviations from Fermi-Liquid Behavior above T_c in 2D Short Coherence Length Superconductors. *Phys. Rev. Lett.* **75,** 312–315 (1995).

176. Kontani, H. & Onari, S. Orbital-Fluctuation-Mediated Superconductivity in Iron Pnictides: Analysis of the Five-Orbital Hubbard-Holstein Model. *Phys. Rev. Lett.* **104,** 157001 (2010).

177. Rosenberg, E., Chu, J.-H., Fisher, I. & Ruff, J. Evidence for ferroquadrupole order in YbRu2Ge2 from x-ray diffraction and elastoresistivity measurements. *Bulletin of the American Physical Society* (2016).